Nano-scale approaches for the development and optimization of state-of-the-art semiconductor photovoltaic devices

A Thesis submitted to the University of Manchester for the degree of
Doctor of Philosophy
In the Faculty of Engineering and Physical Science

2014

EDSON GARDUÑO-NOLASCO

School of Electrical and Electronic Engineering

LIST OF CONTENTS

Words count including footnotes and endnotes: 43,090

LIST OF FIGURES

LIST OF TABLES

ABSTRACT

Thesis Title: Nano-scale approaches for the development and optimization of state-of-the-art semiconductor photovoltaic devices

Name: Edson Garduño-Nolasco

Degree: Doctor of Philosophy

University: The University of Manchester

Date: April, 2013

This project is concerned with both the study of different Multiple Quantum Wells (MQWs) structures using the $In_{0.53}Ga_{0.47}As/In_{0.52}Al_{0.48}As$ material system lattice matched to InP and a systematic investigation of the properties of InAs QD systems within GaAs with the aim of achieving enhancements of solar cell performance. The key challenge is the growth of QDs solar cell structures which exhibit sufficient absorption (enhanced infrared absorption) to increase short circuit current density (Jsc) but which can still maintains a high open circuit voltage (Voc). The research consists of epitaxial growth using state-of–the-art MBE, optical absorption, photoluminescence and high resolution x-ray diffraction measurements as well as device fabrication and characterization of novel solar cell structures. Optimization was performed on these novel cells to further improve their efficiency by inserting stacks of QD into different regions of the device. The effect of localized doping of such structures was used in an attempt to maintain and enhance the open-circuit voltage which in turn increases the device efficiency. The fabricated devices were characterized using measurements of the dark/light current-voltage (I-V) characteristics and spectral response (50-480 K). Solar cell external quantum efficiencies under standard air mass (AM) 1.5 spectrum were determined and the suitability of these new cells under solar concentration were assessed. Full physical simulations are performed using SILVACO semiconductors modelling software to generate models of multi-junction solar cells that were crucial in informing iterations to growth and fabrication and help to reconcile theory with experiment.

One of the key findings, of this thesis, is the fact that Intermediate band photovoltaic devices using material based on InAs/GaAs vertically stacked quantum dot arrays, can be used in applications according to specific configuration criteria such as high temperature operation conditions. The intermediate band cell, including an inter-dot doped configuration, has been found to be a potential candidate as the inter dot doping profile

reduces the efficiency degradation below the GaAs values including an enhancement in the open circuit voltage. It has been proved that these devices not only have a good performance at high temperatures but also by changing the vertical stacking QD layer periodicity can enhance the short circuit current density while keeping a large open circuit voltage. It was confirmed in practical device operation that thermal energy is required to enable the intermediate band in InAs/GaAs QD materials. The impact of this works can help in the future improvements of the intermediate band solar cells based on InAs on GaAs QD. The best overall efficiency of 11.6 % obtained in this work is an excellent value for so simple devices configuration. The Si_3N_4, tested for the first time on InAs/GaAs QD materials, reduces the reflectance on the device surface to a value of 2% and the operational wavelength can be tuned by controlling the layer thickness. A 100 nm Si_3N_4 antireflective coating proved to be an excellent coating from 700 to 1000 nm. In terms of short circuit current density a 37% enhancement was achieved.

DECLARATION

No portion of the work referred to in the thesis has been submitted in support of an application for another degree or qualification of this or any other university or other institute of learning.

COPYRIGHT

i. The author of this thesis (including any appendices and/or schedules to this thesis) owns certain copyright or related rights in it (the "Copyright") and s/he has given The University of Manchester certain rights to use such Copyright, including for administrative purposes.

ii. Copies of this thesis, either in full or in extracts and whether in hard or electronic copy, may be made **only** in accordance with the Copyright, Designs and Patents Act 1998 (as amended) and regulations issued under it or, where appropriate, in accordance with licensing agreements which the University has from time to time. This page must form part of any such copies made.

iii. The ownership of certain Copyright, patents, designs, trademarks and other intellectual property (the "Intellectual Property") and any reproductions of copyright works in the thesis, for example graphs and tables ("Reproductions"), which may be described in this thesis, may not be owned by the author and may be owned by third parties. Such Intellectual Property and Reproductions cannot and must not be made available for use without the prior written permission of the owner(s) of the relevant Intellectual Property and/or Reproductions.

iv. Further information on the conditions under which disclosure, publication and commercialisation of this thesis, the Copyright and any Intellectual Property and/or Reproductions described in it may take place is available in the University IP policy IP Policy (see http://documents.manchester.ac.uk/DocuInfo.aspx?DocID=487), in any relevant Thesis restriction declarations deposited in the University Library, The University Library's regulations (see http://www.manchester.ac.uk/library/aboutus/regulations) and in the University's policy on Presentation of Theses.

ACKNOWLEDGEMENTS

Foremost, I would like to thank my supervisor Professor Mohamed Missous, for his patience and continuous support, motivation and immense knowledge. Is an honour for me to work under his supervision.

I am also grateful to my advisor Dr. Max Migliorato for his comments, corrections and valuable discussions concerning my research. My sincere thanks also go to Dr. Peter Carrington, Dr. Daniel Donoval, Dr. Jaroslav Kovac and Dr. Miroslav Mikolasek for their valuate contributions and their help in the devices characterisation.

It is a pleasure to thank CONACyT Mexico and SEP Mexico, which made this project possible by supporting my research financially. Without their support, this project would not have been possible.

I thank my colleagues in the School of Electrical and Electronic Engineering for the stimulating discussions and for all the fun we have had in the last three years.

I would like to express my gratitude to Dr. Teresa Alonso and all the LAPP University of Manchester Committee that helped me since I arrived in Manchester.

I want to thank as well Dr. Jorge Sosa Pedroza, for his friendship, motivation, confidence and spiritual support.

Last but not least, I would like to thank my family, fiancé and friends for supporting me spiritually throughout my life.

PUBLICATIONS

Publications

1. E. Garduño-Nolasco, P. J. Carrington, A. Krier and M. Missous. “Characterisation of InAs/GaAs quantum dots intermediate band photovoltaic devices”, IET Optoelectronics, pages. 71-75, 2014. Volume 8, Issue 2. DOI: 10.1049/iet-opt.2013.0056 , Print ISSN 1751-8768, Online ISSN 1751-8776
2. E. Garduño-Nolasco, M. Missous, Daniel Donoval, Jaroslav Kovac and Miroslav Mikolasek. “Temperature dependence of InAs/GaAs Quantum Dots solar photovoltaic devices”, Journal of Semiconductors IOP, Volume 35, Issue 5, 2014, doi:10.1088/ 1674-4926/ 35/5/054001
3. E. Garduno-Nolasco and M. Missous, “Silicon Nitride anti-reflective coating for intermediate band InAs/GaAs PV devices”, IEEE Proceedings, Pages 380 – 385, Print ISBN: 978-1-4799-1460-9, DOI: 10.1109 /ICEEE.2013.6676062
4. E. Garduño-Nolasco, M. Missous, Daniel Donoval, Jaroslav Kovac and Miroslav Mikolasek “Variable temperature photocurrent characterization of quantum dots intermediate band photovoltaic devices”. SPIE Photonics Europe 2014. SPIE Proceedings 9140, Photonics for Solar Energy Systems V, 914009 (May 15, 2014), doi: 10.1117/12.2052826
5. E. Garduño-Nolasco, M. Missous, Daniel Donoval, Jaroslav Kovac and Miroslav Mikolasek, “Temperature efficiency dependence of intermediate band GaAs/InAs Quantum Dots Photovoltaic Devices”, HETECH 2013 Conference proceedings

Conference contributions

- E. Garduño-Nolasco, M. Missous, Daniel Donoval, Jaroslav Kovac and Miroslav Mikolasek. (2013). Temperature efficiency dependence of intermediate band GaAs/InAs Quantum Dots Photovoltaic Devices. Presented at HETECH 2013. University of Glasgow in Scotland: HETECH. eScholarID:205676 2013 Conference contribution
- E. Garduño-Nolasco and M. Missous. (2013). AR coating design for GaAs/InAs Quantum Dots intermediate band Photovoltaic Devices. Presented at UK Semiconductors 2013. Sheffield Hallam University. eScholarID:205661 2013 Conference contribution
- Edson Garduno-Nolasco P. Carrington, A. Krier and M. Missous. (2013). Characterisation of long wavelength Photovoltaic devices based on GaAs/InAs Quantum Dots. Presented at Quantum Dot Day Meeting 2013. University of Nottingham, UK. eScholarID:190282 2013 Conference contribution
- Edson Garduno-Nolasco P. Carrington, A. Krier and M. Missous. (2013). Characterisation of GaAs/InAs Quantum Dots Photovoltaic Devices. Presented at Semiconductor and Integrated Opto-electronics (SIOE 2013). University of Cardiff, UK. eScholarID:190283 2013 Conference contribution
- E. Garduño-Nolasco and M. Missous. (2013). Silicon Nitride anti-reflective coating for intermediate band InAs/GaAs PV devices. Presented at CCE 2013 International IEEE Conference. Instituto Politecnico Nacional, Mexico DF: IEEE. eScholarID:205674 2013 Conference contribution
- Edson Garduño-Nolasco and M. Missous. (2012). Characterisation and SILVACO modelling of Photovoltaic devices based on the InGaAs-InAlAs material systems. Presented at UK Semiconductors 2012. University of Sheffield, UK. eScholarID:190284 2012 Conference contribution
- Edson Garduño-Nolasco, Professor M. Missous. (2012). Characterisation and SILVACO modelling of Photovoltaic devices based on III-V semiconductors material. Presented at PGR poster conference 2012. University of Manchester. eScholarID:190279 2012 Conference contribution

- Edson Garduño-Nolasco and M. Missous, “Characterisation and SILVACO modelling of Photovoltaic devices based on III-V semiconductors material”, PGR University of Manchester Conference 2012, University of Manchester, Poster presentation.

- Edson Garduño-Nolasco and M. Missous, “Characterisation and SILVACO modelling of Photovoltaic devices based on the InGaAs-InAlAs material systems”, UK Semiconductors 2012, University of Sheffield, Poster presentation.

- Edson Garduno-Nolasco P. Carrington, A. Krier and M. Missous, “Characterisation of long wavelength Photovoltaic devices based on GaAs/InAs Quantum Dots”, Quantum Dot Day Meeting 2013, Nottingham, UK, November 2012, Oral presentation.

- Edson Garduno-Nolasco P. Carrington, A. Krier and M. Missous, “Characterisation of GaAs/InAs Quantum Dots Photovoltaic Devices“, Semiconductor and Integrated Opto-electronics (SIOE ’13), University of Cardiff, Wales, April 2013, Oral presentation.

CHAPTER 1

INTRODUCTION

1.1 Overview

Solar cells based on III-V compound semiconductor materials are excellent candidates for renewable energy generation. GaAs-based photovoltaic devices have demonstrated excellent efficiency and stability at high temperatures that makes them the in fact a good choice in high end solar concentrator applications. The wealth of optical and electrical properties of III-Vs using state-of-the-art in material synthesis technology, such molecular beam epitaxy (MBE), gives the opportunity for further improvements in cell efficiency and cost reductions. Particularly, the introduction of InAs quantum dots (QDs) into the GaAs lattice extends the absorption of the device out into the near infra-red and consequently the photovoltaic device efficiency is enhanced.

This project is concerned with a systematic investigation of the properties of InAs QD systems within GaAs with the aim of achieving an enhancement of solar cell performance. The key challenge is the growth of QDs solar cell structures which exhibit sufficient absorption to increase short circuit current (Jsc) but which can still maintain a high open circuit voltage (Voc). Building upon the University infrastructure, the research involved epitaxial growth using state-of–the-art MBE, optical absorption, photoluminescence and high resolution X-ray diffraction measurements as well as device fabrication and characterization of novel solar cell structures. Optimization was performed on these novel cells to further improve their efficiency by inserting stacks of QD into different regions of the device. The effect of localized doping in such structures was also studied to maintain and enhance the open-circuit voltage which in turn increases the device efficiency.

The fabricated solar cells were characterized using measurements of the dark/light current-voltage (I-V) characteristics and spectral response (4-300 K). Solar cell external quantum efficiencies under standard air mass (AM) 1.5 illumination were also determined

and the suitability of these new cells under solar concentration were assessed. Full physical simulations using SILVACO design software was undertaken to generate models of multi-junction solar cells that were crucial in informing iterations to growth and fabrication and helped to reconcile theory with experiment.

1.2 Aim and objectives of the project

- Comparison of state of the art semiconductor III-V photovoltaic devices and study the different techniques used to date to enhance the efficiency of these devices. These techniques use multi-junction solar cells and the insertion of quantum wells. At least one of the techniques will be used in this project to improve the efficiency of III-V semiconductor compounds solar cell.

- Ability to fabricate solar cell devices, as well as characterize the materials by studying their structural, optical and electrical properties.

- Develop reliable simulations of materials in order to predict the behaviour of the devices. In this way it is possible to design optimal solar cell devices by avoiding material wastage and reduce fabrication costs.

1.3 The studied samples

Several samples using either Indium Phosphide (InP) or Gallium Arsenide (GaAs) substrates were used in this project. The studied samples were grown using molecular beam epitaxy (MBE) techniques on two different MBE systems which are the RIBER V90H MBE (VMBE referred ID) and RIBER V100 MBE (XMBE referred ID). The studied materials can be grouped in two categories as follow.

1.3.1 Quantum wells materials

Several materials grown on GaAs and InP substrates were grown using quantum wells (QWs) structures. The samples VMBE1661 and VMBE928 were grown on highly doped

GaAs n-type substrates. These two structures consist of QWs repeated 50 times. The quantum wells were grown between doped $Al_{0.3}Ga_{0.7}As$ layers (*p* and *n* types). The Aluminium composition for all the layers was set up at 0.3. The main difference between the two samples resides in the growth temperature; VMBE1661 was grown at ~670 °C and VMBE928 at ~580 °C. See Table 1

Table 1 Structure details for GaAs system based samples. VMBE928 GaAs/AlGaAs MQW (50) (grown at ~580C), VMBE1661 GaAs/AlGaAs MQW (50) (grown at ~670C)

	Layer	Thickness (Å)	Doping
	GaAs	200	p-type
	$Al_{0.3}Ga_{0.7}As$	2000	p-type
	$Al_{0.3}Ga_{0.7}As$	300	
x50	$Al_{0.3}Ga_{0.7}As$	65	
	GaAs	85	
	$Al_{0.3}Ga_{0.7}As$	300	
	$Al_{0.3}Ga_{0.7}As$	5000	n-type
	GaAs	2000	n-type
	GaAs	0.35 µm	n+

Four additional samples were grown on InP substrate. These are InGaAs/InAlAs p-i-n quantum wells structures. The structures details are presented in Table 2. VMBE2016 consists of a p-i-n lattice matched $In_{0.53}Ga_{0.47}As$-$In_{0.52}Al_{0.48}As$ structure and it is used as a control sample. VMBE2017, consists of 15 QWs $In_{0.4}Ga_{0.6}As$-$In_{0.52}Al_{0.48}As$ (tensile strained). In XMBE242, the number of QWs layers is increased up to 25 using a lattice matched system $In_{0.53}Ga_{0.47}As$-$In_{0.52}Al_{0.48}As$. Finally, XMBE245 is a 25 QWs compressively strained using $In_{0.7}Ga_{0.3}As$-$In_{0.52}Al_{0.48}As$.

The InGaAs/InAlAs system has been used in order to extend the absorption range in the infra-red. The InGaAs/InAlAs structures exhibit better absorption in the infrared spectrum, which is highly desirable because the cell can absorb lower energy light than GaAs/AlGaAs devices.

Table 2 Structure details for InP based samples. All samples are grown at ~500C

			VMBE2016 Control		VMBE2017 x15 QWs		XMBE242 x25 QWs		XMBE245 x25 QWs	
	Layer	Type	d (Å)	x	d (Å)	x	d (Å)	x	d (Å)	x
	$In_xGa_{1-x}As$	p	750	0.52	750	0.52	750	0.52	750	0.52
	$In_xAl_{1-x}As$	p	100	0.25	100	0.28	100	0.28	100	0.28
	$In_xAl_{1-x}As$	i	2000	0.52	2000	0.52	2000	0.52	2000	0.52
	$In_xAl_{1-x}As$	i	No QWs layers 3500 $In_{0.52}Al_{0.48}As$ layer instead		100	0.52	100	0.52	100	0.52
QW	$In_xAl_{1-x}As$	i			150	0.52	150	0.52	150	0.52
QW	$In_xGa_{1-x}As$	i			100	0.4	100	0.4	30	0.7
	$In_xAl_{1-x}As$	i			100	0.52	100	0.52	100	0.52
	$In_xAl_{1-x}As$	n	10000	0.52	10000	0.52	10000	0.52	10000	0.52
	$In_xAl_{1-x}As$	n	2500	0.52	2500	0.52	2500	0.52	2500	0.52
	InP	n+	0.5um Substrate							

1.3.2 Quantum dots materials

Different InAs/GaAs quantum dot samples were grown on 100mm GaAs highly doped n-type substrates using the RIBER V100H system. The samples consist of 20-period quantum dots arrays vertically stacked. The difference between the growth samples lays mainly in the inter-dot doping profile, the InAs layer thickness (Table 3) and the vertical periodicity (Table 4) of the quantum dot layers.

Sample XMBE288 is an undoped InAs/GaAs in which the InAs layer thickness is 2.7 ML. XMBE291, also undoped and with InAs(2.1 ML)/GaAs, (XMBE293) has a $8x10^{10}$ cm^{-2} n-doping InAs(2.02 ML)/GaAs and (XMBE293) has $16x10^{10}$ cm^{-2} n-doping InAs(1.98 ML)/GaAs. All these structures are summarised in Table 3. The QD layer thickness is critical for the material performance, the optimal value was found to be around 2 ML [1]. The inter-dot doping has been shown to enhance the open circuit voltage [2]. A 300 Å p-$Al_{0.6}Ga_{0.4}As$ layer is used as window for surface recombination reduction purposes.

In addition to the inter-dot doping study, different periodicities were tested in the vertical array in order to find the optimum value. In the past, it has been found that the number of layers and the vertical quantum dots periodicities are critical parameters that can impact the energy conversion efficiency [3].

Table 3 InAs/GaAs Quantum Dot epitaxial structures details for samples XMBE288, XMBE291, XMBE293 and XMBE294. The δ-doping layer varies for each sample. The wetting layer thickness is ~2ML for samples XMBE291, XMBE293 and XMBE294; for sample XMBE288 the wetting layer thickness is ~2.7ML.

			Sample			
		d	**XMBE288**	**XMBE291**	**XMBE293**	**XMBE294**
	GaAs	500 Å	p-type $1x10^{19}$			
	$Al_{0.6}Ga_{0.4}As$	300 Å	p-type $5x10^{18}$			
	GaAs	1000 Å	p-type $5x10^{18}$			
	GaAs	90 Å				
x20	GaAs	250 Å				
	δ doping layer		0	0	$8x10^{10}cm^{-2}$	$16x10^{10}$ cm^{-2}
	GaAs	250 Å				
	InAs	→	2.70ML	2.10ML	2.02ML	1.98ML
	GaAs	90 Å				
	GaAs (Si)	3000 Å	n-type $1x10^{18}$ cm^{-3}			
	GaAs (Si)	2000 Å	n-type $5x10^{18}$ cm^{-3}			
	GaAs (Si) Subs.					

Table 4 InAs/GaAs Quantum Dot epitaxial structures details for samples XMBE312, XMBE322, XMBE311 and XMBE291. All of these samples includes a doping profile within the structure. The main difference between each sample is the periodicity of the QD layers.

	Sample				
	d	**XMBE312**	**XMBE322**	**XMBE311**	**XMBE291**
GaAs	500 Å	p-type $1x10^{19}$ cm^{-3}			
$Al_{0.6}Ga_{0.4}As$	300 Å	p-type $5x10^{18}$ cm^{-3}			
GaAs	1000 Å	p-type $5x10^{18}$ cm^{-3}			
GaAs	90 Å				
GaAs	250 Å	No QDs	Periodicity x5	Periodicity x10	Periodicity x20
GaAs	250 Å				
InAs	→				
GaAs	90 Å				
GaAs (Si)	3000 Å	n-type $1x10^{18}$ cm^{-3}			
GaAs (Si)	2000 Å	n-type $5x10^{18}$ cm^{-3}			
GaAs (Si) Subs.					

Recalling the key issue of the present project, it is absolutely necessary to find the optimum number of layer that should be vertically stacked in order to get the highest

available energy conversion rates. Thus, three more samples were grown. These samples have different vertical periodicity. The sample XMBE312 is the control sample. This sample has no QDs within the lattice, so its optical and electrical behaviour can be compared with samples with 5, 10 and 20 quantum dot vertically stacked layers (respectively XMBE322, XMBE311 and XMBE291). The structural details for these 4 samples are shown in Table 4.

1.4 Outline of the thesis

The present work is organized in 6 chapters. The introduction and the objectives of the project are presented in Chapter one. This includes the details of the studied samples as well as the thesis outline including both quantum well and quantum dot structure groups. Chapter two includes an extensive literature review in which different types of solar cells are described. Chapter two is the synthesis of several scientific contributions in the last few years in semiconductors photovoltaic devices. The fabrication process is described in chapter three, in which the details of each step of the fabrication is presented. This chapter also presents the experimental techniques that are used to characterise the devices and the cell designs .The final recipe for solar cells is shown in Appendix A Mask Designs. The results of the characterization of the fabricated solar cell devices using Quantum Wells structures are presented in chapter 4. A comparison between the results is included within the chapter and the optimisation process attempting to improve the devices energy conversion efficiency is described. Also, data analysis and detailed discussions are presented. In addition, the further details of the optimisation process are presented in Appendix C. Chapter 5 presents the temperature dependence measurements characterisation of several InAs/GaAs quantum dots solar cell devices. The devices, without anti-reflective coating (ARC) and with cylindrical geometry, were fabricated and characterised *on-wafer* under 20 suns conditions in the temperature range from 50K to 430K. The temperature dependence parameters such as open-circuit voltage (Voc), short-circuit density current (Jsc), Fill Factor (FF) and Efficiency (η) were studied in details. The increase of temperature produces an enhancement of the short circuit current. However, the open circuit is degraded because the temperature increases the non-radiative recombination phenomena involved as well as reduces the effective band gap of the semiconductor. Finally, Chapter 6 summarises the obtained results and appraises the main findings and achievements of the research undertaken. Future work is also discussed.

CHAPTER 2

LITERATURE REVIEW

2.1 Introduction

Modern life requires ever greater amount of energy usage. Thus, it is necessary to replace existing sources, which are mostly fossil fuels, with alternative ones which are friendlier to the environment. In addition fossil fuels are not abundant in nature and their finite amount requires the development of renewable energy sources. One of the most important renewable energy sources is the electromagnetic energy from the sun. Some authors point that the sun can generate enough energy per day or even hour to supply sufficiently the needs of the whole of societies worldwide [4]. Furthermore, Solar energy is necessary not only on earth but in space applications as well. In space, the principal energy source for electronic circuits is the sun.

Devices which are able to convert the sun energy (electromagnetic waves) into electrical energy are generally called photovoltaic devices (PV), solar cells (SC) or photovoltaic cells (PVCs). The requirements of a PV device are:

- High efficiency
- Low cost
- Environment resistance (durability)
- Easy fabrication method

Concerning photovoltaic devices we can find different types, where the energy process conversion is different for each of them. This section presents an overview of such devices and the state of the art in PVs.

2.2 Photovoltaic thermal systems

The photovoltaic thermal systems (PVTs) are devices capable of converting electromagnetic waves from the infrared wavelength range (heat irradiated) into electricity. The ground state of the material is excited by the heat received and free charge carriers are generated. Thus, the free charges flow through the anode contact to a circuit and return from the cathode contact.

The materials used to fabricate thermal PV modules are generally crystal silicon. Thermal photovoltaic device modules present efficiencies not greater than 10.7%, under AM0 spectrum, which is a very good value for commercialization of these thermal modules. These high efficiencies can be achieved by using double sided PV, where energy can be generated on both sides of the module. In that case the module is known as 'bifacial' [5]. Another way to improve the efficiency of the PV modules is the use of light concentrators (collectors) in order to excite the back side of the module as shown in the Figure 1. The collector can have many forms that depend upon the physical dimensions requirements and the creativity of the designers, which is crucial in order to increase the module efficiency. The earth inclination plane, the geographical localization of the module and the size of the module must be taken into account when the reflector is designed. With a good collector configuration, the thermal PV modules can deliver up to 17% efficiency [6]. In addition, a mechanical system needs to be installed for positioning the module and because of that the cost of solar collectors increases.

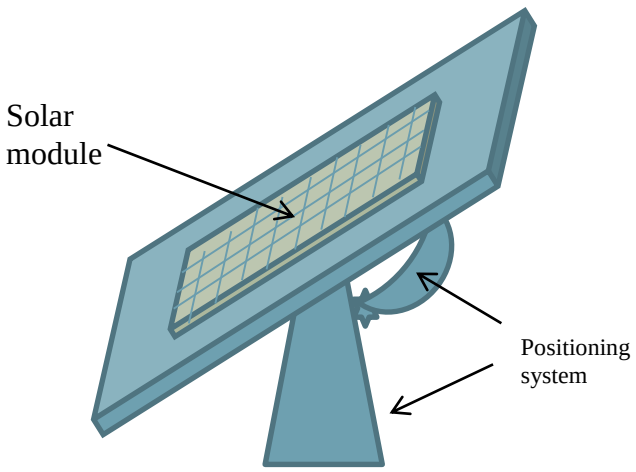

Figure 1 Thermal PV module with positioning system [6]

One of the disadvantages of these systems is the need for cooling because they usually operate at temperatures between 25 ^{0}C and 55 ^{0}C (300 – 340 ^{0}K) [7] , which consequently increase the fabrication and installation costs.

2.3 Organic devices

Other kind of photovoltaic devices are based on organic devices. These PV devices have been popular because of their ease of fabrication, low cost and mechanic flexibility. In such devices, the active material layer can be grown on the top of a flexible substrate [8]. The active layer consists of organic material (polymer) such as poly (2-methoxy-5-(20-ethyl-hexyloxy)-1,4-phenylene-vinylene)(MEH-PPV) and (6,6)-phenyl C61-butyric acid methyl ester (PCBM) [9], neat polythiophene (PT) [10] and efficiencies of an individual cell can reach up to around 4%. The highest efficiency reported is 6.5% using tandem structures [11].

Although the efficiency of these PV devices is generally low, the fabrication of a wide area module based on organic cells enhances the amount of electrical energy generated. Moreover, their mechanic flexibility eliminates the possibilities of module breakage.

The contacts to these devices must be made of a conductive material in order to facilitate charge extraction and carriers injection. Because of this, a layer of indium tin oxide (ITO) is used on the top of the active layer. Unfortunately, ITO is expensive and an alternative is a conductive polymer layer. This layer can be a poly (3, 4-ethylenedioxythiophene): poly (styrene sulfonate) (PEDOT:PSS). It was found that substituting the ITO layer for PEDOT layer reduces significantly the conversion efficiency; however the use of ITO with PEDOT on the top increases the conversion efficiency [12].

Nowadays, hybrid organic PV devices, with the presence of inorganic semiconductors on classical structures, are developed and the energy conversion efficiency has been improved. Zinc oxide along with copper phtalocyanine is one of the combinations used in hybrid devices, with the Zinc oxide being the inorganic semiconductor. The efficiencies achieved by these hybrid devices are around 4% using heterojunctions techniques [13].

2.4 Semiconductor Crystal devices

The electron behaviour in semiconductors depends on its boundary conditions. The atom itself exhibits a single energy level but in a crystal lattice (matrix of atoms) the energy varies due to lattice interaction between the atoms. So, the energy of the atom has continuous values, with forbidden energies between the valence and conduction bands.

At room temperature (300 °K) the valence band is fully occupied by electrons while the conduction band is mostly empty (for intrinsic materials). The conduction band can be occupied by electrons even when no external electrons are injected. This is possible with electrons excitation from the valence band to the conduction band made possible by the presence of a sufficient external energy. The energy required to take an electron from the valence band to the conduction band depends on the semiconductor's band gap and it is different for different semiconductors (Table 5).

Table 5 Band gap of semiconductors materials [14]

Material	Band gap (eV)
Indium arsenide (InAs)	0.36
Germanium (Ge)	0.67
Silicon (Si)	1.11
Indium phosphide (InP)	1.35
Gallium arsenide (GaAs)	1.43
Cadmium telluride (CdTe)	1.49
Aluminium antimonide (AlSb)	1.6
Cadmium selenide (CdSe)	1.73
Selenium (Se)	1.74
Aluminium arsenide (AlAs)	2.16
Gallium phosphide (GaP)	2.26
Aluminium phosphide (AlP)	2.45
Silicon carbide (SiC)	2.86
Zinc oxide (ZnO)	3.37

Silicon cells

Silicon has been demonstrated to be an excellent semiconductor for making solar cell devices despite its indirect band gap. Silicon has advantages in PV devices design as it can present high open circuit voltages (Voc) characteristic, which is favourable for PV devices. Furthermore, the silicon semiconductor devices business has grown up in the last

decades to such a level that the cost to fabricate silicon solar cells has been reduced dramatically.

An individual silicon solar cell (SSC) can generate a Voc up to 0.6 volts. By connecting individual cells in cascade, higher voltage sources can be reached. The amount of current available in these devices depends directly on the amount of light falling on them.

In 1984, Tom Tiedje reported the maximum efficiency for silicon solar cells. The defined limit was 29.8 %, based on his Auger recombination measurements and AM1.5 absorption in crystalline silicon [15]. The above mentioned theoretical limit was found by including the recombination phenomena involved within the material such as Auger recombination and radiative losses. In addition, the optical measured data was used in the numerical analysis. These side effects can be produced by the deposition of contacts (sometimes aluminium is used to diffuse the metal on the silicon layer) [16].

Many material modifications and different cell configurations have been tested in order to improve the energy conversion efficiency. As it is well known, silicon has an indirect band gap necessitating thick layers in order to get a good absorption, but if this thickness is reduced at least at the 10% level the silicon wafer is still able to generate almost the same energy yielding thin silicon solar cells. Thin silicon solar cells can have efficiencies up to 16.6% using PECVD passivation oxide and reducing optical losses [17].

Thin n-type silicon layers can be grown on highly doped p-type silicon substrates by using lateral overgrowth (ELO) epitaxial growth. These thin film solar cells exhibited an enhanced Voc compare with typical silicon cells due to the saturation current reduction. The latter leads to achieve higher efficiencies up to 16.9%y [18].

2.5 III-V Semiconductors PV devices

The highest efficiencies reported for solar cells have been fabricated with materials of the III and V semiconductors. It has been predicted, that for 6-multi-junction III-V semiconductor photo material, theoretical efficiencies of up to 56% can be reached [19]. These solar cells are fabricated for high power requirements of space applications. The optimal energy for sun energy conversion for a single layer solar cells is 1.4 eV (this will be explained in detail in the next chapter) so III-V semiconductor such as Gallium

Arsenide (GaAs) are perfect for sun energy conversion with an energy band gap of 1.43. GaAs is not the only semiconductor to have an optimum energy band gap for solar energy conversion but there are some other III-V semiconductors compounds* such as Gallium Indium Phosphide ($In_xGa_{1-x}P$), Gallium Indium Arsenide ($In_xGa_{1-x}As$), Aluminium Indium Arsenide ($In_xAl_{1-x}As$) and Gallium Aluminium Arsenide ($Al_xGa_{1-x}As$) that are also excellent materials for solar cell usage.

III-V solar cells have many advantages; including these are the use of thin layers (as most have a direct band gap), lightweight and high radiation resistance. However, each crystal has a different lattice constant which limits in practise the possible options to combine materials for fabrication of multi-junction solar cells. This is because lattice match ensure high quality crystals, reducing dislocations and increasing the absorption [20]. There are combinations that work well, for example, InGaP-InGaAs, InGaAs-GaAs, InGaAs-InAlAs at certain compositions.

After the growth of the solar cell the substrate can be removed in order to transfer the solar cell to a different (cheaper) substrate, this substrate could be glass or any reflective material. The purpose of doing this is to reflect the light that wasn't absorbed by the cell layers, so it can enhance the amount of light absorbed. By using reflective substrates thinner layers are required, avoiding crystal dislocations for mismatched materials but, however, reducing the material light absorption. So, this technique is perfectly applicable to mismatched lattice thin film solar cells. [21]

2.5.1 GaAs Solar cells

Gallium Arsenide (GaAs) is a direct band gap semiconductor with energy band gap of 1.43 energy (eV) at 300 K. GaAs absorption levels are approximately 10 times greater than those of silicon so thinner layers are sufficient and this reduces the cells weight. In solar cells some scattering effects depends on operating temperature. That is the case for carrier recombination which increases directly in proportion to the temperature. As GaAs temperature coefficient (the rate of decrease of efficiency with temperature) is lower

* The band gap of the semiconductor compound will vary with the 'x' composition value.

compared with the one for silicon, the GaAs solar cells exhibit better conversion rates as the temperature increases. [22]

The use of Si as a substrate is possible for GaAs solar cells, and it has been reported that GaAs/Si devices are more resistive to radiation than GaAs/GaAs devices. However, the differences in Si and GaAs lattice constants generate dislocations in the device which reduce the minority-carriers diffusion length. In order to reduce the dislocation density some changes are made in the growing material process, including InGaAs/GaAs strain-layer superlattice (SLS) systems as shown on Figure 2. Thus, these devices can get efficiencies up to 20% at AM1.5 [23] but at the cost of a more complex growth process.

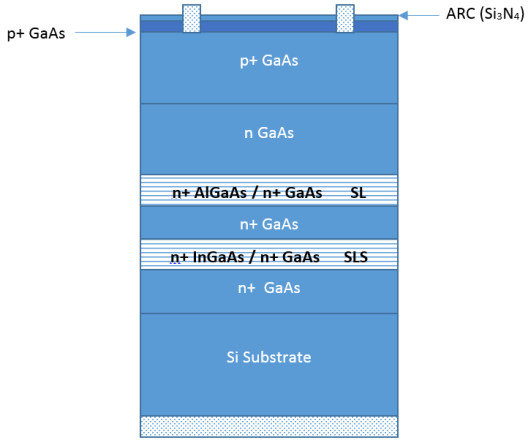

Figure 2 SLS in GaAs-on-Si device for dislocations density reduction [22]

GaAs layers have also been grown on GaAs, Ge (lattice matched), Si and conductive (such as cooper) substrates as well. Growing the GaAs layers on Ge can present different advantages, among them a theoretical efficiency of 35.7 % which is higher than the 27.5 % theoretical efficiency using GaAs substrate largely because the Ge captures a great deal of the long wavelength solar radiation. Using Ge substrates it is also possible to obtain lower weight devices due to the mechanical stiffness of the Ge wafers. Practical efficiencies for GaAs solar cells on Ge (~31%) substrates are higher than on GaAs substrates (~15%). [24]

GaAs-on-Ge solar cells, as was mentioned above, also have the advantage of a low temperature coefficient and high resistance to radiation, however when these devices

operate under high temperature conditions the contacts can diffuse into the GaAs layer but it was shown that this degradation mechanism is moderate [24].

GaAs solar cells can thus be grown on different substrates such as Si, GaAs, Ge, among others, but this substrate can be removed from the device. Once removed, various materials can be used to support the thin film. These materials are glass, metal sheet or plastic sheet. The choice of this new "substrate" material depends on the cost limits of the device or the mechanical requirements for the solar cell uses.

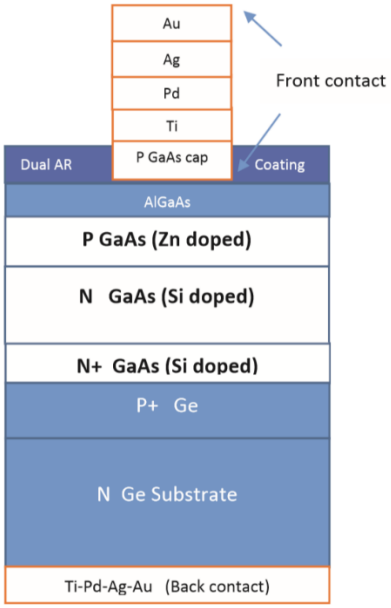

Figure 3 GaAs on germanium with GaAs cap front contact [25]

If a conductive material is used to insert the GaAs thin film it is possible to improve the efficiency of the solar cell. That is because in the metal the heat dissipation is better and this reduce the reverse saturation current. Another reason of this improvement is the mirror effect of the back contact. This mirror effect increases the external quantum efficiency (EQE) due to the extra light absorption. This increase of the EQE can be about 10% in the 700 to 900 nm range. [26] GaAs generates almost all the carriers in only 5 microns because of its very strong optical absorption. So, in electrical sense it is important not to remove all of the substrate. However, when the device is glassed the efficiency drops by 2%. [27]

2.5.2 $Al_xGa_{(1-x)}As$ solar cells

Aluminium Gallium Arsenide ($Al_xGa_{1-x}As$) has a lattice constant very similar to the GaAs lattice constant, so $Al_xGa_{1-x}As$ is a perfect option to grow on GaAs substrate solar cells with resulting high quality crystals , avoiding dislocations.

The energy bandgap changes from 1.43 to 2.16 as a function of the 'x' composition value (Figure 4). If $Al_xGa_{1-x}As$ is grown on GaAs it will enhance the operational wavelength range of the device and the recombination on the boundary (GaAs- $Al_xGa_{1-x}As$ junction) is reduced as well. [28]

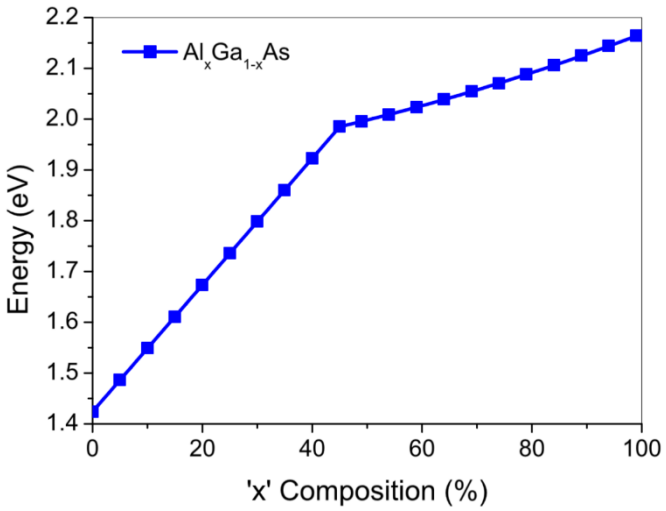

Figure 4 $Al_xGa_{1-x}As$ bandgap [29]

The surface recombination is one of the most fundamental limiting factors for high efficiency GaAs solar cells. One way to control this effect is by growing a layer of $Al_xGa_{1-x}As$ on the top of GaAs solar cell and this then can increase the energy conversion efficiency by up to 20%. [30]

Enhancing the efficiency of solar cell based on GaAs can also be achieved by different techniques, one being the insertion of lenses into the device (increases the efficiency from 9 to 13 per cent) [31] or the use of concentrator in order to increase the thermal activated devices [32]. Another option to increase the efficiency of the solar cell is connecting them in cascade of 2 or more solar cells. Here, the problem is the losses due to the contacts between the two cells (Figure 5). This can be solved using tunnelling junctions such that high current can be produced by small voltages values. These tunnelling junctions must

be the same material used in the device. In the case of $Al_xGa_{1-x}As$ -GaAs cells, values of Al (composition) up to 0.4 have been reported to be the best tunnelling junction; when Al concentration is high the fabrication becomes more difficult. The effectiveness of the junction depends on the composition value, so it is important to know what happens near to 0.45. At that point, when the composition is relatively high the electron density is reduced and the tunnelling current is reduced as well due to the junction width increment. Therefore it is important to have abrupt junctions for the tunnelling. [33]. x=0.45 is also the composition at which $Al_xGa_{(1-x)}As$ becomes indirect bandgap semiconductor.

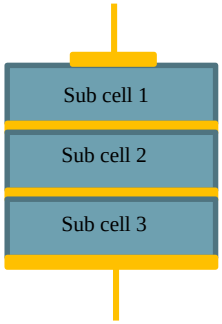

Figure 5 Cascade solar cells

The insertion of multiple quantum wells (MQW) to improve the efficiency is achieved by introducing them in a p-i-n junction. In [34], Stephen M. Ramey demonstrated that a single solar cell with MQW has a better efficiency than a single solar cell without MQWs. The critical parameters in order to analyse the structure is the thickness of the wells and the QW number, in addition to other parameters such as recombination and photo generation in the materials. Controlling the first two parameters can improve the efficiency of the device. Increasing the number of QWs increases the absorption of the device. [34]

The quantum well devices are combined with other devices. That is the case of the multi-junction solar cells. It usually consists of three combination cells, top-middle-bottom of different band gaps as shown in Figure 6. [35]

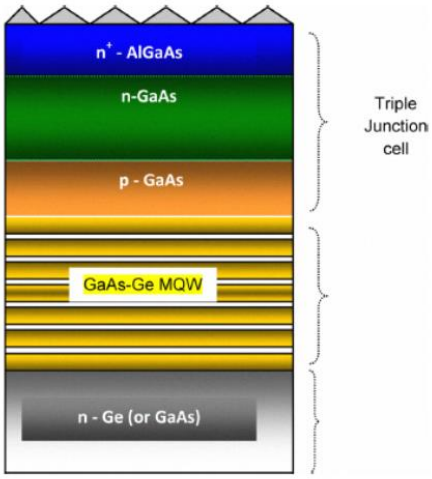

Figure 6 Triple junction solar cell exhibit an efficiency of 44%. [35]

2.5.3 $In_xGa_{(1-x)}As$ Solar cells

Indium Gallium Arsenide ($In_xGa_{1-x}As$) is a III-V semiconductor has a bandgap from 0.36 to 1.42 eV depending upon the composition 'x' value (Figure 7).

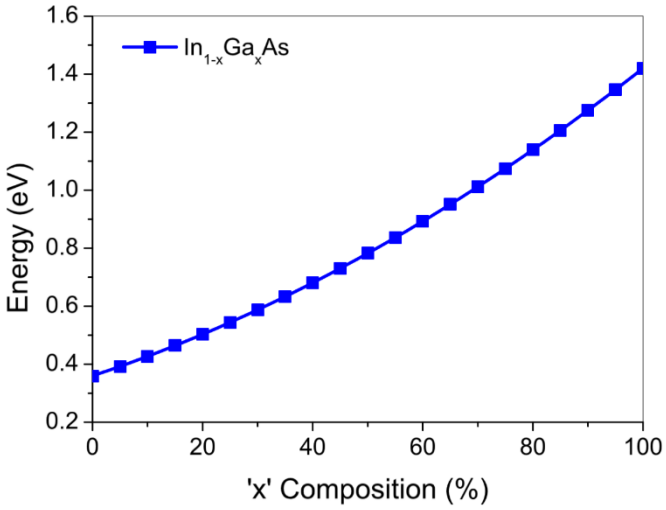

Figure 7 $In_xGa_{1-x}As$ bandgap [29]

In solar cells the energy bandgap of $In_{0.53}Ga_{0.47}As$ is really convenient. Its lattice constant is 4% higher than the GaAs lattice constant but it has the same lattice constant as Indium Phosphide (InP) at 5.8687 angstroms [29]. So, a perfect combination is to grow $In_{0.53}Ga_{0.47}As$ on InP in order to avoid dislocations and in order to have thicker layers to increase the long wavelength light absorption. There are some efforts researching $In_xGa_{(1-x)}As$ growth on GaAs substrates. One way to reduce dislocations is post annealing, or the

insertion of strained layer superlattice (SLS) buffer layer, of course the mismatch depends on the indium concentration. It was found that inserting SLS buffer layers with a low mismatch the dislocations can be reduced in both regions above and below the SLS layer due to the generated electric field. Another possible explanation for this effect is that the SLS-induced strain bends the upper layer strain as reducing the dislocations. [36]

In GaAs/ $In_xGa_{1-x}As$ quantum well devices some parameters such as the composition value 'x' and the thickness of the layers can affect the open circuit voltage of the solar cell. One of these parameters is the well-barrier relation. When the thickness of the QW is small, the solar cell has high energy quantum confinement. It has been found that a single well device present a higher gain in voltage compared with MQW devices. Moreover, concerning the lattice strain, it has been found that by introducing lattice strain the quality of the crystal will limit the device performance due to the possible present dislocations. So, in strained materials, the thickness of the barriers is critical during the design to avoid trapping recombination [37], [38]. A necessary condition for reducing defects within the host lattice is to use thick barriers for a MQW device according to the experimental data presented for F. W. Ragay in [39]. Using $In_xGa_{1-x}As$ material system, multi-quantum wells have been demonstrated to reach efficiencies of 18% similar to the ones presented for Ming-Ju Yang in [40].

It is possible to enhance the conversion range using different III-V group materials with different bandgap. That is the case of the tandem solar cells. Some materials mixed in this manner are ternary and quaternary compounds. One example is the tandem solar cells reported by J. F Geisz in [41] using a triple junction tandem solar cell exhibiting efficiencies up to 40.8% . The triple junction consist of 1 sub cell (bottom cell) of InGaP, a second sub cell (middle cell) of $In_{0.04}Ga_{0.96}As$ and a third sub cell (top cell) of $In_{0.37}Ga_{0.63}As$. The three cells were grown on GaAs substrate leading to a conversion range from 0.89 eV ($In_{0.37}Ga_{0.63}As$) to 1.83 eV ($In_{0.49}Ga_{0.51}P$).

2.5.4 $In_xAl_{(1-x)}As$ Solar cells

Indium Aluminium Arsenide is a ternary semiconductor compound with a lattice constant of 5.86 Å for 'x' composition value of 0.5 and the bandgap varies from 0.36 (x=0) to 2.142 eV(x=1) (Figure 8) and so the absorbed wavelengths from 570 nm (visible spectrum – red colour) to 3.4 μm (infrared spectrum).

The lattice constant of $In_xAl_{(1-x)}As$ compounds allows its growth on InP. $In_xAl_{(1-x)}As$ has not been as extensively studied as the $Al_xGa_{(1-x)}As$ ternary compound. Few data about $In_xAl_{(1-x)}As$ can be found in the literature. The refractive index for two thicknesses of $In_xAl_{(1-x)}As$ (with x within the range from 0 to 1) shown in Figure 9 has been reported by [42]. Some authors report that the optical properties of $InxAl_{(1-x)}As$, for different composition, are directly affected by the Molecular Beam Epitaxy (MBE) growth process in order to have good quality crystals. [43]

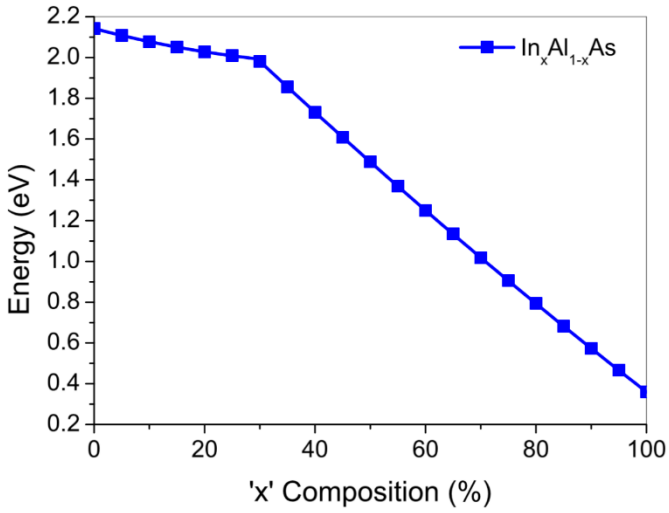

Figure 8 InAlAs bandgap [29]

As used in [43] the growth of $In_xAl_{(1-x)}As$ (Al_x=0.88) on GaAs layer as a buffer, can reduce significantly the dislocations and defects on the substrate-layer interface. So, It is possible to grow $In_xAl_{(1-x)}As$ (Al_x=0.88) layers on GaAs avoiding structural defects (due to the mismatched lattice) by using engineered buffer layers. [44]

$In_xAl_{(1-x)}As$ MQW structures have been investigated with $In_yGa_{(1-y)}As$ obtaining high mobility because of the large discontinuities in the conduction band in these heterojunctions.

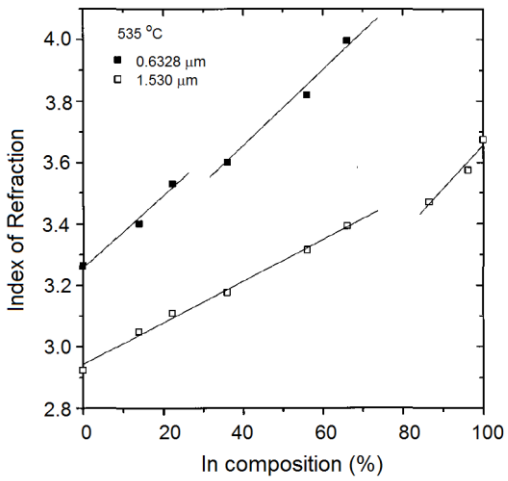

Figure 9 InAlAs refractive index in function of 'x' value composition for two different layer thickness [42]

One of the best combinations between $In_yGa_{(1-y)}As$ and $In_xAl_{(1-x)}As$ is with the compositional values of y=0.53 for $In_yGa_{(1-y)}As$ and x=0.52 for $In_xAl_{(1-x)}As$ to get perfect lattice match between them and also with InP. However, the quantum well can still be mismatch with the barriers by using other compositions. It has been found that barrier and well can have the same width and the composition of the well can be used to modify the optical properties. [45] By varying the indium and aluminium compositions, a rich variety of compounds can be synthesised which can span a very large portion of the sun spectrum.

2.6 Quantum Well devices

The device energy conversion is limited by different parameters, one of these parameters is the material absorption range. So, it is critical to use materials that absorb as much of the sun light spectrum beyond the visible range.

The insertion of quantum wells is one of the ways to enhance the absorption range of the material enabling new sub-band transitions in the material as shown in Figure 10 quantizing the energy levels.

Thus it is possible to enhance the open circuit voltage in InP/InGaAs, $Al_{0.35}Ga_{0.65}As$/GaAs, $Ga_{0.51}In_{0.49}P$/GaAs lattice matched systems due to the reduction of the recombination processes by using free-defects material [46]. In practical photovoltaic devices the Voc and the energy conversion efficiency are improved by using lattice matched material systems getting up to 14% of efficiency with Voc of 1.07 volts as

reported for MQW $Ga_{0.51}In_{0.49}P/GaAs$ lattice matched devices [47]. The latter has been demonstrated by Stephen M. Ramey and Rahim Khoie [48] that the incorporation of QW enhances the energy conversion efficiency of materials by using physic modelling.

Additionally, many efforts have been dedicated to model several MQW structures in order to find the optimal thicknesses of the well and the barriers as it has been found to be critical in the photovoltaic material design [49]. However, modelling materials involves the use of critical numbers such as absorption coefficient, recombination rates and mobility rates which are critical to get reliable results.

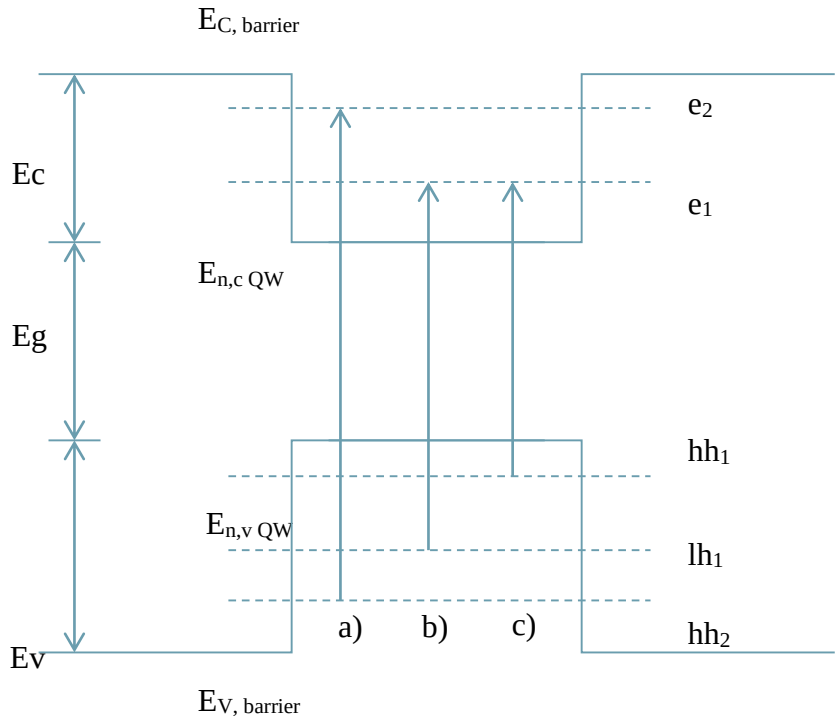

Figure 10 Inter-Subband transitions allowed in quantum well

Recently, D. Teng et al in [50] have been found that the barrier thickness in mismatched systems such as $In_xGa_{(1-x)}As/GaAs$ is critical in order to reduce the recombination and it has been found that the use of thin barriers reduce the recombination rates into the depletion region thus the efficiency can be enhanced. The latter is not really important in free-of-defects material systems [51].

As mentioned previously, the $In_{0.53}Ga_{0.47}As/In_{0.52}Al_{0.48}As$ material system grown on InP substrates gives high quality crystals and they are generally affected by the composition

values used in the barrier layers which generates strained layers affecting the optical properties of the material and allowing the absorption range enhancement [52], [53].

Moreover, to optimize the InGaAs/GaAs multi-quantum well devices it is possible to use solar concentrators systems. It was found by modelling, that multi-quantum well structures can increase the conversion efficiency rates when they are exposed to concentrated light. The temperature dependence efficiency rates for MQW materials is lower than the ones for simple p-i-n GaAs junction devices. It may be due to the thermal energy that enhances the carriers scape in the MQW structure [54]. It can be explained due to the fact of the use of MQW reduces the effective carrier lifetimes resulting in more thermally stable devices as shown in [55] for $Al_{0.36}Ga_{0.64}As$ p-i-n. Additionally, it has been found that by reducing the impurities concentration good photocurrent collection ratios are achieved enabling the short wavelength absorption as demonstrated by Paxman et al in [56].

As much as the growing technology enable it, new configurations are proposed in order to increase the photovoltaic material conversion efficiency. One of these configurations is the use of Bragg reflectors. In InGaP/GaAs MQW material systems such as $Al_{0.13}Ga_{0.87}As$/AlAs with interface layers of $Al_{0.5}Ga_{0.5}As$ enhances the energy conversion efficiency compared with the one achieved by the MQW InGaP/GaAs device without Bragg reflectors. The latter is due to the light trapped enhancement up to around 90% extra in the well region [57], [58].

2.7 Quantum Dot devices

The actual theoretical limits of 31% predicted for a single p-n junction by William Shockley and Hans J. Queisser [59] can be exceeded. By introducing new energy levels in the materials band gap, these devices which are termed "Intermediate band" structures [60] [61] extend the absorption range. It has been predicted that introducing intermediate band materials, the theoretical efficiency limit can increase to 47% for a triple junction configuration [62]. These energy levels can be generated by insertion of Quantum Dots in a host semiconductor structure which can be grown using a range of epitaxial growth techniques. In the case of InAs/GaAs (approximately 7% mismatched system), the Stranski-Krastanov method, which is also known just as S-K method, is commonly used for the synthesis and the result is a high quality and defect-free quantum dots materials.

The S-K technique offers limited tuning possibilities or changes in geometry of the dots, their density and size. More recently doping of InAs/GaAs QD has also been studied showing that the presence of n-type dopants inter dots enhanced the current generation up to the efficiency of 11% [63]**.** The most successful technique to grow quantum dot structures is using epitaxial growth with highly mismatched systems with which vertically stacked QDs layers can be grown. By limiting some dots parameters such as their height, the dots can be vertically aligned. It has been proven in [64] that properly aligned and quite uniform dots lead to very narrow photoluminescence spectral lines. So, vertical alignment is a critical characteristic for structure used for laser devices. However, due to the quantum dot insertion, the PL peaks will suffer an unavoidable shift due to the enhancement in the electrons confinement [65]. Antonio Marti et al [66] found that QD structures can be tuned by inserting n-type atoms into the barriers where the doping level is defined for the inter dot spacing. These devices, known as Intermediate Band (IB) devices, are thermaly stable and they are affected by impact-ionization processes [67], [68]. QD materials are very promising for third generation solar cell applications in which the losses due to the carrier thermalisation is attempted to be reduced.

Many challenges are faced for the quantum dots material implementation regarding the growth process due to the high required precision as well as the many compromises involved in the design such as mobility-conductivity relations [69]. Additionally, by using quantum dot materials, the presence of phonons in the structure is reduced as the controlled inter dot space distance and the well thickness generates higher Jsc levels without Voc degradation [70]. Table 6 below summarises the best efficiencies obtained on the materials described above, including multi-junction cells.

Table 6 Best efficiencies of reviewed publications analysed in chapter 2.

Material	Junction Type	Efficiency (1sun)	Reference
Polycrystalline Si	Single Junction	16.6 %	[17]
Thin crystalline n-Si	Single Junction/Reflector	25.0 %	[18]
GaAs-on-Si	Multi-junction tandem	20.0 %	[23]
GaAs/InGaAs	Multiple Quantum Wells	18.0 %	[40]
$Ga_{0.51}In_{0.49}P/In_{0.04}Ga_{0.96}As/In_{0.37}Ga_{0.63}As$	Triple-junction	33.2 %	[41]
InAs/GaAs	x20 vertically stacked QDs	14.0 %	[70]

CHAPTER 3

EXPERIMENTAL TECHNIQUES

3.1 Introduction

In order to evaluate the performance of the fabricated devices it is necessary to obtain structural, optical and electrical parameters. In this Chapter, the different techniques used to characterise both the epitaxial material and the fabricated devices are described. The optical characterisations are obtained using photoluminescence (PL), absorption, and reflectivity. The structural characterisation consists of Double Crystal X-Ray Diffraction (DCXRD) measurement and the electrical characterisation requires the measurement of fabricated devices under light conditions. Furthermore, the different steps required to fabricate a photovoltaic solar cell device are described.

3.2 Solar cells basics [22]

3.2.1 Basic solar cell

The most basic solar cell is made by one layer of a semiconductor with the back contact and a front contact collector. But in this basic configuration, the efficiency is very low. The p-n junction shows good properties that are suitable to fabricate solar cells. The voltage current characteristic is given by:

$$V_{oc} = \frac{kT}{q} In\left(\frac{I_L}{I_0} + 1\right)$$

Where I_L is the current generated under illumination condition, I_0 is the saturation current.

One important point to notice is that in this type of solar cells the losses due to resistances can be appreciable. From the previous equation, it can be seen that the recombination phenomena (which determines the I_0 value) in the material will limit the open circuit voltage. These parasitic resistances are increased due to the n and p type majority flow of carriers. The basic solar cell is shown in Figure 11.

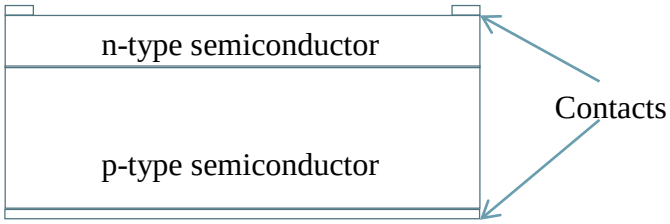

Figure 11 Basic Solar cell structure

3.2.2 IV curves

One of the most important metrics in solar cells is the I-V curves. This curve describes the characteristics of the device. The I-V curve (current-voltage) can be in different forms. In Figure 12 is shown an example of a typical I-V curve. Sometimes these curves are shown with the 'x' axis flipped in order to analyse the characteristics on the first quadrant. From the I-V curve can be extracted information about the electric behaviour of the solar cell.

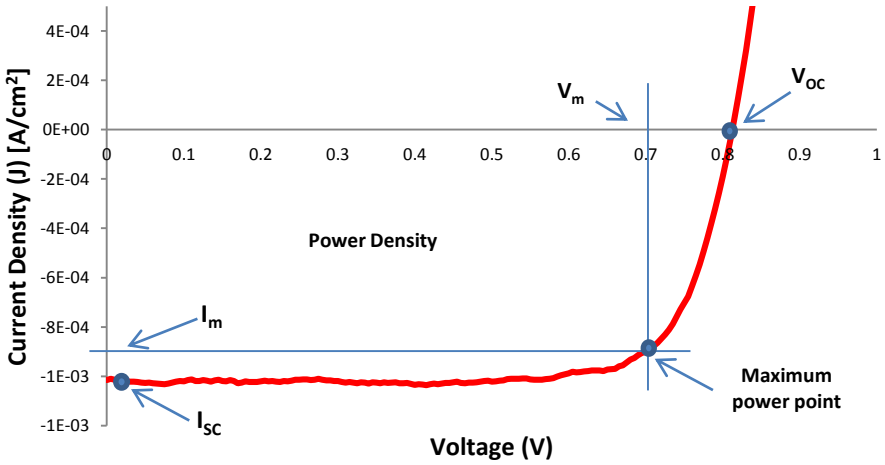

Figure 12 Characteristic IV curve for a photovoltaic solar cell device.

3.2.3 Efficiency

The efficiency of a solar cell is defined as how good it is in converting light energy to electrical energy. It can be calculated as a function of the short circuit current and the open circuit voltage. In terms of the short circuit current, it can be increased by reducing

the bandgap of the material (the short circuit current can be known only if the photons flux of the source is known too). The quantity of electrons excited by the source is integrated over the whole spectrum.

Efficiency calculations

The efficiency of the devices was calculated using:

$$\eta = JscVocFF/Ps \quad \textbf{9}$$

Where:

- η - Efficiency
- Jsc - Short circuit current density
- Voc - Open circuit voltage
- FF - Fill factor
- Ps - Source power

The FF is calculated using:

$$FF = JmVm/JscVoc \quad \textbf{10}$$

Where:

- JmVm - Pm Maximum power point

The source power for 1 sun is 100 mW/cm^2 [22].

The Fill Factor is used to calculate the efficiency of the cell from the IV curve, it is the ratio of the maximum operation point of the device ($J_m V_m$) divided by the $J_{sc} V_{oc}$ product. This figure of merit can describe the efficiency of the device.

However, the efficiency is limited by other factors too, one of these being the reflective properties inherent to semiconductors and contact material leading to some of the light energy being reflected and not passing through the device active layers.

3.2.4 External Quantum Efficiency

The quantum efficiency (QE) gives a complete picture for the performance of the device and therefore can help to improve further the solar cell efficiency. The quantum efficiency

is related to the relationship between the incident light and the photocurrent. The quantum efficiency is divided into internal quantum efficiency (IQE) and external quantum efficiency (EQE). The IQE is defined as:

$$IQE = \frac{\#collected\ carriers}{\#incident\ photons}$$

Mathematically:

$$\text{If } \ Spectral\ Response\ (SR) \ = \frac{I_{sc}}{I_{light}} = \frac{I_{sc}}{P_{in}}$$

$$\text{Then: } IQE = \frac{1}{1-R}\frac{I_{sc}}{I_{light}/E} = \frac{1}{1-R}\frac{hc}{e\lambda}SR$$

In other words the quantum efficiency determines the number of photocarriers generated by the total absorbance of the incident photons. The ideal would be to have a 100% for the quantum efficiency.

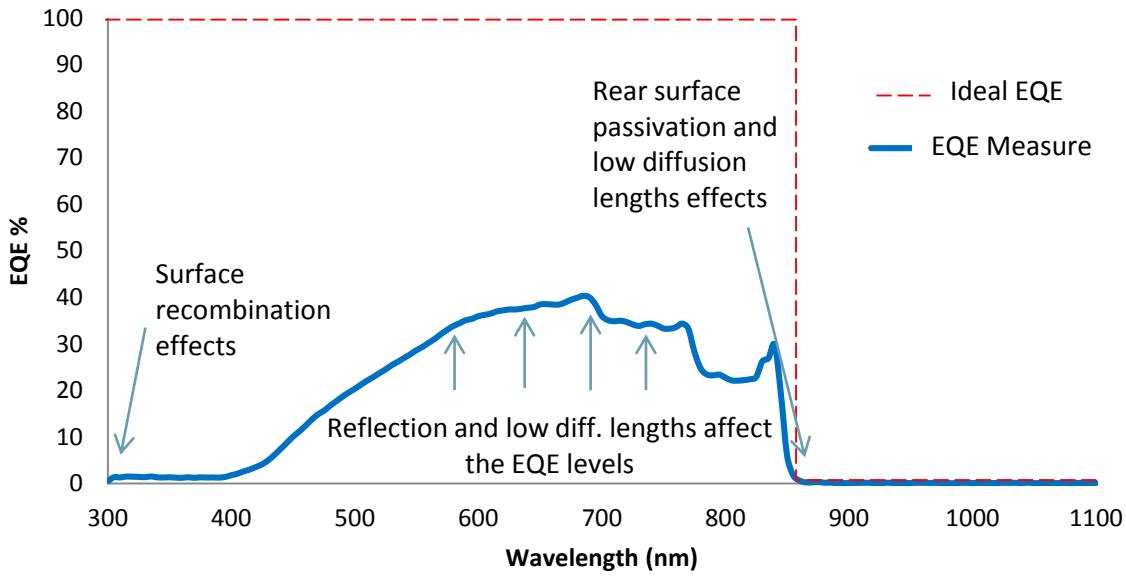

Figure 13 Quantum Efficiency [71]

As shown in Figure 13 the IQE is affected by the front surface recombination velocities in the short wavelengths. That is the reason for using a "window" layer on the top of the solar cell device. The recombination on the rear surface affects the IQE response at high wavelengths. In the case of the long wavelengths (high energy light) the IQE is also affected by the total thickness of the cell [72].

The EQE it is calculated by adding the effects of the reflective properties of the materials to the internal quantum efficiency. Many efforts have been dedicated to find the best way to estimate the EQE by using different mathematical methods as neural networks [73] and resulted in good approximations in solar cells of multiple layers. To measure the quantum efficiency it is necessary to have a complete measurement system. It is necessary to have the complete spectrum data of the power incident light source in order to get the collected carrier density and to get the efficiency [74].

3.3 Solar cells materials preparation

3.3.1 Molecular Beam Epitaxy

Molecular Beam Epitaxy, better known as MBE, is a widely used semiconductor growth technique. It is characterised by large capabilities to control the material composition, layer thickness, interfaces, doping profiles with high accuracy which leads to high quality crystals. The growth process is made under ultra-high vacuum (UHV) conditions which allowed the growth of very clean surfaces free of impurities (understand impurities as undesired contamination particles). It is possible, due to the UHV condition, to insert in the system different sensors that help to monitor and control parameters like thickness, temperature, etc. The latter results within complex materials with high quality.

Figure 14 University of Manchester's Molecular Beam Epitaxy facility

3.3.2 Stranski–Krastanov growth (S-K)

Quantum dots can be fabricated taking advantage of the physical effects of exceeding the critical thickness for two mismatched materials. The result will be the spontaneous formation of random material islands known as Quantum Dots. However, it is not easy to achieve due to the accuracy required during the growing process. For the specific case of the GaAs/InAs quantum dot material studied in the present work, it is necessary to grow them by using Molecular Beam Epitaxy which will generate a high density of self-assembled random dots. That is the case of 7% mismatched where the GaAs (substrate) has lower lattice constant than InAs. The growing involve the control of parameters as temperature, pressure and deposition ratios.

The growing process consist basically in growing an InAs layer on GaAs material layer. This is a system with 7% mismatch and S-K is the actual option to grow high quality QD materials base on InAs/GaAs.

This method relies in the mismatched lattice deposition exceeding the critical thickness. In Figure 15 the S-K process diagram is shown. The process involves the deposition of an InAs(wetting layer) layer on top of a GaAs layer (spacer). Here, the wetting layer thickness is critical to control the dots size. The optimum wetting layer thickness for InAs/GaAs material has been found to be around 2 ML [75] in order to obtain uniform dots. When this thickness is exceeded the dots will not be uniform.

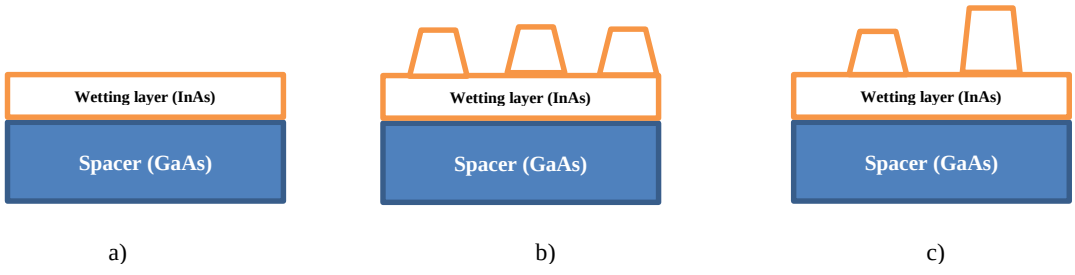

Figure 15 S-K process diagram for different wetting layer thickness a) lower than 1 ML, b) approximately 2 ML and c) higher than 2 ML [75]

3.4 Characterisation

Characterisation is the extraction of important parameters either of the epitaxial wafer or the fabricated device. During the fabrication process or even during the growth process itself, the material properties can be altered. So, the characterisation helps to find out these differences and is thus a powerful tool to design and improve devices. The different procedures shown in this chapter are non-destructive. It means that the measurement never affects the properties of the sample wafer; however some of the presented techniques are contactless and some of them are not such as the I-V measurement procedure due to the applied bias and the probes connected to the solar cell contacts.

3.4.1 PL measurements (Photoluminescence)

Photoluminescence is a non-destructive measurement that gives information about both the discrete energy states and band gap of the material. It is based on the premise that when light is shone on the material (semiconductor wafer) and the incident photon has energy higher than the material band gap an electron is promoted from the valence band to the conduction band. The promoted electron will go back to its relaxed state by losing the extra gained energy via recombination processes. During this process emission of light is possible and this is called radiative recombination.

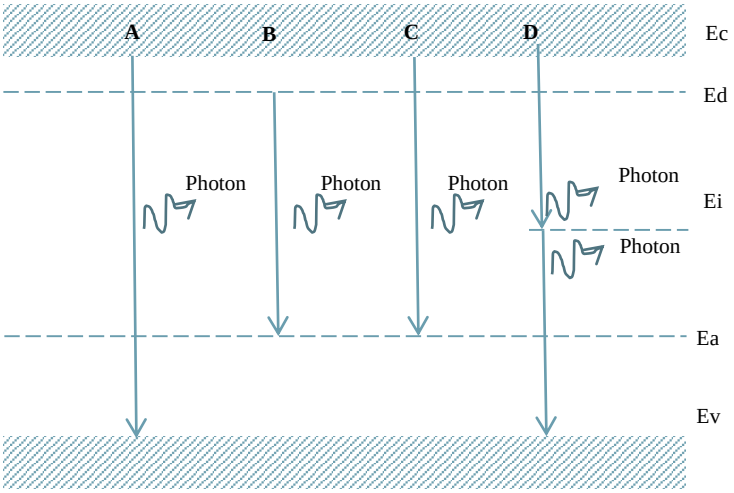

Figure 16 Radiative recombination types: (A) free electron - hole, (B) free exciton, (C) neutral donor to free hole, (D) free electron to neutral acceptor and (E) donor acceptor pair recombination.

The radiative recombination process can occur in several ways in the material. The first one can be via an electron from the conduction band relaxing back to the valence band (Figure 16A), but the electron can also move to the energy level generated by the acceptors in the material (Figure 16C) or the electron can jump to an intermediate energy level (Trap) and generate a photon then jump from the trap to the valence band (Figure 16D). [76] Furthermore the electron can also come from the Energy levels created by the donors (Figure 16B). As shown in Figure 16 each photon generated has different energy depending on the exact process (refer to figure).

To perform the PL measurements a fixed wavelength light source is required. The light absorbed generates movement of electrons between energy levels. Then, by using a broadband light sensor (photodetector), the emitted light generated from the radiative recombination is detected. For this project, the setup used to perform the PL measurements is depicted in Figure 17. The equipment used is the Accent RPM2000™ (Figure 18); two different photodetectors are available which are InGaAs photodiode array (900 to 1800 nm) and Silicon CCD (500 to 1100 nm). A green 532 nm laser (8 mW power) was used as a power light source.

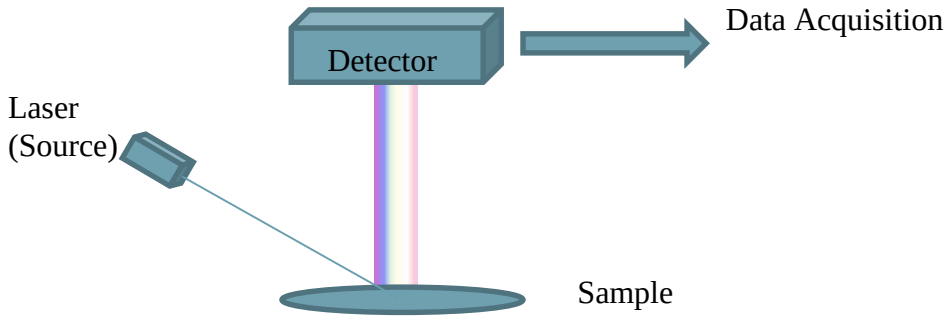

Figure 17 Photoluminescence measurement setup

The measurements were performed at room temperature using the two available photodectectors and it was thus possible to cover the spectral range from 500 nm up to 1800nm. Figure 18 shows a picture of the equipment used to perform the PL measurements.

Figure 18 Accent RPM2000™

3.4.2 Absorption measurements

In optical processes, the absorption coefficient refers to the wavelength which is absorbed by the material; this refers to the energy range that can be absorbed by the solar cell (recalling that the efficiency of the solar cell can be improved by enhancing the wavelength conversion range). The absorbance measurement is a non-destructive procedure.

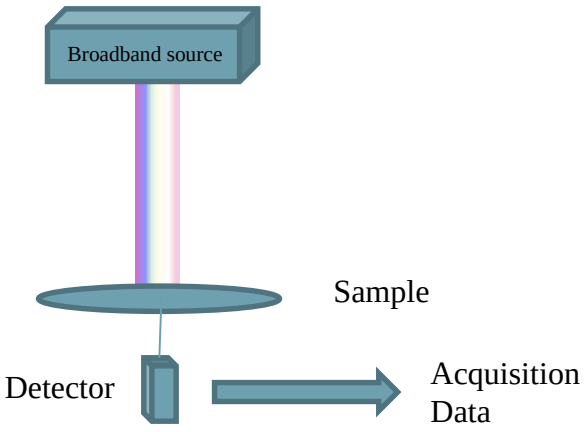

Figure 19 Absorption setup system

The absorption measurements consist of shinning broadband light onto the sample surface. Only some percentage of this light will pass through the material and the rest will be either reflected or absorbed by the sample. Transmitted light is sensed at different

wavelengths and the absorption coefficient is obtained. A schematic of the process is depicted in Figure 19.

The light source is broadband white light. The detector senses all the absorbed light for the material tested at different wavelengths. The light used in the present project is a tungsten halogen broadband source Ocenoptics LS1™ guided by a fiber. Because of the wide range of the band gaps of the sample materials used in this project, the measurements were performed using two different detectors. The detectors used are an extended InGaAs (900 to 2500 nm) and a Si CCD array (400 to 1100 nm). The set up equipment used for these measurements can be seen in Figure 20.

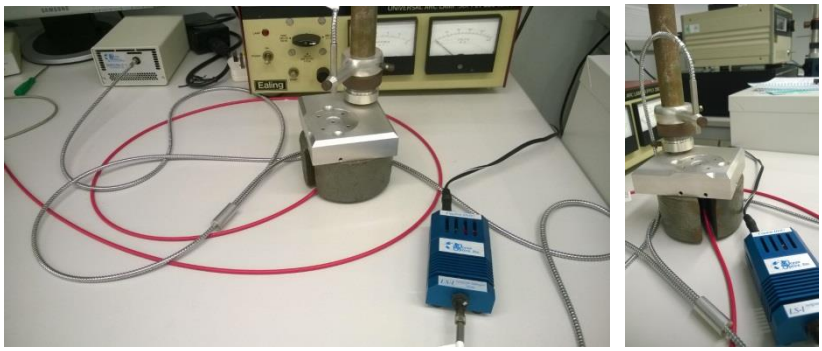

Figure 20 Absorbance equipment setup

Specialized software is needed to obtain the absorbance curves. The software used to collect the measurement data is the SpectraSuite spectroscopy. For the case of the CCD array detector (s2000 Ocean Optics) the software used is 001Base32. To perform the measurement it is necessary to follow first a calibration procedure so reliable measurements can be obtained. The first step is to store the background noise measurement (dark conditions). Next, the reference measurement of the source light is obtained (light condition). Then, the dark condition curve is subtracted from the light reference one and then absorption measurement can be performed.

3.4.3 DCXRD Double Crystal X-ray Diffraction

This non-destructive material characterisation shows the specific constitution of the various films in the epitaxial wafer, since the nominal parameters can sometimes be different from the actual parameters of grown materials. The latter is produced due to variations in both growth rates and compositions. The operational principle of the X-ray

diffraction is based in the inter atoms lattice distance (lattice constant) that is comparable with the incident X-Ray wavelength and which allows the diffraction of the rays (Figure 21). The difference of phase between the rays reflected in the different planes of the crystal structure is then measured. The phase difference can make the addition of both signals larger or smaller than the original ray depending on the magnitude of this difference. This then leads to either constructive or destructive interference effects.

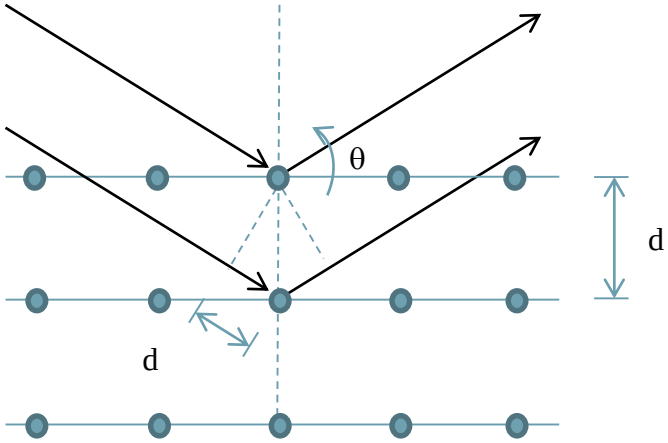

Figure 21 X-Ray diffraction principle [77].

The atoms distribution in the lattice defines the intensities of the rays. The rays intensity can be obtaining using Bragg's law [77] :

$$n\lambda = 2d \sin \theta_B$$

Where:

λ: X-Rays wavelength
n: diffraction order
d: adjacent parallel planes spacing
θ_B: Bragg angle

This condition can be satisfied for more than one angle of incidence ray across the sample which will result in non-constructive interference deviations of the final measurement curve (rocking curve). Thus, for high quality crystals, which have very narrow peaks, the resulting rocking curve cannot be accurate. To ensure the detection in smaller distances (few arc seconds), the x-ray should be conditioned to a second ray. The latter requires the

addition of a reference crystal located between the X-ray source and the sample planes, where the reference crystal should have a lattice constant similar to the material under measurement. Thus, dividing the X-Rays angle into two different pathways, the resulting rocking curve is not influenced by the ray diffractions and it will contain only information about the sample under analysis. This is how most reliable data are ensured by using Double Crystal X-ray Diffraction measurements.

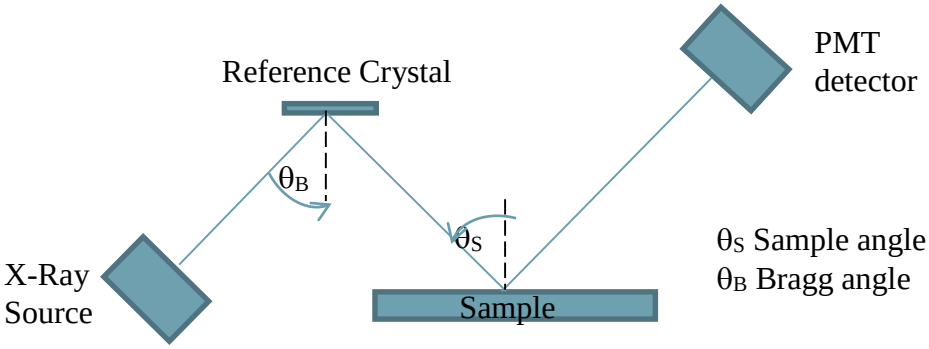

Figure 22 DCXRD apparatus indicating the X-Ray source, the reference crystal, the sample holder and the detector

Figure 22 shows a schematic of the DCXRD process. The equipment used to perform the material characterization in this work is a Bede QC200™ Double Crystal X–Ray Diffraction (DCXRD) which is shown in Figure 23. The X-ray source used has a wavelength of 1.54 Å with random polarization. The crystal references used are:

- Ge crystal: used for wafers grown on GaAs substrates
- InP crystal: used for wafers grown on InP substrates

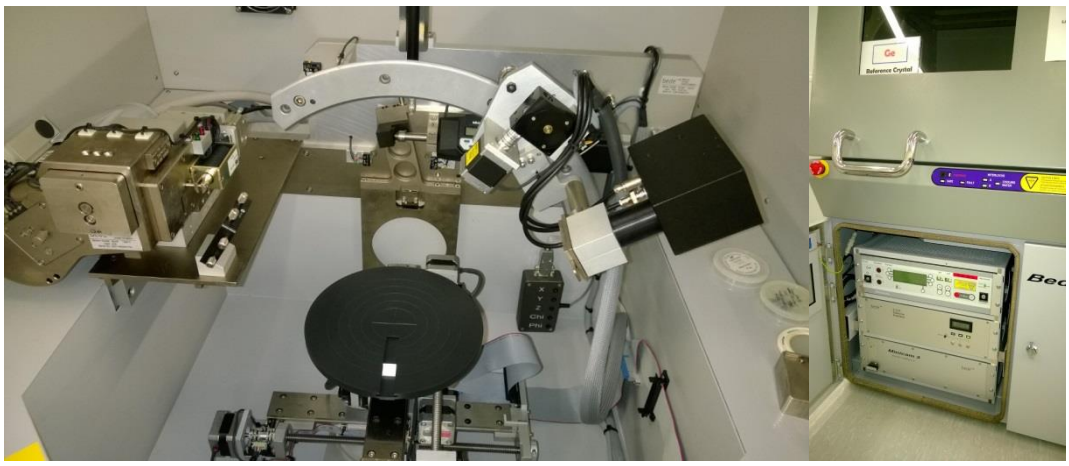

Figure 23 Bede QC200™ DCXRD measurement equipment.

The sample is placed on the equipment base which can be moved with very high precision across axes (x,y and z) and rotated (over planes xy and xz) to locate the sample under measurement as aligned with the reference crystal as possible to obtain a strong peak diffracted. Once the sample is aligned with the reference crystal, a rocking curve can be obtained.

From the X-ray measurements data about the quality of the sample can be obtained and this is represented as narrow peaks. Broadened peaks result from poor quality films.

Once the DCXRD rocking curve is obtained, the data is analysed using the software RADS Mercury™ to find the best fits to thickness and compositions. During simulation, the software starts with some boundary conditions which are usually the nominal values of the grown layers (first approximation) and it iterates until a best fit is obtained between simulation and experimental data. The structural characterisation was done in the University of Manchester facilities.

3.4.4 I-V Characteristics

Once the device is fabricated, it is necessary to test it to extract its electrical and optical parameters. The IV characteristics describe the electrical behaviour of the solar cell. It provides critical information about the device under both conditions of dark and light environments. Sometimes this curve is used to estimate the solar cell behaviour in different environments using different methods of interpolation and extrapolation. [78]

In principle, this is a non-destructive measurement; however, performing the measurement procedure without proper care (e.g. the bias voltage exceeding the limits of the material) the device can be destroyed.

The equipment used to make the IV measurement is the Agilent Technologies B1500A and probe station (Figure 24). This equipment was used only to get the dark conditions (no light) and to test the device's IV characteristics.

Figure 24 B1500A semiconductor device analyser and probe station.

To obtain the IV curve under light conditions, it is necessary to have a solar simulator, which is expensive equipment. However, a solar simulator system was designed and built to perform the measurements for the present project. The solar simulator consists of a broadband incandescent light mounted on a poste in which the height can be adjusted. Thus, the light falling on the device can be calibrated to get 100 mW/cm^2 which is equal to 1 sun standard light. The solar simulator set up is shown in Figure 25.

Figure 25 Solar simulator at 1 sun (100 mW/cm^2)

In order to calibrate the system at 1 sun and to check the reliability of the solar simulator, measurements were performed at the University of Lancaster Facilities. The samples used to perform the system calibration were XMBE291, XMBE293 and XMBE294. They are all high efficiency devices. As can be seen in Figure 26, an excellent agreement exists between the measurements made using a commercial solar simulator and the ones performed with the homemade system.

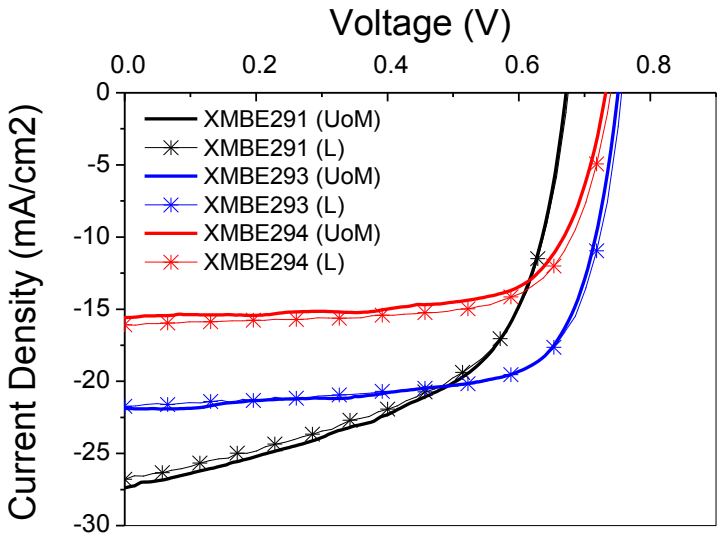

Figure 26 Reliability test and calibration for the solar simulator at 1 sun.

3.5 Fabrication process

The basic fabrication process of the diodes involves: wafer preparation for spin coating, exposure for printing features on the mask, post bake, developing and metallic contacts deposition, and finally cleaning and sintering [79].

Appendix B contains detailed descriptions of the final fabrication steps for the solar cell devices used in the present work.

The fabrication process used for the present work follows the steps below:

1. Sample preparation (cleaning)
2. Post-growth annealing (If necessary)
3. Geometry delimitation
   3.1. Photoresist deposition
   3.2. Exposure
   3.3. Development
   3.4. Wet etching
   3.5. Sample cleaning
4. Back contact deposition
   4.1. Metal evaporation
   4.2. Sintering
5. Front contact deposition
   5.1. Photoresist deposition
   5.2. Development
   5.3. Metal evaporation
   5.4. Lift-off process
   5.5. Sintering
6. Sample cleaning
7. Sample placement on header (TO46)
8. Device wiring

3.5.1 Cleaning

‘Contamination’, understood as any undesired particle on the device, can be generated by different sources such as humans, processing equipment and/or chemical residues. The

transport medium of these contaminants is air or physical contact. In the fabrication process of semiconductor devices, the environment must be controlled as any external impurity could affect the performance and efficiency of the final device. Thus, it is important that the fabrication is conducted in a Cleanroom, which has air extraction systems in order to control the number of impurities in the air.

Before any step is undertaken, the sample needs to be cleaned of contaminants. These contaminants need to be cleaned before the start of the fabrication process. The process applied to the samples in the clean room is:

1. NMP (N-Methyl Pyrrolidone) application to eliminate possible organic contaminants. The sample is cleaned in an ultrasonic bath for 10 minutes.
2. Remove NMP excess with DI water.
3. Then, acetone is applied for 10 minutes (in the ultrasonic bath). During this step the NMP is completely removed from the sample.
4. IPA (Isopropanol) is applied after the acetone for another 10 minutes in the ultrasonic bath. The sample is then dried to remove remains of IPA on the sample surface due to the rapid evaporation of the IPA.

The device is inspected many times during the fabrication process by using a high magnification optical microscope. The visual inspections are made in order to ensure that no impurities are present or to detect any errors in the fabrication procedure.

3.5.2 Post growth annealing

The materials sometimes need to be annealed before the fabrication process. This can change the properties of the material depending of the structure and the material type used. The annealing can be done during the growth process but sometimes the material, due to its characteristics and properties, cannot be annealed during the growth process and needs to be annealed ex-situ.

For example, for InP-based solar cells grown on GaAs substrates the annealing process reduce the quantity of dislocations due to the mismatched lattice. The annealing is performed in an RTA (Rapid Thermal Annealing) equipment, and the effect of reducing

the dislocations density in these cells affects the cells fill factor (FF) and as a consequence improves the solar cell efficiency. [80]

The analysis of the RTA on InAs/GaAs has demonstrated that the result of annealing this type of structures with quantum dots modify greatly the luminescence properties from dot to quantum wells and that the inter-diffusion of the dots layers is increased. This causes narrowing of the luminescence peak and a wavelength shift. [81]

For the case of the studied samples in the present work, the RTA process does not change the properties of the photoluminescence, so this step was discarded for most of the studied samples.

3.5.3 Exposure

Fabrication of semiconductor material system devices requires transfer of patterns on the surfaces of the device to fabricate the devices. For solar cells, this procedure is used in order to create the mesa and to create the pattern for the contact metal grids. There are several methods to transfer patterns. One is electron beam lithography (EBL), it is an expensive method but it has the capability to print very high definition patterns in the nm range. The EBL is a non-mask system; it means that the design is assisted by software and a "pencil" of electrons traces the pattern. [82]

Another method, which is widely used, is photolithography. This method requires a photo-mask in order to shine light and print the patterns. This method uses a UV light in the range of 200 to ~450 nm. In order to print the pattern it is necessary to have a film on the top which is sensitive to this wavelength light, this is the photoresist. There are different types of photoresist the most common of which are:

- Positive (Figure 27a): It is a duplicate of the mask; it means that only the non-exposed resist is kept after developer application.
- Negative (Figure 27b): Here, One negative image of the mask is obtained. It means that the resist on the illuminated zones is kept after developer application.

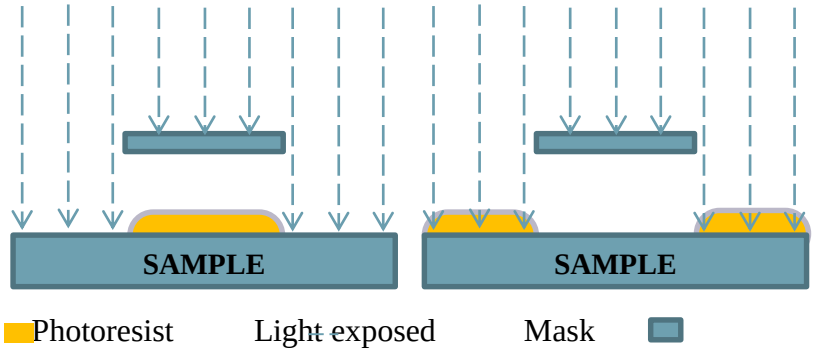

Figure 27 Photoresist types a) positive and b) negative after developing

The photoresist coating is spun on the sample surface. The spinner is rotated, depending of the photoresist to be used, from 300 to 600 rpm for approximately 45 seconds in order to have a uniform distribution of the coating on the wafer surface. The thickness of the coating depends on the substance applied and it is a function of the rpm's and the spin time. In the University of Manchester facilities the resist used for the purposes of solar cell fabrication are specified in Table 7, which lists the photoresist name, type and the developer used to eliminate the residual resist.

After the "spin coating", the next step is the "prebake" or soft bake in order to avoid deformations of the coating due to the photo resist solvents used to develop the pattern. The soft bake is performed at 110 °C using a hot plate.

Table 7 Photo resist and developers used for solar cell project

Photoresist	Type	Developer
S1805	Positive	MIF319
AZnLOF 2070	Negative	MIF326

After the soft bake, follows the alignment. This consists of exposing the wafer to print the pattern (mask) on the photoresist. The equipment used for this is a Karl Suss MA4™mask aligner. For solar cells fabrication it is necessary to make two alignments:

- Mesa definition
- Front contact pattern (current collector)

One of the masks designed for this work is shown in Figure 28, and the dimensions details are presented in Appendix A Mask Designs. The developing is performed with different solvents depending on the exact needs of the device.

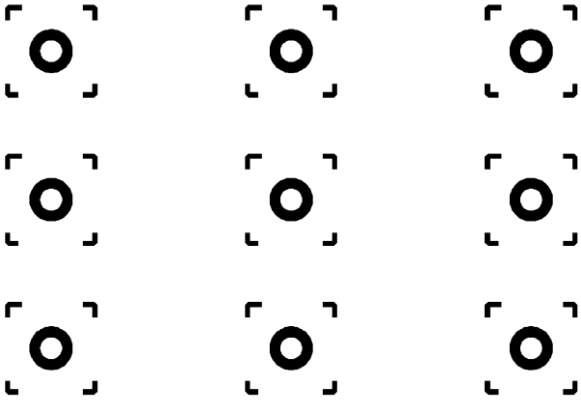

Figure 28 Solar cell Mask (7.5mm x 7.5mm)

However, after a long optimization process and after trying several geometries, the best geometry found was a cylindrical diode of 250 µm diameter. A non-alloyed Au/Ti ring is used for the front contact and an alloyed Au/AuGe ohmic for the back contact with shading losses of 48%. The geometry for the fabricated devices reported in this work is shown in Figure 29.

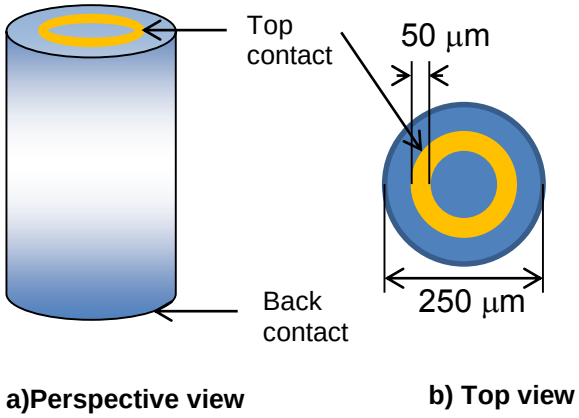

Figure 29 QD PV devices' geometry

Nowadays efforts are dedicated to finding new methods to generate the patterns with good definition but at lower costs. One way is using flexible stamps in order to print texturized patterns on the solar cells surfaces; this is convenient for reducing costs of texturizing the

solar cell surfaces for antireflective purposes. The name of this technique is Nano Imprinted Lithography with UV light (UV-NIL). [83]

3.5.4 Resist Developing

After the exposure, there is a need to use again the hot plate, for "post baking" in order to stabilize the photo resist. This post bake is performed at 120 ºC for only one minute. The developer is a substance that will eliminate the undesired photoresist in the wafer surface. Different developers are available and each one of these reacts to different photoresist depending on the purpose of the process, additive (Deposit materials) or etch (eliminate material). For the photoresists used for this project see Table 7. The mesa is the active area delimitation; this step is made in order to reduce the leakage current due to the dark current from the area where the metal fingers are not present. Different geometries were tested in order to find the optimum dimensions to minimize the leakage. Cubic and cylindrical mesas were tested (Appendix A Mask Designs). The cylindrical mesa exhibited the best results.

3.5.5 Metal deposition

This step consists of depositing a conductive material (metal) on the surface to define the contacts for the device. The metallization process can degrade the device behaviour if not carefully performed. The main degradation are losses due to the series resistance of the contacts deposition.

The contacts for the solar cell need to be made of a conductive material but not necessary pure metal. In the case of silicon solar cells, a nickel and copper combination can be used with successful result [84]. Organic material can also be used as contacts which are conductive but these can introduce large losses as well. The solar cell presented in this work has metallic contacts which use the following composition:

- Front contact (fingers): Titanium - Ti (50nm) / Gold - Au(100nm)
- Back contact: Gold-Germanium - AuGe (50nm) / Gold - Au(100nm)

The process is performed using a BioRad Evaporator; the sample is located in a high vacuum chamber and the metals are located on their respective boats. When the required vacuum is established into the chamber the process begins. It is necessary to perform the evaporation under low-pressure chamber conditions in order to reduce the presence of contaminants, thus, the evaporation is performed using a pressure $< 10^{-6}$ mbar. The filament of each boat is electrically excited, first the Titanium and Gold-Germanium and at the end the Gold boats. The boat's filament current is increased until the metal starts to evaporate. The temperature required to evaporate the metal is obtained from the current passing through the filament. There is another type of evaporation: electron beam but this method is more expensive. The evaporator used to evaporate the devices contacts for the present project is a BioRad. The setup and the equipment are shown in Figure 30.

Figure 30 BioRad and process setup diagram

3.5.6 Lift-off

Once the metallic contacts are evaporated uniformly on the material surface, it is necessary to remove the undesired metal. The way to do the latter is to dissolve the photoresist previously spin-on. On the top of the device, the deposited photoresist do not cover the area where the metal is desired. So, when the metal is deposited, the metallic layer will cover both areas with and without photoresist. If the material is exposed (submerged) is the correct solvent, the photoresist will be eliminated taking with that the undesired metal.

Thus, the lift-off process is a non-destructive procedure. However, it is important to run the lift-off carefully because a mistaken handling could damage the desired metallic contacts.

For the actual project purposes, N-Methyl-2-pyrrolidone 1165, usually called NMP, was used at room temperature, as long as necessary (approximately 15 minutes), to remove the photoresist remaining and, as a consequence, the undesired metal on the surface.

3.5.7 Sintering and annealing

These are critical steps for both front and back contacts. For the back contact, annealing forms the ohmic contacts so the device can be biased without perturbing its device behaviour. So, in order to form the ohmic contact Au-Ge is used (in an 87%-13% combination) as dopants to form alloys.

Figure 31 Alloying and Sintering equipment

Annealing will increase the temperature up to the melting point of Au-Ge to make it diffuse into the wafer back surface and reduce the resistance of the contact.

The Top contact is a non-alloyed contact and us used sintered at a lower temperature. The ideal temperatures found are 320 C for 2 minute for AuGe/Au alloyed contacts and 240 C for 1 minute for the front Ti/Au sintered contacts.

CHAPTER 4

QUANTUM WELL DEVICES: RESULTS and DISCUSSIONS

4.1 Introduction

The use of multiple quantum wells structure (MQWs) has many advantages due to the confinement of the electrons in two dimensions. QW give rise to new energy levels as it is described for the following equations. The different transitions between these states created in the quantum well(both in the conduction and valence bands) could be heavy hole level 1- electron level 1 (Figure 16a), light hole level 1 – electron level 1 (Figure 16b) or heavy hole level 2 – electron level 2 (Figure 16c). As shown one transition can be calculated as:

$$\boldsymbol{E_n = E_g + \Delta E_{n,c} + \Delta E_{n,v}} \quad \mathbf{1}$$

Where En is the 'n' subband energy, $\Delta E_{n,c}$ and $\Delta E_{n,v}$ are the quantised levels and E_g the energy bandgap of the well material. From the particle in a box problem one can calculate $\Delta E_{n,c}$ and $\Delta E_{n,v}$, as,

$$\boldsymbol{\Delta E_{n,c} = \frac{\left(h/2\pi\right)^2 \pi}{2m_e^* L} n^2} \qquad \mathbf{2}$$

$$\boldsymbol{\Delta E_{n,v} = \frac{\left(h/2\pi\right)^2 \pi}{2m_h^* L} n^2} \qquad \mathbf{3}$$

Thus, adding equations 2 and 3 we have:

$$\boldsymbol{E = E_g + \frac{\left(h/2\pi\right)^2 \pi}{2m_e^* L} n^2 + \frac{\left(h/2\pi\right)^2 \pi}{2m_h^* L} n^2} \qquad \mathbf{4}$$

Where:

m_e^*, m_h^* - Effective masses of electron and hole

L – Well thickness

n – Number of energy state

So the possible energy levels in the quantum well depend directly on the well thickness. Different subbands can exist not only in the well but also in the barrier, thus different confined energy gaps are present in the structure and this increases the absorption range of the material. So, the number of quantum wells will increase the absorption in the device [85]. These new states can be confirmed in measurements of optical activity in the device

such as absorption or photoluminescence measurements [86]. The use of multiple quantum wells was proposed in order to avoid the problems present in tandem solar cells at the moment of joining the different cells one on the top of the other because of the difficulty of putting contacts. In [86], Barnham reported a structure in which the first active layer of MQWs was built of (InGa)As/GaAs and it was found that by controlling the barrier and the well thickness it is possible to modify the absorption bandgap due to the confined levels in the QWs. It is also possible to use superlattice configuration but the disadvantages are the high number of wells required to increase the material absorption. So it is better to use constant thickness for the wells when making the MQW structure [87].

4.2 Structural characterisation

The QW studied samples are VMBE1661, VMBE2016, VMBE2017, XMBE242 and XMBE245. The layers details for all these samples are shown in Figure 32.

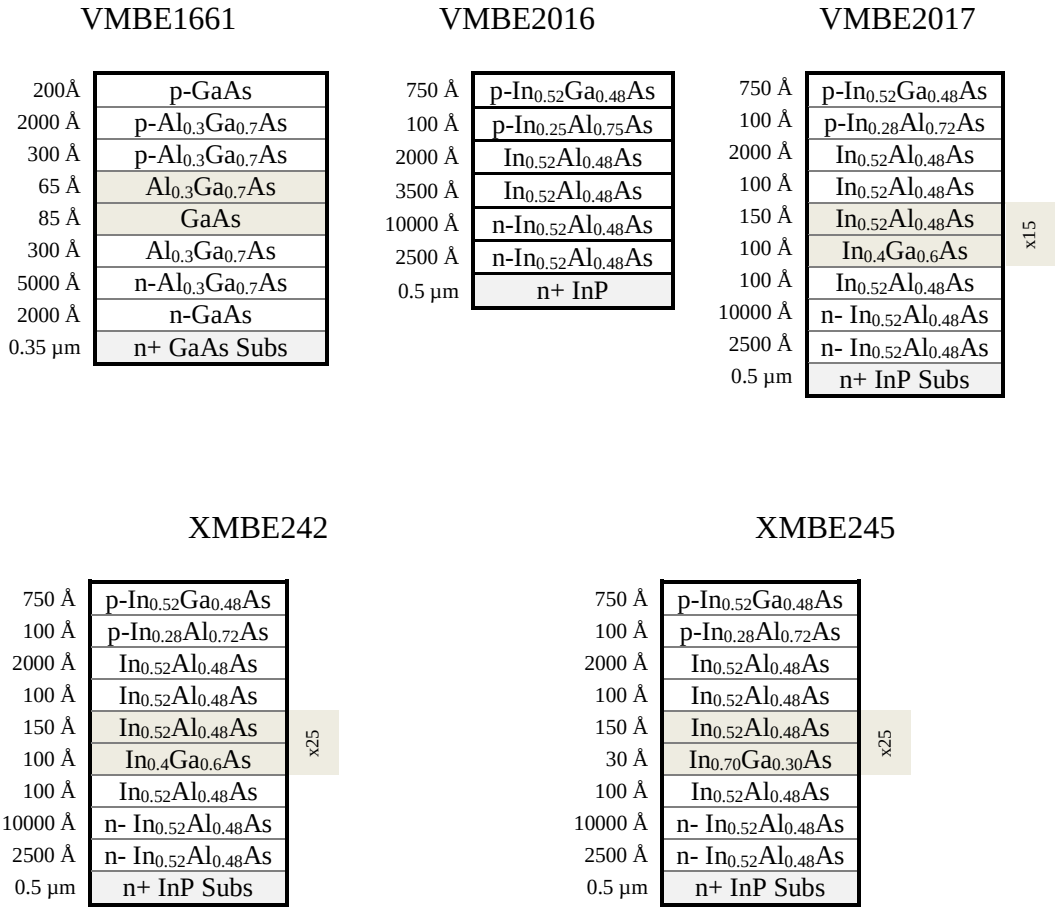

Figure 32 Quantum Well structure epitaxial details

For the GaAs system based material, VMBE1661, the DCXRD measurement is shown in Figure 33. The measurement shows that the highest peak corresponds to the substrate material (GaAs) and the peaks around it are the satellite peaks due to the MQW structure. The RADS simulation fitting extracts the real values of the thickness and composition of all the layers. The experimental and simulation show that the sample is of good crystalline quality. The peaks are also very narrow.

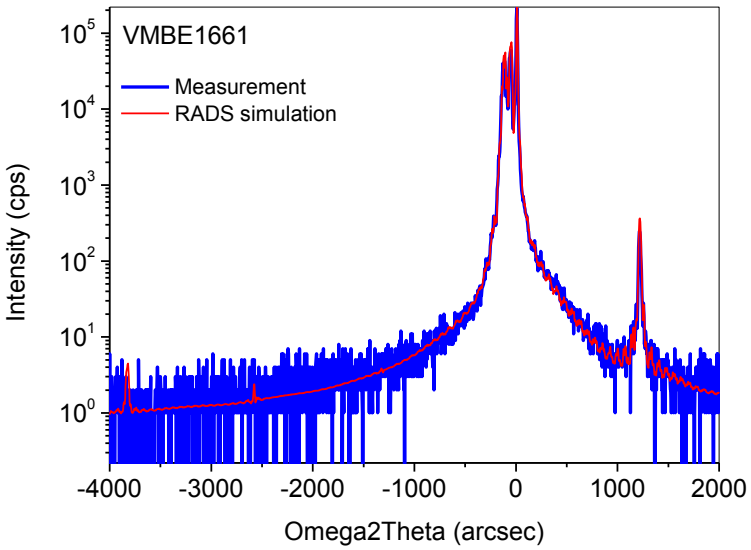

Figure 33 DCXRD for sample VMBE1661, GaAs material.

For $In_xGa_{(1-x)}As/In_xAl_{(1-x)}As$ multi-quantum wells materials, the structural characterisation is shown in the following figures. The DCXRD measurement showed in Figure 34 depicts the rocking curves for material VMBE2016. The sample is of good quality and is nearly lattice matched structure. The measurement shows only two strong peaks one which corresponds to the InP substrate and the other to the nearly lattice matched $In_{0.52}Ga_{0.48}As$ and at the sides it has two more peaks at lower intensity corresponding to the emitter and cap layers. The simulation results for this sample are in a good agreement with the designed values.

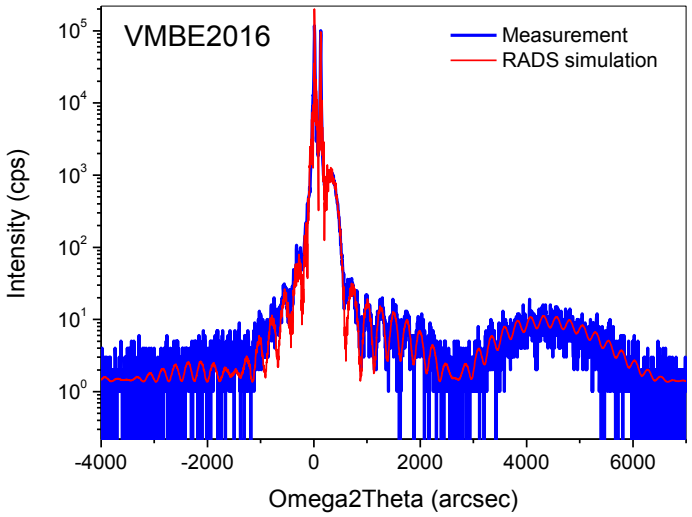

Figure 34 DCXRD for VMBE2016 InGaAs/InAlAs system based materials. Control sample

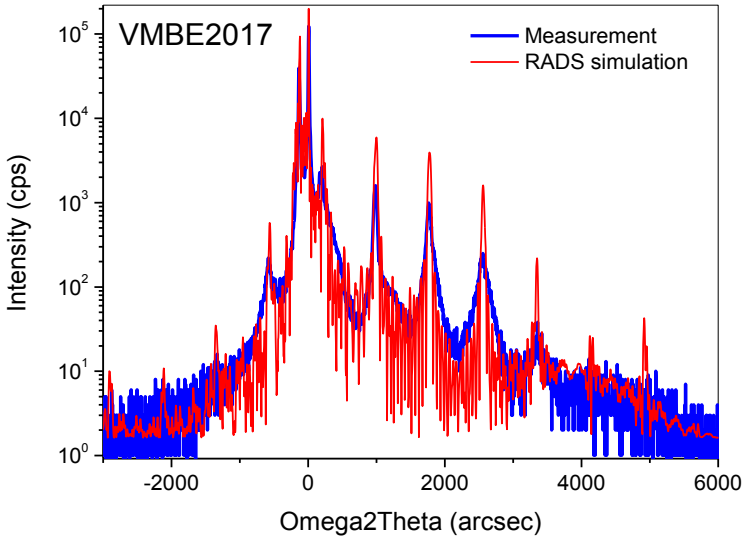

Figure 35 DCXRD for VMBE2017, x15 MQW InGaAs/InAlAs tensile strained system based material

Introducing a Multiple Quantum Well (MQW) structure within the host lattice will generate more peaks around the substrate peak in the rocking curve. This is the case for the 15 quantum wells periodicity sample, VMBE2017, shown in Figure 35. These peaks (Satellite peaks) and their number will increase when increasing the number of wells as well.

Sample XMBE242 has 25 QWs and is lattice matched. This time, the DCXRD does not show satellite peaks due to the lattice matched configuration. Figure 36 shows the effect of the 25 lattice matched QWs without satellite peaks but with different peaks around the highest peak which corresponds to the InP substrate. It is important to notice that the peaks are well defined and very narrow meaning that the quality of the sample is very good.

The XMBE245 material has 25 strained QWs, so similar to XMBE242 but in this case the QW is highly compressively strained. It means that the lattice constant of the barrier is higher than the lattice constant of the well. The DCXRD shows more peaks, corresponding to the satellite quantum well peaks. Figure 37 shows the effect of the 25 QWs in the different peaks around the highest peak that corresponds to the InP substrate. The number of satellite peaks is increased because of the reduction of the QW thickness. The satellite peaks are well defined but are very broad, perhaps due to dislocation or high strain.

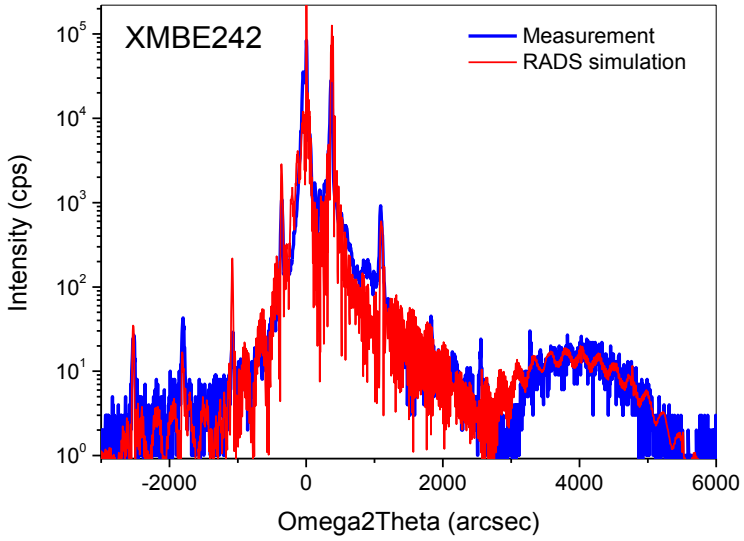

Figure 36 DCXRD for XMBE242, x25 MQW InGaAs/InAlAs lattice matched system based material

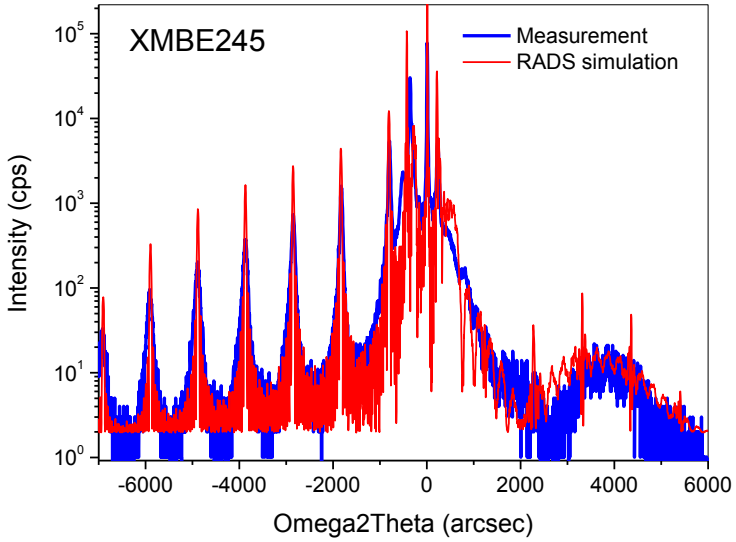

Figure 37 DCXRD for XMBE245, x25 MQW InGaAs/InAlAs compressively strained system based material

As it can be seen from the previous DCXRD rocking curves, regarding of the crystal quality, showed a good crystal lattices for VMBE1661, VMBE2016, VMBE2017, XMBE242 and XMBE245. Specifically, when we talk about mismatch materials such as samples VMBE2017 and XMBE245, the materials were grown with an excellent quality despite the evident risk of having undesired defects. The effect of the lattice mismatch has been depicted in several satellite peaks surrounding the strongest rocking curve peak (corresponding to the substrate peak). An excellent agreement between the nominal values and the actual crystal values was demonstrated by performing the RADS simulation.

4.3 Optical characterisation

As has been mentioned in previous sections, the optical characterisation is crucial for a good understanding of photovoltaic devices as optical measurements will reveal information about material absorption range and the different energy levels present in the material.

The photoluminescence measurement for sample VMBE1661, which was grown at 670 °C, shows emission from the quantum wells (GaAs wells) including both ground and first

excited state at room temperature. The absorbance measurement was performed but it was impossible to get good result. Figure 38 shows two measurements of absorbance. In the first one the InGaAs detector (from 900 nm to 1800 nm) is used showing that GaAs-$Al_{0.30}Ga_{0.70}As$ solar cell is not absorbing any energy in this wavelength range. The second measurement was made using the CCD detector (from 500 nm to 1100 nm) showing that around 900 nm the material start to absorb strongly. However, below 880 nm the absorbance measurement cannot be performed correctly because the GaAs substrate starts to absorb all the light. The solution is to "lift-off" the substrate in order to measure the absorption in the active layers. Because of the band gaps involved in the GaAs-$Al_{0.30}Ga_{0.70}As$ system the absorbance start from 600 nm to 870 nm approximately. In Figure 39 a scan from 600 to 700 nm shows a very low intensity peak centred at 662.4 nm (1.87 eV) that correspond to $Al_xGa_{(1-x)}As$ material layers with composition x=0.35.

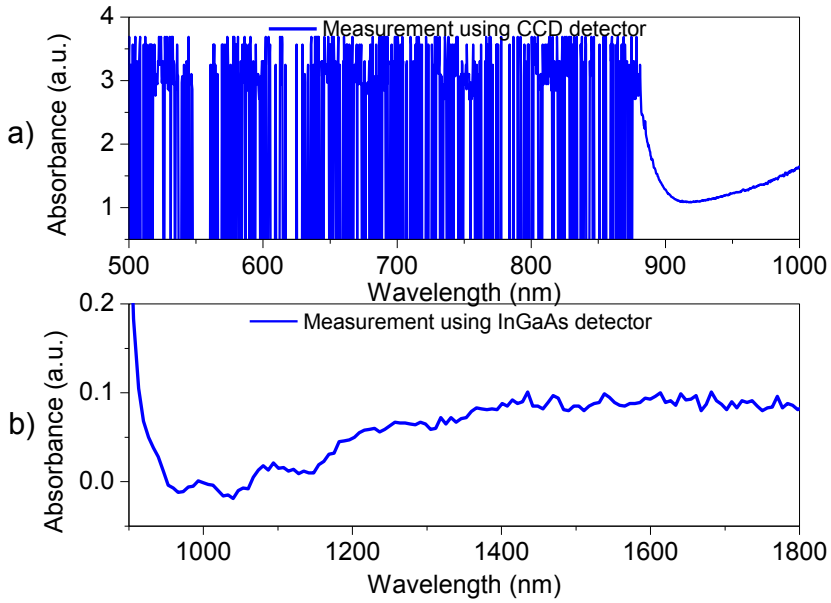

Figure 38 Room temperature absorbance measurements for VMBE1661.

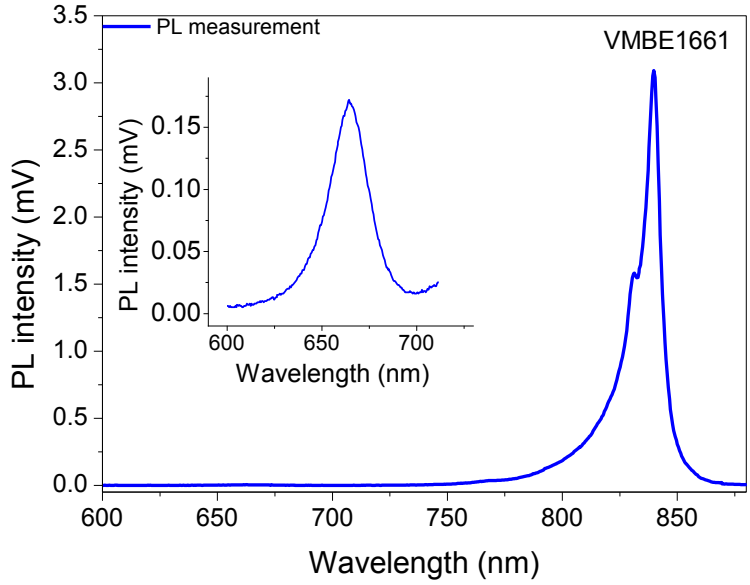

Figure 39 Room temperature photoluminescence measurements for VMBE1661.

Figure 32 shows the epitaxial details for the following sample measurements. The absorption measurement for sample VMBE2016, grown at 580 °C, is shown in Figure 40 where the absorption of energy starts in 1.65 µm (~0.750 eV) which corresponds to the contact layer of $In_{0.51}Ga_{0.49}As$. The VMBE2016 material was designed to be a control p-i-n diode. Its photoluminescence measurement reveals two peaks that correspond to the $In_{0.52}Al_{0.48}As$ and $In_{0.51}Ga_{0.49}As$ materials. The photoluminescence measurement is shown in Figure 41.

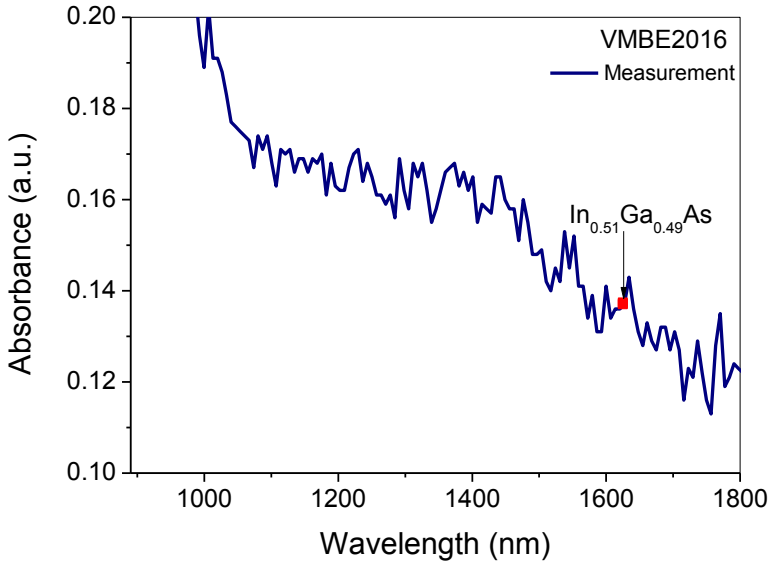

Figure 40 Room temperature absorbance measurements for VMBE2016 showing the $In_{0.51}Ga_{0.49}As$ optical transition at 0.7eV.

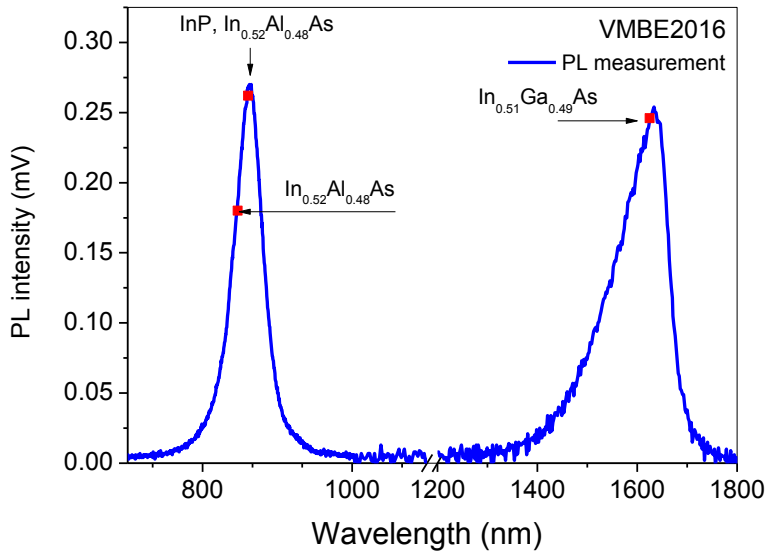

Figure 41 Room temperature photoluminescence measurements for VMBE2016 using CCD detector (700 – 1100 nm) and InGaAs detector (1200 – 1800 nm).

The effect of the QW is visible in the VMBE2017 sample absorbance characterization depicted in Figure 42, showing very nice defined steps near 1.1, 1.4 and 1.5 µm. So it is clear how the QWs increase the absorption of the material due to the electron confined in smaller energies between the barriers. Just like in the case of VMBE2016, there are two peaks present; of course each one corresponds to the two materials used but now near the $In_{0.52}Ga_{0.48}As$ peak appears a shoulder. The latter can be seen in Figure 43. According to the calculation using equation 4 described at the beginning of the present Chapter, this new peaks corresponds to the QWs sublevels generated in the $In_{0.42}Ga_{0.58}As$ well. These levels enhance the absorption of the cell.

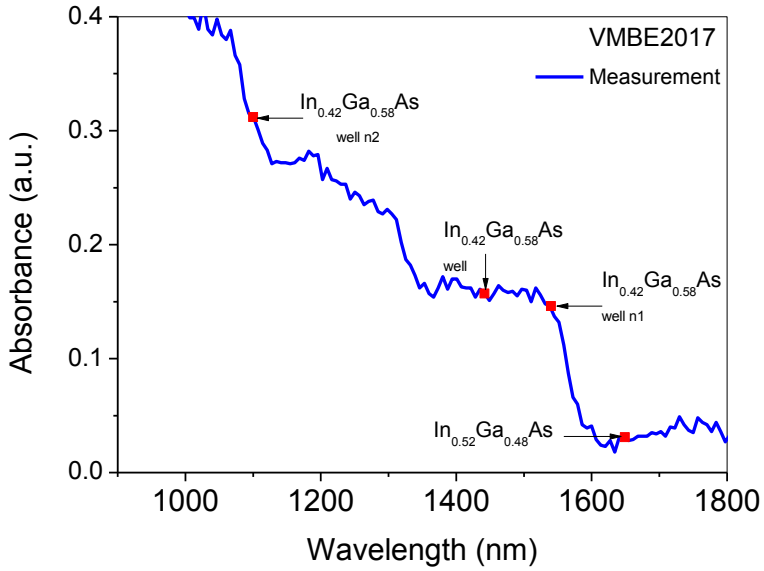

Figure 42 Room temperature absorbance measurements for VMBE2017 showing three different optical transitions.

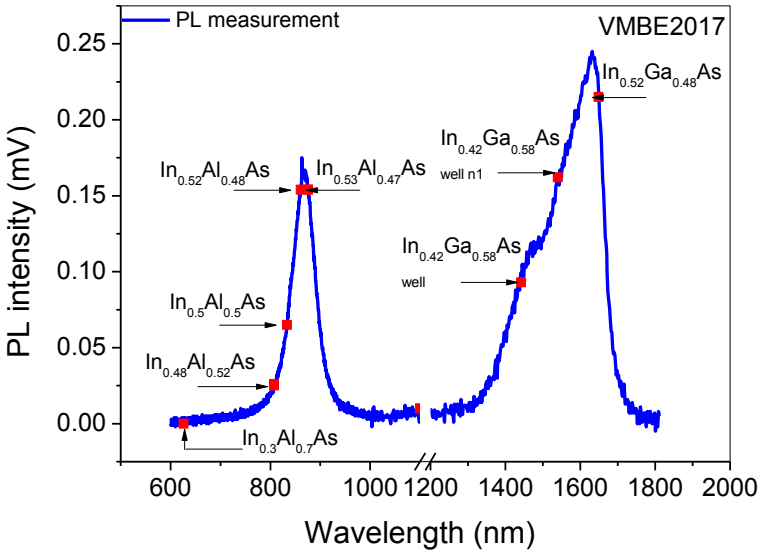

Figure 43 Room temperature photoluminescence measurements for VMBE2017 using CCD detector (700 – 1100 nm) and InGaAs detector (1200 – 1800 nm).

Sample XMBE242 exhibited a similar behaviour to the previous samples. In the case of absorbance measurements the sub-bands of the QWs generates steps in the graph. In Figure 44 these steps are shown around 1.06, 1.3 and 1.5 µm. Now, compared with the vmbe2017 sample the absorbance is much better, and it proves that the addition of more quantum wells increases the absorption but also the crystal structure was of a much better quality. The absorption extends from 1 µm to 1.6 µm approximately. Below 1µm, there are difficulties measuring the absorption as the InP substrate starts absorbing very

strongly. Now the shape of the $In_{0.52}Ga_{0.48}As$ peak in the PL measurement (Figure 45) is very different; the PL intensity is much higher and the QW absorption is at 1549 nm.

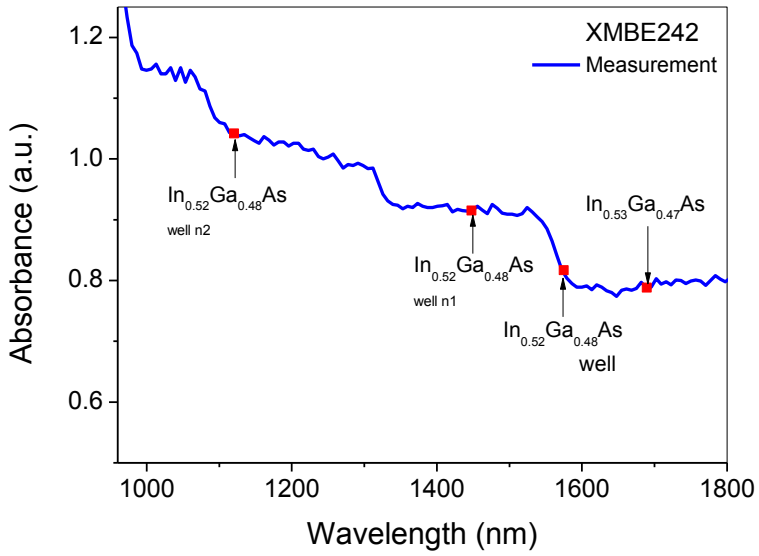

Figure 44 Room temperature absorbance measurements for XMBE242 showing four different optical transitions.

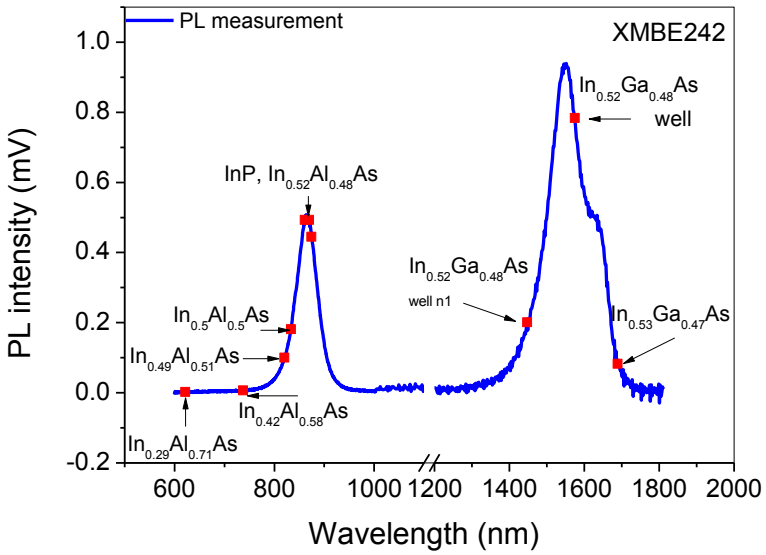

Figure 45 Room temperature photoluminescence measurements for XMBE242 using CCD detector (700 – 1100 nm) and InGaAs detector (1200 – 1800 nm).

The absorbance measurement for sample XMBE245 is shown in Figure 46. For this sample, the sub-bands of the QWs generate several steps in the graph. These steps are shown only around 1.3 and 1.5 µm. Now, compared with the XMBE242 sample the absorbance is poor, which suggests that the addition of strained quantum wells reduces

the absorption. This is evident from the much better steps shape in XMBE242. The absorption is from 1.3 µm to 1.6 µm approximately. The mismatched lattice modifies the shape of the $In_{0.52}Ga_{0.48}As$ peak in the PL measurement (Figure 47); the shoulder pass from the left side to the right side compared with the XMBE242 sample.

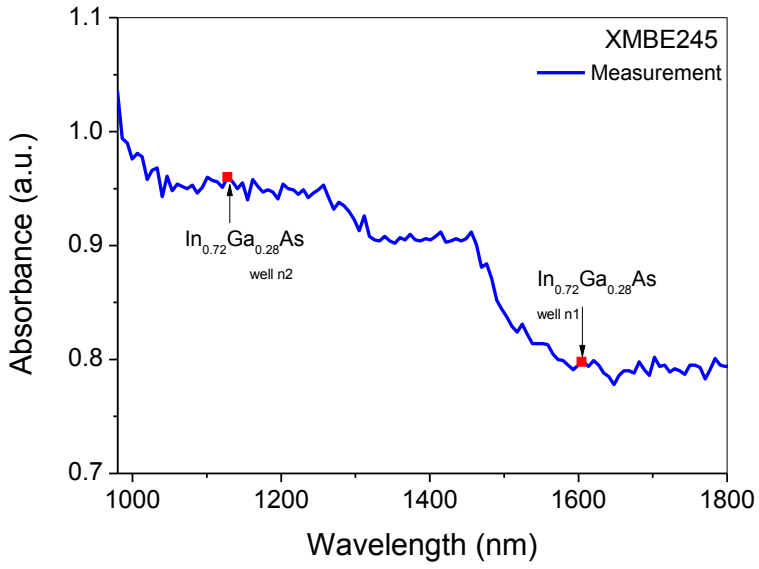

Figure 46 Room temperature absorbance measurements for XMBE245 showing the several InGaAs optical transition due to the multi-quantum wells structure.

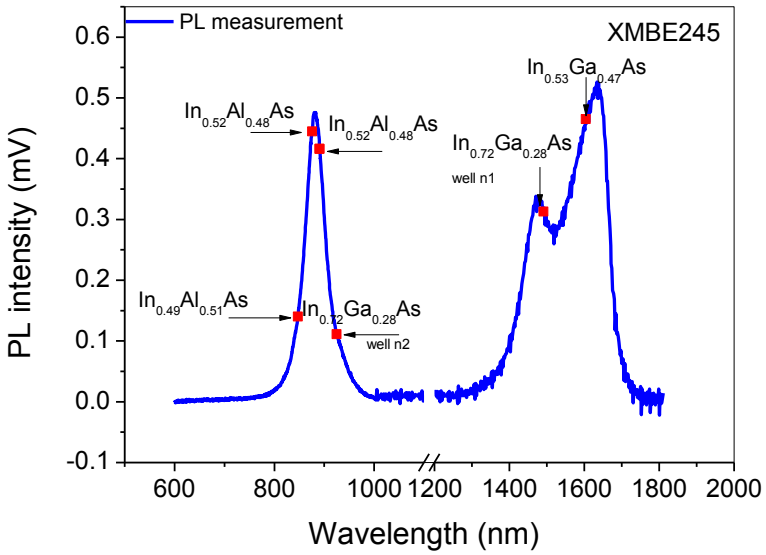

Figure 47 Room temperature photoluminescence measurements for XMBE245 using CCD detector (700 – 1100 nm) and InGaAs detector (1200 – 1800 nm).

According whit the PL and absorption measurements for several MQW materials it was observed that the insertion of the strain in the InGaAs/InAlAs quantum well material system resulted in the reduction of the absorption of the cell, probably as result of defect

introduction. However, the open circuit voltage was increased, which is something desirable as implied that the power operation point is increased. The effect of the QW is visible in the VMBE2017, XMBE242 and XMBE245 with very nice defined steps near 1.1, 1.4 and 1.5 μm, which increases the absorption of the material. The corresponding calculations demonstrated that this new peaks corresponds to the QWs sublevels generated in the $In_{0.42}Ga_{0.58}As$ well. The absorption for using InGaAs/InAlAs MQW material system can extend the absorption range from 1 μm to 1.6 μm approximately enabling the infra-red material absorption.

4.4 Electrical characterisation

4.4.1 J-V curves

As was mentioned before, the electrical measurements were performed at room temperature under 1sun (light power 100 mW/cm^2). The JV curves (J is current density) for all the samples are shown in Figure 48. VMBE1661 measurement shows that the Jsc in light conditions goes up to 10 mA/cm^2 and the Voc is approximately 0.85 volts. This GaAs based material is the one that exhibited the best performance among all the MQW materials studied.

The second best performance was showed by VMBE2016, the control sample. Its Jsc is 7 mA/cm^2 and the turn on voltage is approximately at 0.4 volts. The Voc is less that the value found for $GaAs/Al_{0.30}Ga_{0.70}As$ material and it impacts directly on the cell efficiency. The JV curve for sample VMBE2017 ($In_{0.52}Al_{0.48}As/In_{0.52}Ga_{0.48}As$ MQW x15) shows that the turn on voltage was reduced to 0.15 volts compared with the one exhibited by VMBE2016 sample largely as result of the very low "effective" band gap due to the QW. The light measurement leads to a short circuit current of 0.52 mA/cm^2.

Originally an increase in the efficiency of the device was expected due to the insertion of the quantum wells. The short circuit current reduced by almost 25% with respect to the control sample (VMBE2016) as the open circuit voltage was drastically reduced by 50%. The massive drop in the open circuit voltage is due to the much reduced effective band gap due the QW which lowers the turn on dramatically. Unfortunately while the low band

gap enhances the long wavelength absorption region enormously, as shown previously, an unintended consequence is the reduction in the open circuit voltage and consequently the device efficiency is severely degraded.

For sample XMBE242, the JV characterization shows a reduction in the short circuit current to only 1.5 mA/cm^2, and the open circuit voltage is approximately 0.27 volts, equal to the Voc of the VMBE2017 as expected from the use of low band gap materials in the QW.

Furthermore, XMBE245 material (x25 compressively strained InGaAs/InAlAs MQWs) exhibited a short circuit current of 2.2 mA/cm^2 which is higher than the XMBE242 values. In addition, the material exhibited an open circuit voltage of 260 mV. As result of the mismatched lattice, it can be seen an efficiency enhancement.

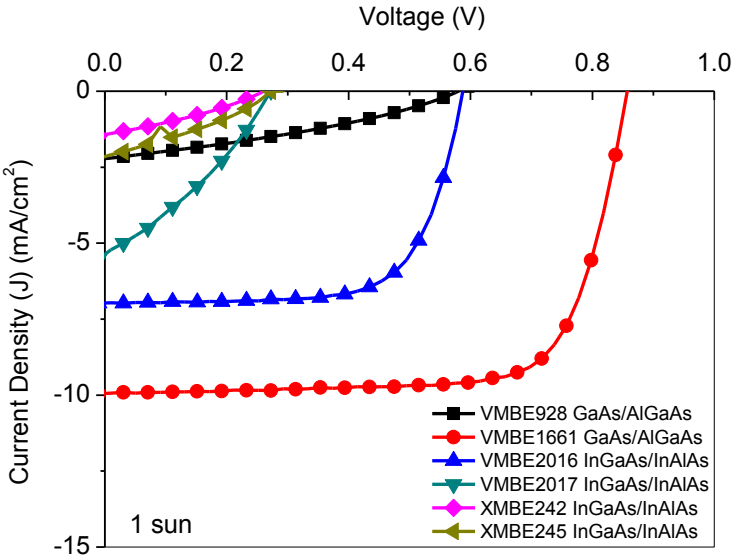

Figure 48 Room temperature JV measurements for all materials using quantum wells structures.

From the measurements of the electrical behaviour of the devices it is possible to estimate the efficiency of the cell. The efficiencies of the devices made from the different wafers are shown in Table 8. The highest efficiency (2.8%) for the InGaAs/InAlAs system based material is obtained for the control p-i-n junction sample. By contrast the GaAs/$Al_{0.30}Ga_{0.70}As$ material VMBE1661 exhibited the highest efficiency of all the studied MQW materials in this section. Note that the growth temperature of the GaAs

QW plays a large role in the efficiency as lowering the growth temperature to 580 °C (sample VMBE928) lowered the efficiency from 6.3 to 0.4% as a results of increased electronic point defects in the material.

Table 8 Photovoltaic material efficiencies for all materials based on quantum well structures.

	Sample	Jsc	Voc	FF	η
		mA/cm^2	V	%	%
GaAs/AlGaAs	VMBE928	-2.24	0.59	32.8	0.4
	VMBE1661	-9.92	0.85	75.2	6.3
InGaAs/InAlAs	VMBE2016 (control)	-6.96	0.59	69.6	2.8
	VMBE2017 Tensile strained	-5.49	0.26	32.8	0.4
	XMBE242 Lattice matched	-1.46	0.26	30.8	0.1
	XMBE245 Compressively strained	-2.18	0.28	30.9	0.1

It can also be observed that the efficiencies of the devices are low. There was an expectation that there would be an increase in the efficiency in the samples VMBE2017, VMBE242 and VMBE245 due to the QWs insertion and indeed the absorption measurements showed greatly enhanced absorption in the long wavelength region. However the effect of the low band gap QW is to effectively lower the open circuit voltage in proportion to the band gap and thus the efficiencies were greatly affected. This was confirmed via physical simulations using SILVACO in Section 4.5.

4.4.2 External Quantum Efficiency

In Figure 49, it can be seen that the external quantum efficiency (EQE) of the cells is degraded when moving from samples VMBE2017 ($In_{0.52}Al_{0.48}As/In_{0.52}Ga_{0.48}As$ MQW x15), to XMBE242 ($In_{0.52}Al_{0.48}As/In_{0.40}Ga_{0.60}As$ MQW x25) and finally XMBE245 ($In_{0.52}Al_{0.48}As/In_{0.70}Ga_{0.30}As$ MQW x25). The GaAs samples (VMBE928 and VMBE1661), as expected, have the best performance in the visible light spectrum (around 400 to 800 nm). On the other hand the efficiency of the InGaAs/InAlAs cells, again as expected, is increased in the infrared spectrum (above 800 nm).

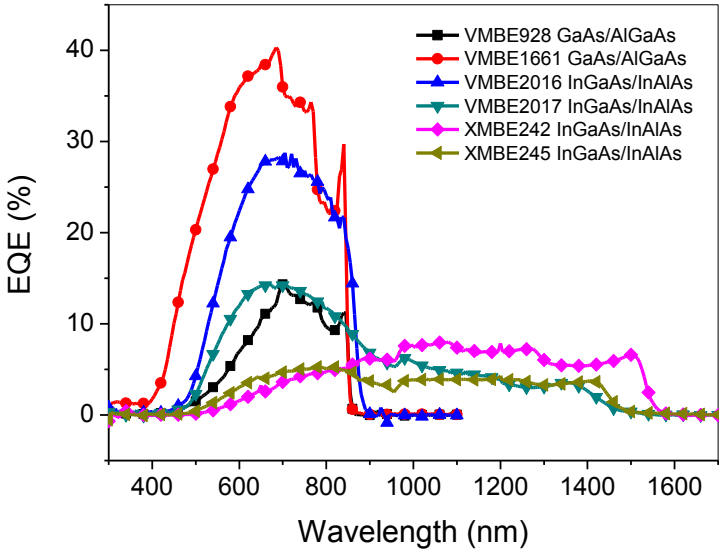

Figure 49 Room temperature External Quantum Efficiency for quantum well materials.

Recalling the JV curves, it is shown that the highest short circuit current is provided by the high temperature grown GaAs/$Al_{0.30}Ga_{0.70}As$ device (VMBE1661), agreeing its highest absorption efficiency in the visible range. This sample also exhibited the highest value of open circuit voltage. The lattice matched InAlAs control sample VMBE2016 shows good values of short circuit current and open circuit voltage as it does not include any low band gap material in its structure. This is not the case for InGaAs/InAlAs MQW structures. The efficiency drops significantly with respect to the control sample due to the insertion of the low band gap MQW materials.

4.5 Optimisation process

Generally the fabrication process follows the simulation process. But for this section the process is opposite. Why is it like that? Because first of all the simulation must be closer to the real values, it means that in order to have dependable simulations, SILVACO needs to be properly calibrated. Therefore the SILVACO material parameters have to be tuned (recall that SILVACO is primarily a software for Silicon devices design) to match both the measurements and the simulation. Once this is achieved, it should be possible to perform *predictive* simulation first and then fabrication afterwards to check the simulation.

4.5.1 SILVACO modelling

SILVACO(c) is software developed by Dr. Ivan Pesic's company and it is a software designed for the physical simulation of electronic devices. It is a convenient tool to simulate devices to predict their performances starting from first principles and includes both epitaxial layer definitions AND device layout, making it a powerful virtual wafer fab tool. The core of SILVACO is Atlas, this module has its own syntax and it is possible to define the structure, the material in which the device is made and its physical parameters. This chapter will present a simple introduction to SILVACO simulation that is common to almost all devices. Of course, each device type has its own specific materials parameters. Modules specific to solar cell simulation include light source simulation. The information of this chapter was taken from "SILVACO ATLAS User Manual" [88], "Device Simulation guide" [89] and from the simulation code developed for this project purposes.

SILVACO has many modules, each one is used independently but in order to make a simulation they need to be integrated. All the code can be developed using DeckBuild which is the run-time environment, from DeckBuild it is possible to load the structure files previously made in Athena (Device designer) or DevEdit (Structure and Mesh Editor). All this parameters are analysed into Atlas the core of SILVACO. Atlas solves all the equations and generates the LOG and STR files which include all the calculated data. This information can be plotted in TonyPlot (tool for visualize the results) and exported to other file types. The design can be on 2D or 3D structures.

In addition, SILVACO has also:

- An Optimizer – Library of Optimizers
- A C-Interpreter – Interactive Model Development
- Mocasim – Monte Carlo simulation tool

The method used in SILVACO is the finite difference, so it is iterative and needs discretisation of the problem. In other words, the device is divided into small pieces and the program tries to find the solution starting with one initial value and then calculating the next value taking into account the previous one.

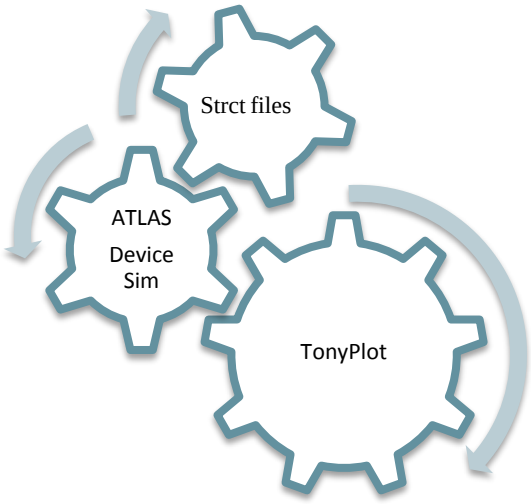

Figure 50 SILVACO simulation engine

In Figure 50 is shown the complete engine of SILVACO. It has many modules but for the specific interest of this project only ATLAS, DeckBuild and TonyPlot are the most relevant.

ATLAS can be called the "SILVACO core" because it is responsible for doing all the calculations required to get a result. It includes the different models and the algorithms to get the solutions. DeckBuild can be seen as the "administrator" because it is responsible for passing all the required parameters to ATLAS and other modules to do the corresponded process. Finally, TonyPlot is the user graphic interface helping to visualize and export the final data of the process.

All simulations mostly follow the same process independently of the device geometry or functionality. The process is the same in all the cases. Basically the process of simulation in SILVACO has the steps shown in Figure 51. Each step will be described in this section with the possible options available in the software.

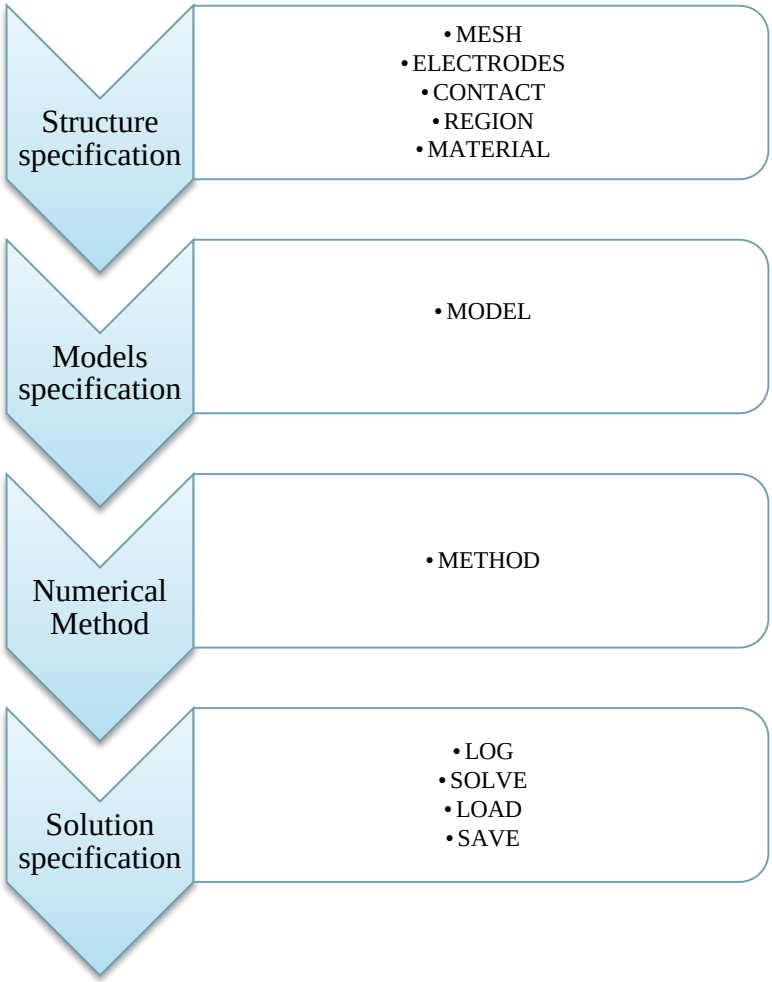

Figure 51 SILVACO simulation process

SILVACO store and load from files. It can work with two different files type. The first file type stores the structure data of the device. This file has the extension STR and it can be plotted in TonyPlot. Once opened in TonyPlot the graphic can be saved with different extensions or even exported to other file types. The other file type will contain the terminal characteristics, or the calculated data results of Atlas such as the IV data. This files type has extension LOG and it can be loaded by Atlas. Whenever SILVACO solves any device, the calculated data is stored in the LOG file which only needs to be created before any SOLVE statement and closed after the calculations. So, it is possible to generate different LOG files during one simulation to store the results separately.

SILVACO software has been developed for Silicon base devices; it means that in general the default parameters are set up for silicon properties. However, it is possible to perform simulations for different material devices such as ternary compounds. In this case SILVACO has different values that will replace the silicon ones only defining in the

statements of the ‘regions’ in the device the pre-established names for the different material such as GaAs, InGaAs, InAlAs, etc. In order to define a new material property in the code it is necessary to indicate in SILVACO the new parameter using the MATERIAL parameters statements (e.g. **MATERIAL name=InGaAs eg300=0.8 permitivity=1.2 affinity=3.3 nc300=1 nv300=1).** Generally, the parameters required for a new material are the energy gap of the material, the permittivity and the conduction and valence effective densities of states at 300 K. The material parameter can be defined for MATERIAL type, REGION number or region NAME; other parameters that can be defined such as mobility and impact parameters. The parameter definition must be performed carefully because each model needs different parameter definition, so if one of the needed parameters is omitted then SILVACO will automatically set up the default silicon parameter instead of the correspond material. So it is recommended to check model by model in order to be sure that all the needed parameters are defined in the material statements.

In order to perform the device modelling it is necessary to declare the model to be used, in other words, it is necessary to define the physic equations to be used during the device analysis. The equation selected depends directly of the studied phenomena. Some of the available models in SILVACO are related with the carrier generation, transport mechanisms and different recombination phenomena in which mobility values, recombination rates, carrier statistics and impact ionization rates, among other parameters, should be taken into account.

As is well known the electrons and holes experience increment and saturation of their velocities because of the electric field and its momentum and changes occur due to the scattering processes produced by lattice vibrations (phonons), impurity ions, other carriers and material imperfections. The statements to enable the analysis are:

- CONMOB - Concentration dependent, doping versus mobility
- ANALYTIC - Concentration and temperature dependent. Caughey-Thomas model
- CCSMOB - Carrier-Carrier scattering for high carrier concentration
- FLDMOB - Required to model any type of velocity saturation
- CVT - This is good for non-planar devices
- YAMAGUCHI - Includes perpendicular fields only for 300 K

The process responsible for the phenomena of generation-recombination analysed for SILVACO are the phonon transitions, photon transitions, auger transitions, surface recombination, impact ionization and tunnelling. These can be analysed using the models:

- SRH (Shockley Read Hall) – uses fixed minority lifetime for carriers and it must be used in almost all simulations.
- CONSRH (Concentration Dependent SRH) – Specifies Shockley Read Hall recombination using concentration dependant lifetimes.
- AUGER – Specifies Auger recombination. It will be important in the high current densities cases.
- Impact Ionization SELB and CROWELL. In a space charged region with sufficient revers bias the electric field accelerates the electrons, so if both sufficiently strong field and inter-carrier collision enough to allow high velocity increase are true then the free carriers acquire sufficient energy before collision with the crystal atoms. Thus, more free carriers are generated. IMPACT SELB is recommended for most of the cases as it includes temperature dependent parameters. Also available is the Crowell-Sze model for impact ionization (IMPACT CROWELL) using carrier scattering lengths.

  It is compulsory in SILVACO simulations to define the boundary condition. The boundary conditions supported in Atlas are:

- Ohmic contacts, an electrode is assumed by default condition to be ohmic, it can be set with CONTACT NAME= TYPE
- Schottky contacts : can be defined using WORKFUN parameter in CONTACT statement, the value must be on eV units
- Current boundary conditions, this can be set using CURRENT in the contact statement
- Lumped elements between bias and device (Resistors, capacitors, inductances)
- Distributed contact resistance to take into account the finite contact resistance

SILVACO can calculate all the previous models using different numerical methods; this software discretizes the problem to make successive estimations of the solution. SILVACO has 3 different numerical methods:

- Newton, this method linearizes a non-linear problem, it implies long time processing but it converge easily due to the huge calculations. Sometimes this method fails to find the solution and a wrong mesh definition or structures failed considerations could be the reasons.
- Gummel, This model is not available for lumped elements and it is really useful when the equations are weakly coupled to get a linear convergence. It will truncate the out of range values (errors) in order to avoid non-convergence.
- Block, when the energy balance is included in the analysis of the device this numerical method is recommended as well as the lattice heating. It will make the approximation with some equations coupled and some decoupled.

The numerical method selection depends on the structure and the given parameters for the solution, generally for solar cells it uses the Newton method such that it can converge faster than the others although it implies a long time for calculations. However, it is possible to reduce the processing time by managing the mesh design carefully.

Once the models have been defined, SILVACO needs the voltage definition in the electrodes or the values for the boundary conditions, so Atlas is able to calculate the current through each electrode and other quantities as electric fields and carrier concentrations. To turn on the problem solution the statement SOLVE must be invoked. It is important to make the first solution with equilibrium conditions, this can be made with the SOLVE INIT statement and it obtains the bias steps for the next solutions. It is important to set an adequate bias steps in order to reduce the processing time but keeping the results accurate. For solutions, SILVACO is limited to 75 V otherwise the program would try to ramp up to 200 V and the solution never converges.

All the results obtained are stored on the LOG files as mentioned previously, these files can be plotted on TonyPlot. In order to have better visualization it is possible to make SET files for plotting purposes. Once plotted it is possible to overlay different curves, scale the graphs and export the data to other file types.

In order to simulate a solar cell it is absolutely necessary to simulate the light source and this is certainly possible with SILVACO. It has an AM (0, 1.5) solar spectra data; it can be enabled with the BEAM statement. It is part of the LUMINOUS module and it can be

either monochromatic or multispectral. It includes one function to trace a specific number of rays in order to simulate a 3D device and solve problems in deep structures. Using the ray tracer option the user is able to analyse the device with anti-reflective coating applied on the device surface invoking the INTERFACE parameter into the simulation code so, the IV curves under light condition can be obtained. Thus, the efficiency of the cell, plot of the quantum efficiency, checks of the band diagram are calculated from the electrical simulated data which is stored into the LOG file previously defined. It is then necessary to bias the device (apply ramp voltages on the cathode). The LOG file will include the current data according to the bias applied, it is possible to define the initial data (generally Vanode=0), the final value (Vfinal) and the increment steps (Vstep). The units are volts (V). SILVACO assumes that we define the anode next to the p-type semiconductor.

Parameters optimization

The purpose of simulation is to try to predict the behaviour of the devices to save material resources and fabrication time. Sometimes the measurements are not so close to the simulation results and this can be improved by calibrating SILVACO. The error or discrepancy can be caused by a lack of accurate definition of parameters, the use of semiconductors that are different to Silicon (it is important to recall that SILVACO was made for Silicon Devices in the first instance) or simply degradations in the fabrication process.

It has been found in some simulations that the most common errors in simulations are the doping levels defined or that the material parameters are not enough or the material parameters have the wrong values. Mesh definition can affect the accuracy of the measurement so it is absolutely necessary to try to reduce the mesh lines to a maximum without loss of accuracy, it is a compromise. In addition, it could be external effects at the moment of performing the measurements or error during the fabrication process. In order to apply calibration to the simulation it is necessary to review all the models used for the calculations, check that the SILVACO output file in order to find errors or possible omission values due to a wrong statement typing and convert correctly the units in order to compare with measurement data. However, one of the biggest inconveniences of SILVACO for group III-V semiconductor solar cell is the semiconductors parameters and default data, the user needs to be very careful in the introduced data in order to obtain meaningful simulation results.

4.5.2 Material optimization process

The SILVACO optimisations presented many issues in the accuracy of the results due to the differences between the database material parameters and the real ones. It is true that SILVACO can calculate several parameters as a function of the structure definition or even get some parameters directly from the code, but the used material system is still under investigation so that many of the parameters are still unknown or their values are uncertain which leads to inaccurate simulation. However, if the simulated results are close to the measured results, simulation can lead to device behaviour prediction. The material chosen for simulation is XMBE242, the lattice matched material system. The reason for choosing a lattice matched system is that lattice stress effects are eliminated and we can expect more accurate results.

The effect of QW inside InAlAs pin diode

The epilayer shown in Figure 52 was programmed in SILVACO code. The program is shown in Apendix D.

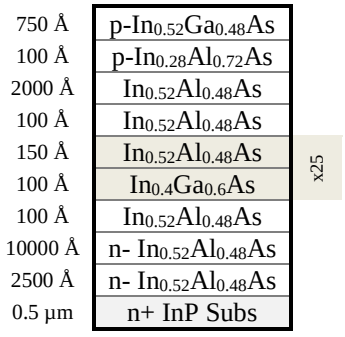

Figure 52 Epitaxial details for sample XMBE242, InGaAs/InAlAs lattice matched system

The modelling of 20 $In_{0.52}Al_{0.48}As/In_{0.4}Ga_{0.6}As$ layers, lattice matched, where using the SILVACO material datasheet. The simulated results were with good agreement compare with the measured ones. By using the correct mesh, and contrast the simulated results versus measured data, the simulation run perfectly. The simulated JV curve, in the

absence of light, exhibited an excellent agreement with the measured one as can be seen in Figure 53.

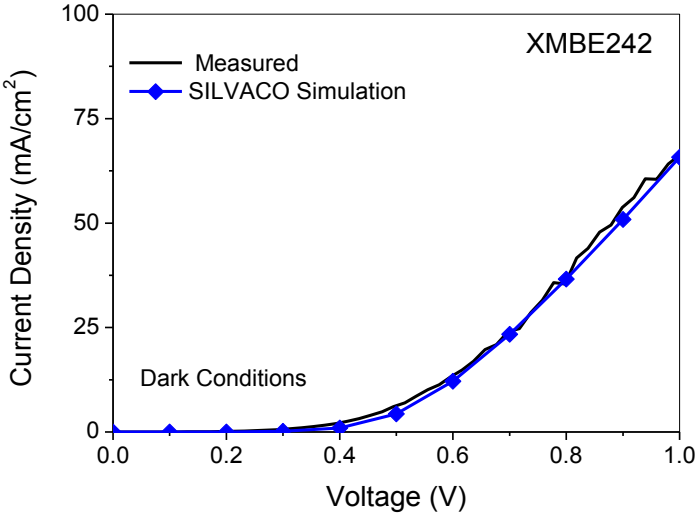

Figure 53 Measured vs Simulated data of JV curve for XMBE242 (lattice matched InGaAs/InAlAs MQW) for dark conditions

Exposing the material to light energy, 1 sun light, the BEAM function was used in SILVACO. The power energy for this was 1e-1, which gives a power light of 100 mW/cm^2 (1 sun) using AM1.5 spectrum. The comparison between measured data and simulated data is depicted in Figure 54. This time, the agreement between the measured data and the simulated data was not as good as in the dark conditions. However, the modelled material data was quite good.

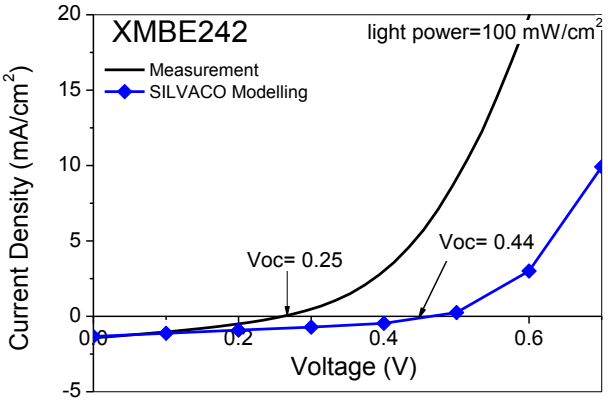

Figure 54 Measured vs Simulated data of JV curve for XMBE242 (lattice matched InGaAs/InAlAs MQW) under light conditions using 1 sun (power light=100 mW/cm2).

From the results shown in the two previous figures it can be seen that the material XMBE242, 20 InGaAs/InAlAs lattice matched MQW, exhibited in practice very low efficiency. This is due to the very low bandgap material which leads to a very small open circuit voltage as confirmed in the simulation too. In the case of light conditions, the disagreement can be due to the reflection on the material surface which was not considered in the SILVACO code.

Quantum Well material optimisation

The optimization process was divided into 6 different steps:

1. Barrier-Well thickness optimization
2. Spacer layers (intrinsic) thickness optimization
3. n/p (Base/Emitter) layer thickness optimization
4. Window layer thickness optimization
5. Buffer thickness optimization
6. Final structure

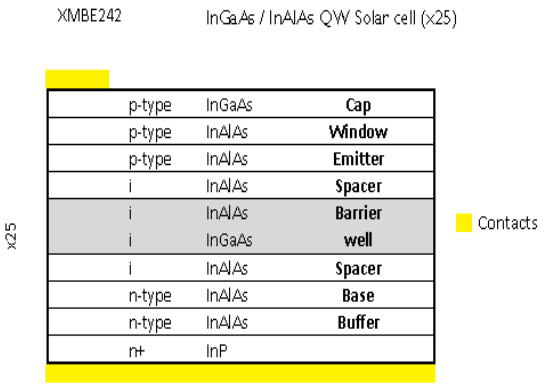

In every step, only one layer thickness was modified, and the J-V characteristics under 1 sun illumination were obtained for each modification and compared with the previous stage in order to choose the optimum thickness. The results of the optimization are presented in the next subsections. The results of each step are shown in Appendix C. The final structure has the optimal thicknesses shown in Table 9. The J-V simulation is shown in Figure 55. The improvement only accounted for an extra ~2 mA/cm^2 for the short circuit current density (Jsc) and an extra ~100 mV for the open circuit voltage and thus the simulation of this structure is pretty good and the obtained efficiency is very much closer to the predicted SILVACO simulation, validating the choice of the materials parameters used in the simulation.

Table 9 Final structure with optima layers for XMBE242

XMBE242 InGaAs/InAlAs x25 MQW Solar cell				
Material	**Doping**	**Layer**	**Original tck Å**	**Optimum tck Å**
InGaAs	p-type	Cap	750	750
InAlAs	p-type	Window	100	100
InAlAs	p-type	Emitter	2000	50
InAlAs		Spacer	100	100
InAlAs		Barrier	150	80
InGaAs		Well	100	50
InAlAs		Spacer	100	100
InAlAs	n-type	Badse	10000	9000
InAlAs	n-type	Buffer	2500	2500
InP	n+	Substrate	0.6um	0.6um

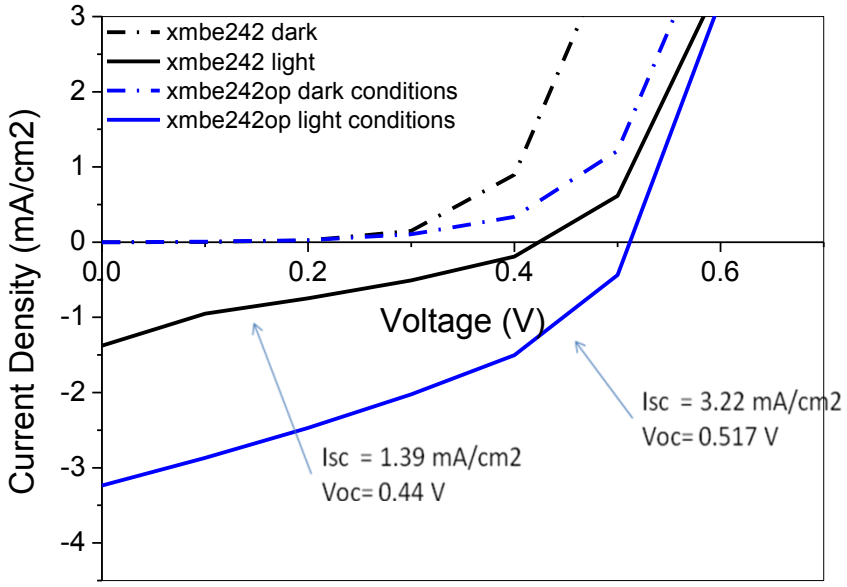

Figure 55 Optima layer thicknesses for XMBE242 J-V simulations

Table 10 Original and Optimised structure efficiency calculations (simulated values)

Sample	Isc	Voc	Im	Vm	FF	η (Eff)
	mA/cm²	V	mA/cm²	V	%	
Original	1.39	0.44	0.6	0.26	25.5	0.15
Optimised	3.22	0.51	1.9	0.33	38.2	0.62

Despite an appreciable increase of both the short circuit currents and open circuit voltages it is clear that the final efficiency (Table 10) is small and that an all InAlAs pin diode is a not an effective solar cell despite its band gap being close to that of GaAs.

In terms of EQE, a very good agreement between the VMBE2017 (15 MQWs $In_{0.4}Ga_{0.6}As/In_{0.52}Al_{0.48}As$ tensile strained) which can be seen in Figure 56, and taking this simulation parameters a parametric changes were performed to the structure. The number of quantum wells was modified to see the effect of the wells periodicity in the EQE.

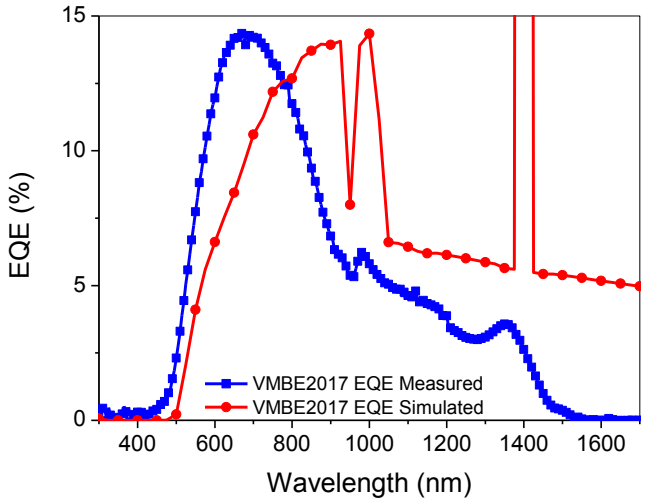

Figure 56 External Quantum Efficiency for vmbe2017 simulation approaches

The periodicity was varied within the range from 10 to 35 wells. In Figure 57 it can be seen the unexpected effect of the quantum wells periodicity. The more active material, the more light absorption was expected in the material to be converted but in effect the optimal QW number is ~ 10 and larger numbers only lead to a decrease to the EQE. The latter is contrary with the premise that the EQE will be increased as increasing the active material quantity but this discrepancy should be analysed in more details as a future work involving materials growth and devices fabrication and characterisation. In addition, the correct optical parameters for the chosen material compositions should be extracted from real materials to be defined in SILVACO to optimise the simulation results.

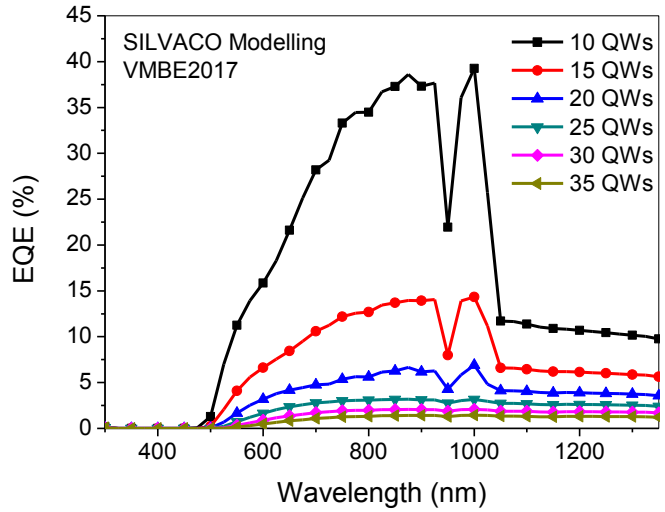

Figure 57 Different Quantum Wells periodicity simulation. It is evident that there is EQE enhancement by decreasing the QW periodicity.

4.6 Conclusion

This section work consisted of characterization, fabrication and simulation of various solar cells structures grown by MBE. The aim of the work was to match the simulated results with the experimental ones in order to get accurate parameters for the devices and their efficiency. The latter is important as it allows the design of improved solar cells. While SILVACO is a 'non-transparent' simulation program, and although in most of the commercial simulation software it is impossible to know what the program is doing, in SILVACO one can modify the models in order to get better simulation results. The key factors for reliable simulations are the careful selection of the device parameters and correct definition of the mesh. Furthermore, the solar cells physics is very important in SILVACO in order to perform simulations that make sense.

According to the results, the highest measured efficiency was obtained for the high temperature grown GaAs/AlGaAs sample (vmbe1661). However, the quantum efficiency calculations showed that this sample can operate only in the visible range. Therefore, it is desirable to enhance the absorption range of the cell. In this sense, InGaAs/InAlAs samples have been proven to have better absorption in the infrared spectrum as indeed

demonstrated in the long wavelength experiments. This is desired, because the cell can absorb lower energy light than the GaAs/AlGaAs devices.

The insertion of quantum well structure resulted in the reduction of the open circuit voltage because of the much smaller band gap created by the wells. However, the short circuit current was increased, which is something desirable as implied that the power operation point is increased.

Several simulations attempts have been performed in order to get the external quantum efficiency of the cell. However, SILVACO's optical parameters files appeared to be limited (it only goes from 300 nm to 800 nm) and thus a modified file was created in SILVACO's C-Interpreted syntax. It is clear that the n-k coefficients file (optical properties) is not correct at all. However, the trend of the EQE curve is close to the measurements.

According to the measurement of the EQE samples, it is clear that by increasing the number of the wells the efficiency is reduced. The latter can be seen in the simulation of the vmbe2017 structure, where the periodicity of the QWs changed from 10 to 35. Although the trend is correct the simulation has to be refined.

CHAPTER 5

QUANTUM DOT DEVICES: RESULTS and DISCUSSION

5.1 Introduction

The fundamental drawback of low open circuit voltage in low band gap $In_xGa_{(1-x)}As$ MQW structures naturally led to an investigation into emulating a 1eV band gap using InAs quantum dots in GaAs. A detailed study of vertically stacked quantum dot array materials, including room temperature characterisation, temperature dependence analysis and some novel material stressing technique to observe the changes in the electric field in the crystal is presented in this section. In addition, is included a study of the effect of anti-reflective coatings designed to reduce the light reflection on the device surface in order to enhance the light absorption and to improve the device efficiency is included. Novel attempts to modify the electric field of the lattice by external stress applied is also investigated.

5.2 InAs/GaAs quantum dot inter-dot doping analysis

5.2.1 Structural characterisation

Because of the many parameters that are involved in the MBE growth process, the final material will have slight variations in thickness and composition and dislocation formations (if any), it is thus important to undertake structural characterization to estimate both the crystal quality and the actual structural values. The structural characterization was made using a Bede QC200™ Double Crystal X – Ray Diffraction (DCXRD) with an X-ray source wavelength of 1.54 Å and with random polarization. A Ge crystal was used as a reference crystal. The epitaxial structures and samples used are summarised below in Figure 58:

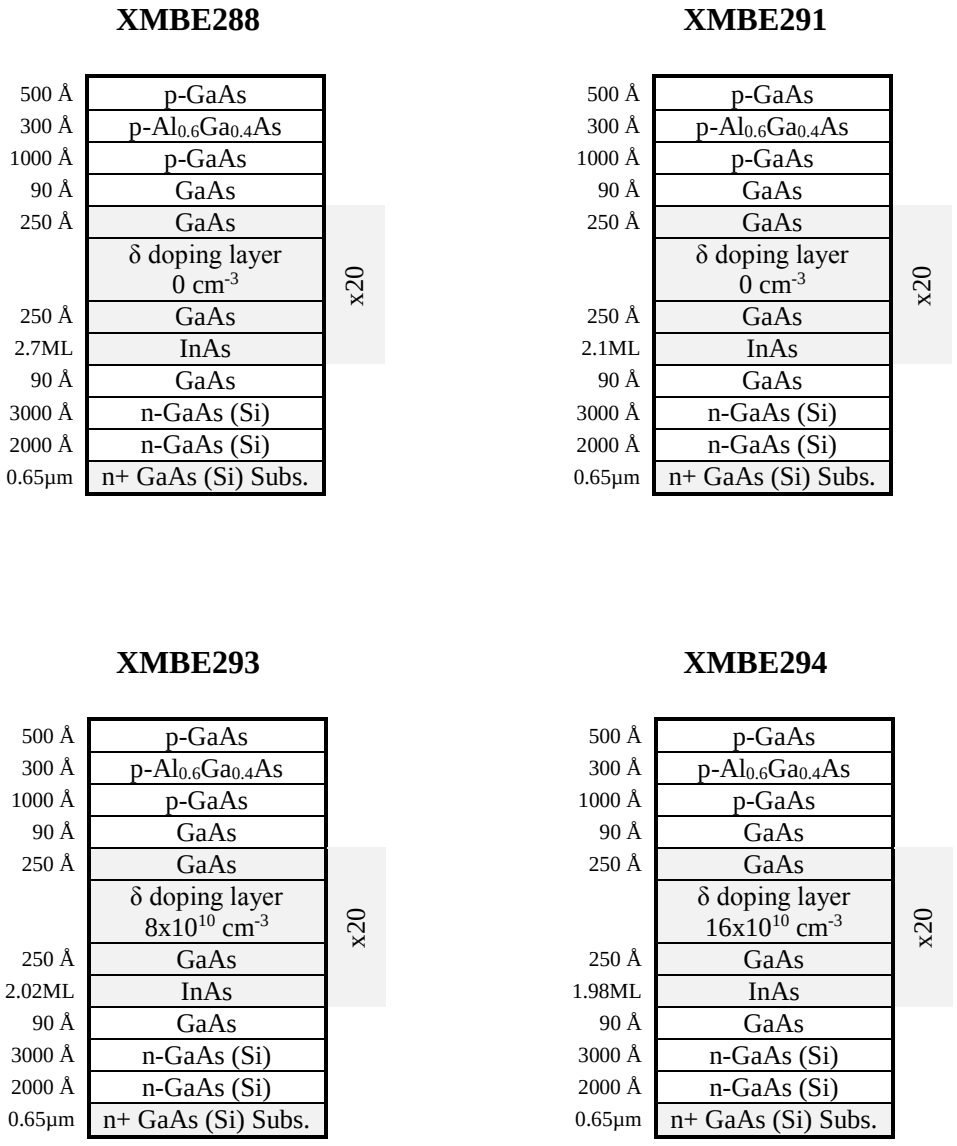

Figure 58 InAs/GaAs QD epitaxial details for different inter-dot doping profile study

The DCXRD measurement for sample XMBE288 is shown in Figure 59. The structures were simulated using RADS Mercury software in order to extract the actual thicknesses. The thickness for the wetting layer in sample XMBE288 is around 2.6 ML where the intensity of the satellite peaks is fairly weak and is broad implying a large amount of crystal distortion in the lattice, suggesting the presence of structural defects [90].These defects will limit the device energy conversion since they act as non- recombination centres for the generated carriers. The extracted values are very close to the nominal values.

For Sample XMBE291, the DCXRD curve is shown in Figure 60. It has an InAs wetting layer thickness of 2.02ML and shows narrow peaks uniformly spaced with a very small shoulder on the left side of each satellite peak as depicted using an arrow in the inset of Figure 60 due to a vertical correlation between layers. This shoulder is evidence of an embedded vertical structure according to Srinivasan et al [91], [92].

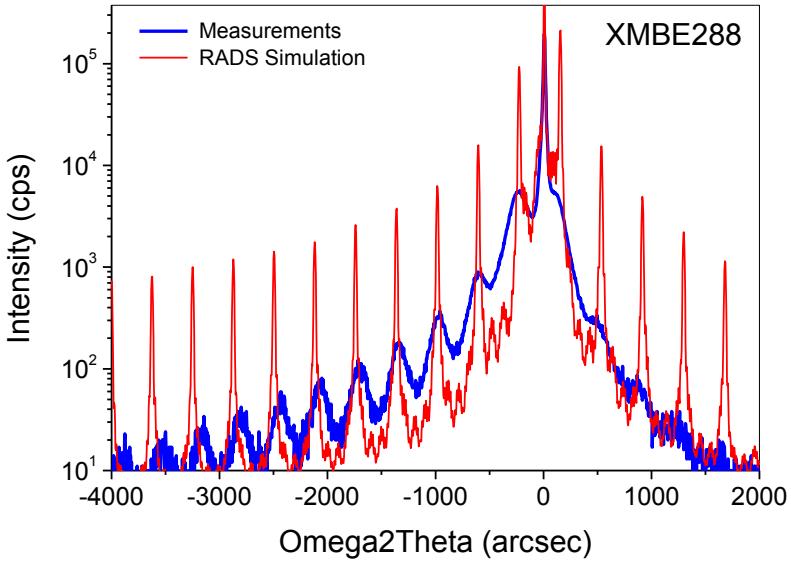

Figure 59 DCXRD curves for InAs/GaAs quantum dot sample XMBE288. Wetting layer thickness of 2.6 ML. Inset, depicted the satellite peaks in detail from -700 to -100 arcs.

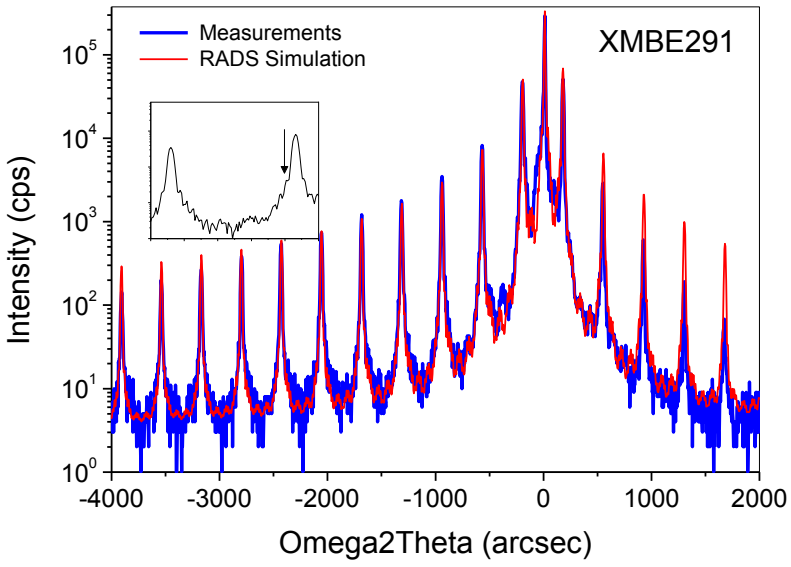

Figure 60 DCXRD curves for InAs/GaAs quantum dot sample XMBE291. Wetting layer thickness of 2.02 ML. Inset depicted the satellite peaks in detail from -700 to -100 arcs

Structural characterisation for sample XMBE293 (Figure 61) and XMBE294 (Figure 62) the quality of the materials is excellent too; the structural characterization shows narrow uniformly spaced peaks with Full width at Half maximum (FWHM) of less than 18arcsec across the entire period demonstrating extremely low distortion in the lattice. The thickness of the InAs wetting layer is 2.02 and 1.98 ML for sample XMBE293 and XMBE294 respectively and again the shoulders on the left side of the satellite, insets in their respectively figures, show a good correlation between the stacked QD layers.

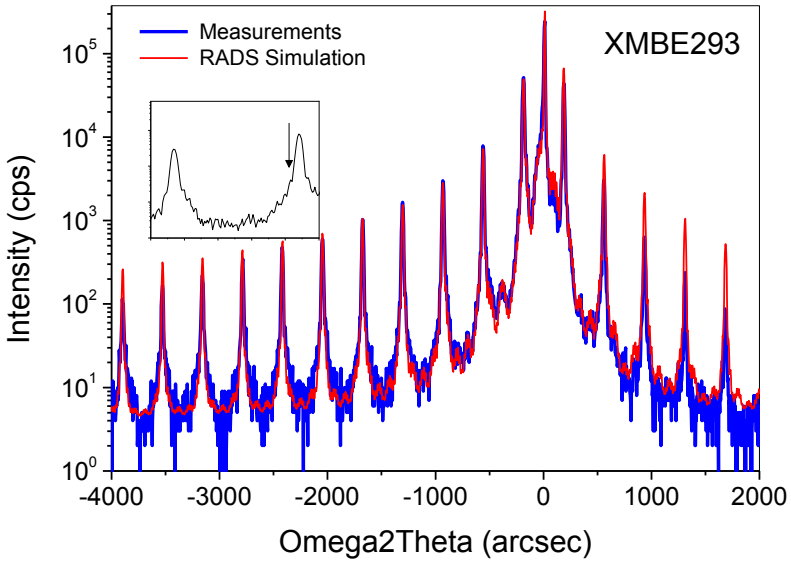

Figure 61 DCXRD curves for InAs/GaAs quantum dot sample XMBE293. Wetting layer thickness of 2.02 ML. Inset, depicted the satellite peaks in detail from -700 to -100 arcs

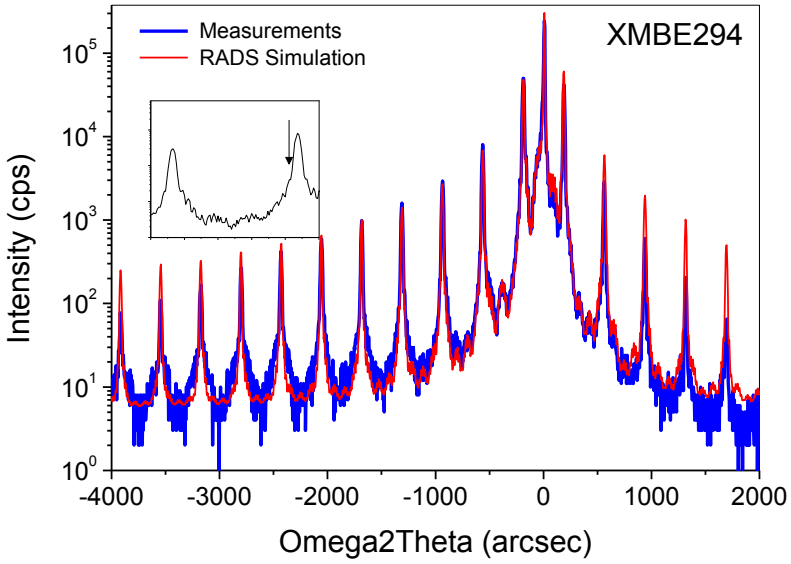

Figure 62 DCXRD curves for InAs/GaAs quantum dot sample XMBE294. Wetting layer thickness of 1.98 ML. Inset, depicted the satellite peaks in detail from -700 to -100 arcs

5.2.2 Optical characterisation

The room temperature Photoluminescence (PL) QD materials responses were performed using a green 532 nm (2.33 eV) laser source. Two detectors were used: a Si CCD array - with sensitivity range from 600 to 1200 nm (1.03 - 2.03 eV) and InGaAs photodiode array- from 900 to 1800 nm (0.68 - 1.33 eV) using an Accent RPM2000^{TM} mapping system.

Figure 63 shows the PL measurement from the epi materials measured using the CCD (Figure 63a) and InGaAs (Figure 63b) detectors where new sub bands transitions can be observed. In the undoped QD sample (2.6 ML InAs) only one transition is present at 1.42 eV which corresponds to the GaAs bandgap. During growth, the InAs thickness in sample XMBE288 exceeded the critical value of ~2.1 ML, resulting in relaxed quantum dots and the generation of dislocations (as evident in the DCXRD measurements by the very poor FWHM). These dislocations act as non-radiative recombination centres, which are responsible for the extremely low PL intensity at 1.1 eV [93]. In contrast, intense PL is observed from samples XMBE291, XMBE293 and XMBE294 with peaks at 1.42 eV (GaAs bandgap), 1.35 eV (InAs wetting layer) and ~1.2 eV (QDs). It is also evident that the peak intensity increases with increasing doping concentrations due to the increased carrier concentrations inside the QDs.

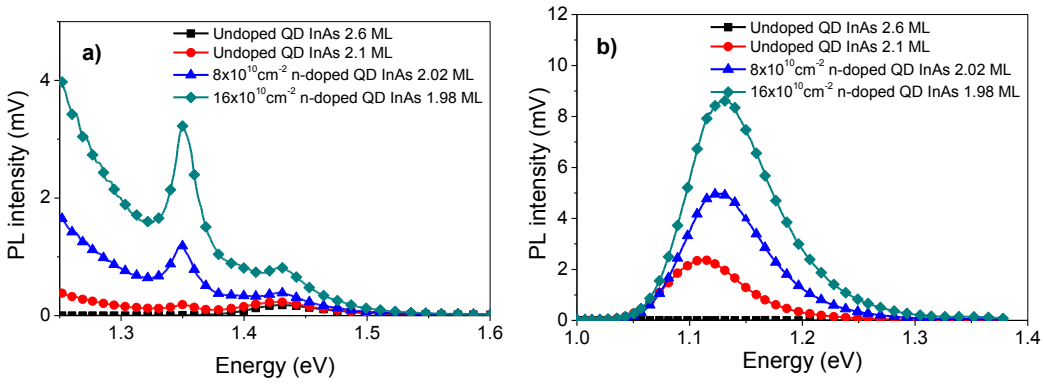

Figure 63 PL spectra or samples XMBE288, XMBE291, XMBE293 and 294 using both a) CCD and b) InGaAs detector at room temperature. New states at 1.37 eV and 1.2 eV are added due to QD insertion.

For the long wavelength PL measurement, a small blue-shift in the QD PL peak is apparent. Comparing Sample XMBE291 with both samples XMBE293 and XMBE294,

the inter-doping dots generates 20meV blue-shift in the PL peak. The latter may be as well because of the dots size difference due to the wetting layer thickness changes.

The optical characterisation exhibited the addition of two energy transitions that can be located within the QD material band diagram shown in Figure 64.

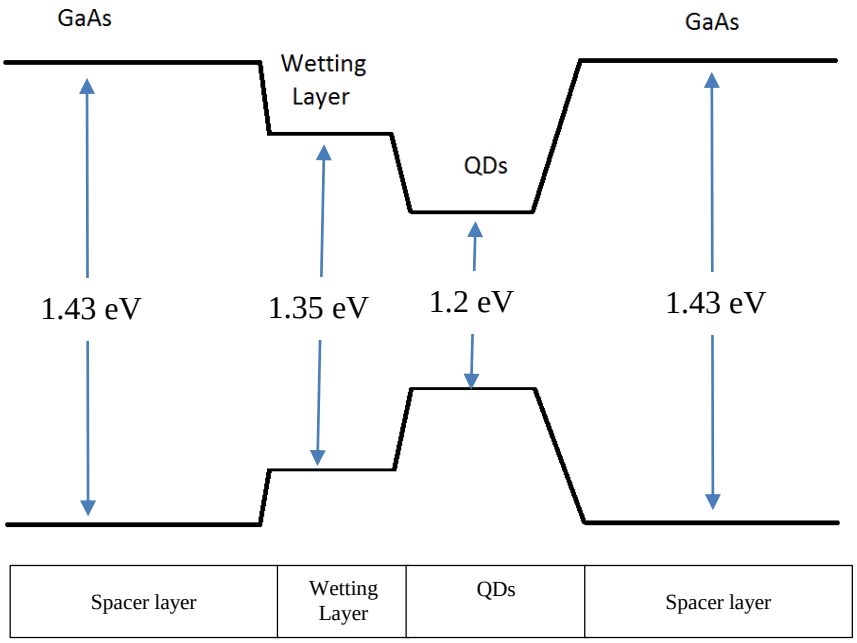

Figure 64 InAs/GaAs Quantum dots material band diagram

5.2.3 Electrical characterisation

Cylindrical diodes were fabricated in the form of mesa structures with a diameter of 250 μm. Metal contacts were evaporated on both front and back sides. For the front contact, a ring of 50 nm Ti(50nm)/Au(100 nm) has deposited. The back contact has made of AuGe(50 nm)/Au(400nm) and annealed at 320 ^{o}C for 2 minutes.

In order to measure the electrical response of the devices, the sample were diced up and mounted on TO-46 headers and finally bonded. For reference, J-V measurements were performed using 1 sun calibrated Solar simulator in the Department of Physics at the

University of Lancaster facilities. Thereafter, the Incandescent lamp height could be adjusted to get the same short circuit current density measured as the one in the Lancaster laboratory. [94]

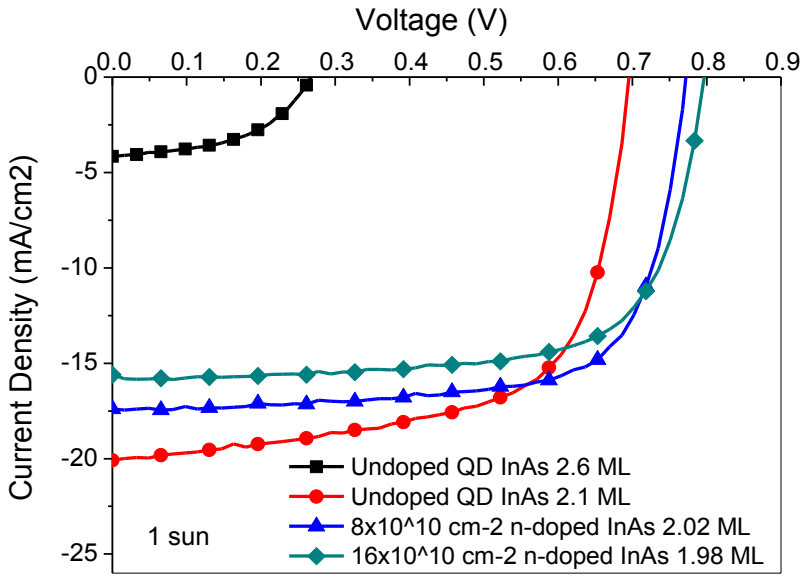

Figure 65 Room temperature J-V characteristics of the various quantum dot samples PV devices at 1 sun (100 mW/cm^2). Doped samples exhibit high open-circuit voltages up to 0.8 V while the short-circuit current density is higher for the undoped sample with a 2.1 ML InAs layer.

The 1 sun J-V measurements are shown in Figure 65. The poor performance of sample XMBE288 is in agreement with the low structural quality. In terms of open circuit voltage, it can be seen that the insertion of n-type doping increases the open circuit voltage from 0.7 volts in the undoped sample XMBE291 up to 0.8V in sample XMBE294. It should be pointed that the quantum dots act as non-recombination centres for generated free carriers, but introducing doping atoms, this recombination effect is reduced enhancing the Voc of the material [63]. However, the short circuit current density (Jsc) is reduced with the increase in delta doping profile. Jsc drops to ~15mA/cm^2 in sample XMBE294 (16x10^{10} cm^{-2} n-doped QD) from 20 mA/cm^2 in the undoped sample XMBE291. This result is contrary to that reported in reference [95], using lower delta doping profile, and in which the Jsc is enhanced as the doping profile is increased. Nevertheless, in terms of Voc, the inter-dot doped material behaviour is consistent. It could be that the dots are acting as radiative recombination centres (as evident by the strong PL) rather than extraction centres. Overall the increased doping led to an increased power conversion efficiency of 9.7 % in sample XMBE293.

Table 11 InAs/GaAs QD device efficiencies calculation

	Jsc	Voc	Im	Vm	FF	η (Eff)
	mA/cm^2	**mV**	**mA/cm^2**	**mV**	**%**	**%**
XMBE288–Undoped QD (2.7ML)	4.1	272	2.9	187	48	**0.5**
XMBE291–Undoped QD (2.1ML)	20.1	696	15.8	571	64	**9.0**
XMBE293–n-doped QD 8x10^{10} cm^{-2}	17.4	733	14.8	653	76	**9.7**
XMBE294-n-doped QD 16x10^{10} cm^{-2}	15.6	797	13.6	653	71	**8.9**

Figure 66 shows the external quantum efficiency (EQE) measured from the solar cells measured using a calibrated 100 W quartz-halogen lamp through a ¼ metre monochromator for samples XMBE288–Undoped QD (2.7ML), XMBE291–Undoped QD (2.1ML), XMBE293–n-doped QD 8x10^{10} cm^{-2} and XMBE294-n-doped QD 16x10^{10} cm^{-2}.

It can be seen that a quantum efficiency of higher than 30% is achieved in GaAs bandgap (1.43 eV) for all the samples except for the sample with 2.6ML. The QD samples all show enhanced EQE below the GaAs bandgap down to 1.1 eV. The increased doping reduces the EQE over the energy range 1.2-1.6 eV compared to the undoped material, which reduces the short-circuit current.

It is clear from the figure that the Inter-dot doped materials show a reduction in EQE in the range from 1.2 to 1.6 eV compared with the undoped material. However, the obtained values (~ 20%) are still excellent compared with values reported for AlGaInAs quantum dot devices in [96] where the lowest energy absorbed is at ~1.24 eV.

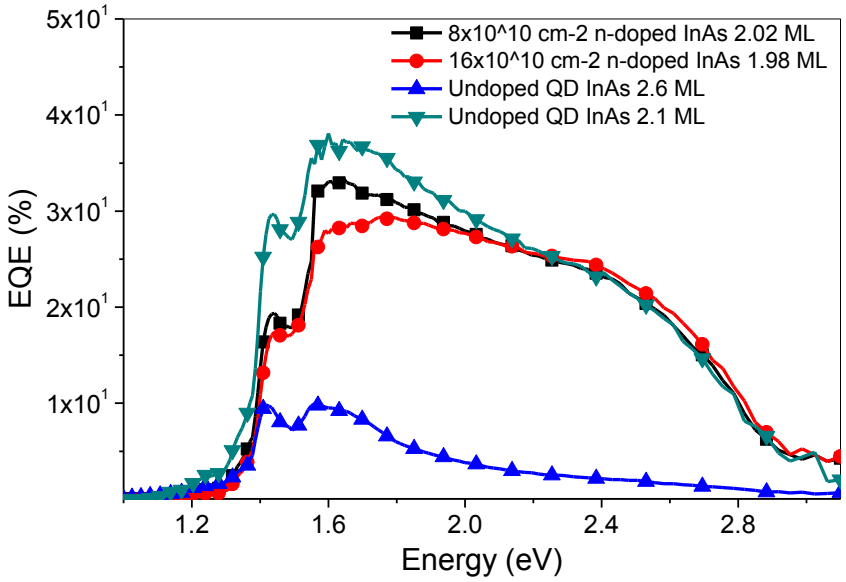

Figure 66 Room temperature External Quantum Efficiency (EQE) spectra for the QDs devices.

The agreement between the obtained IV (Figure 65) and EQE (Figure 66) for InAs/GaAs QD materials, shows that the material optical properties are strongly related with the energy conversion efficiency rates. The extremely low short circuit current achieved for the undoped dots with 2.7 ML wetting layer thickness is a consequence of the very low material absorption. Low absorption rates generates that the quantity of absorbed photons drop having a low short circuit current as consequence. However, for the materials whit a wetting layer thickness around 2 ML, the external quantum efficiency goes up to 40% exhibiting good absorption rates and contributing so to get efficiencies up to 9%.

5.3 InAs/GaAs quantum vertical array periodicity analysis

5.3.1 Structural characterisation

In this section, several materials with different vertical periodicity of the InAs/GaAs quantum dot layers are studied; just like the quantum wells materials case, the structures were simulated using RADS software to obtain the actual thickness of each layer from the DCXRD measurement data.

However, it is necessary to be clear that the observed results are exhibited on the material as a consequence of the quantum dots insertion or any of the further structure changes

(e.g. insertion of doping atoms within the host lattice or changes in the vertical array periodicity). The latter involves the necessity of growing a control sample. This sample consists of GaAs material without any QD. The control sample material ID is XMBE312.

The rest of the samples are configured with 5, 10 and 20 layers of InAs/GaAs quantum dots (XMBE312, XMBE311 and XMBE291 respectively). The epitaxial structures and samples used are summarised below in Figure 67:

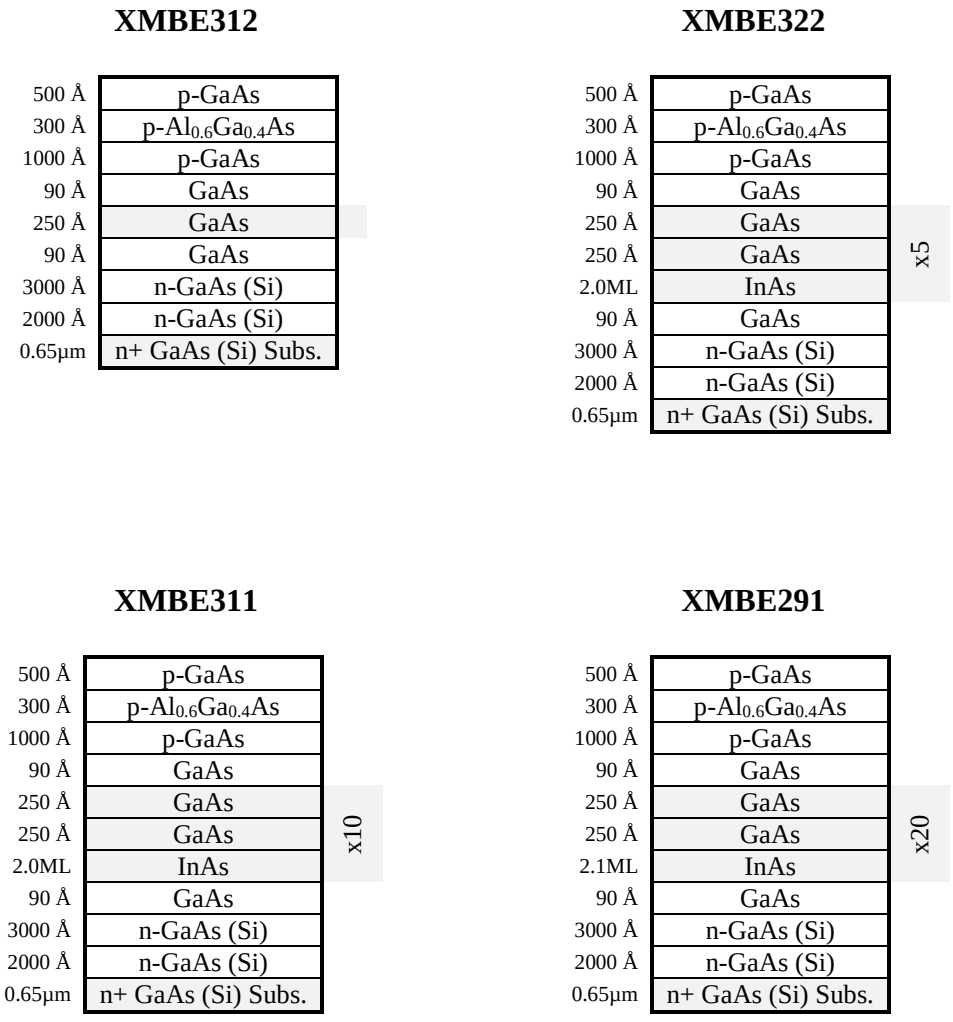

Figure 67 InAs/GaAs QD epitaxial details for different periodicities study.

For sample XMBE312 depicted in Figure 68, the rocking curve exhibited a strong narrow peak implying a good quality of the crystal. At the left side of this peak, appears a second peak which is slightly smaller than the main peak which corresponds to the $Al_{0.5}Ga_{0.5}As$

window layer. For sample XMBE322 (x5 periodicity), depicted in Figure 69, the strongest peak corresponds to the GaAs substrate and it is surrounded by several satellite peaks. This time, the InAs wetting layer thickness, obtained by RADS fitting, is 1.98ML. The satellite peaks are not as narrow as expected, however they are uniformly spaced and a small shoulder can be seen at the sides of each satellite peaks indicating a good vertical alignment of the dots.

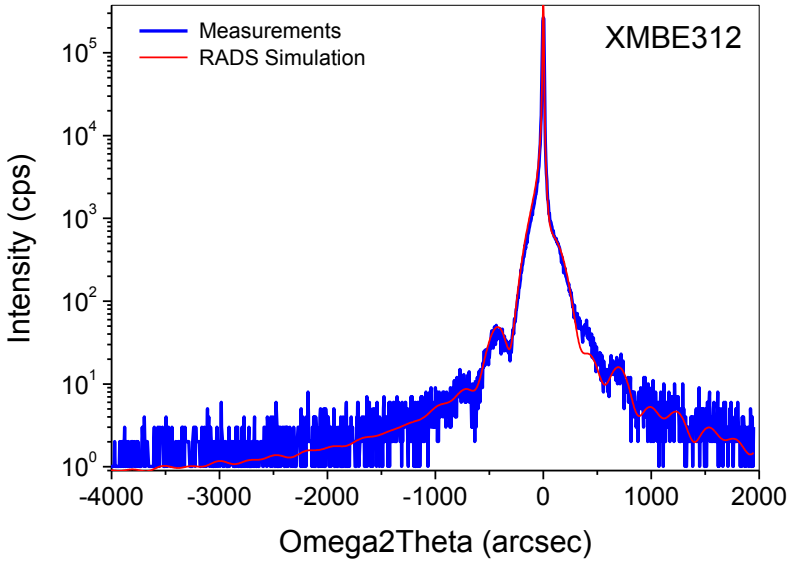

Figure 68 DCXRD curves for InAs/GaAs quantum dot sample XMBE312 without any quantum dot within the lattice.

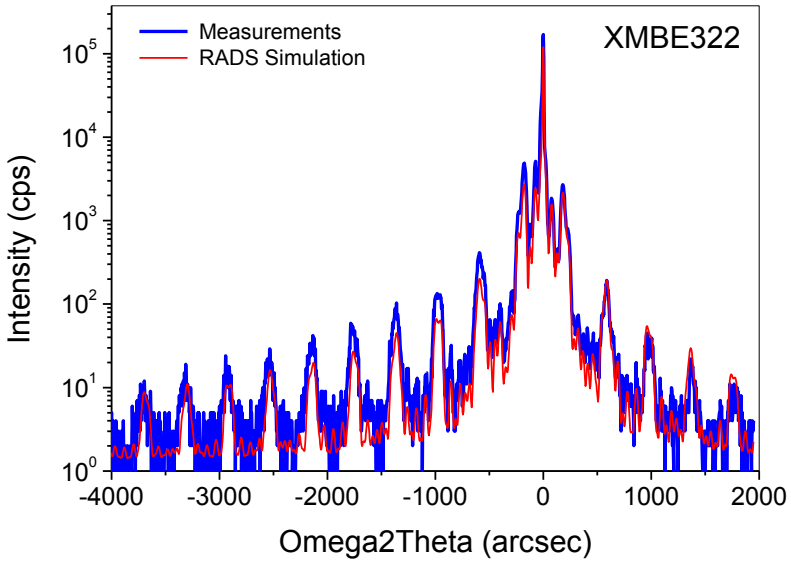

Figure 69 DCXRD curves for InAs/GaAs quantum dot XMBE322 including 5 quantum dot layers.

The rocking curve for sample XMBE311 which has 10 quantum dots layers is shown in Figure 70. By increasing to 10 the number of vertically stacked layers, the satellite peaks are narrower compared with the ones for XMBE322. The satellite peaks exhibited again the left side shoulder which is, according with Srinivasan et al [92], an indication of very high quality crystal. The calculated wetting layer thickness for samples XMBE322 and XMBE311 is 2ML. Sample XMBE291 (x20 periodicity) , shown in Figure 71, has a wetting layer thickness of 2.02ML and shows narrow peaks uniformly spaced with a very small shoulder on the left side of each satellite peak due to a vertical layers correlation.

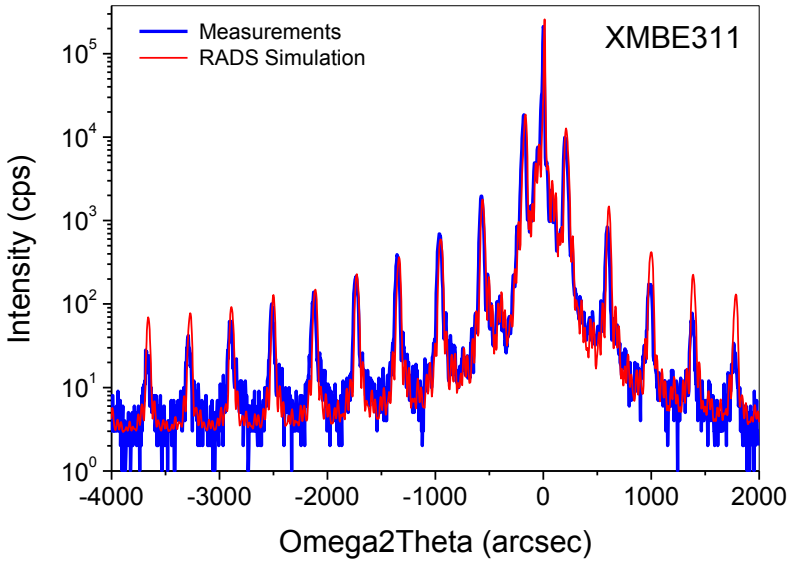

Figure 70 DCXRD curves for InAs/GaAs quantum dot sample XMBE311 including 10 quantum dot layers.

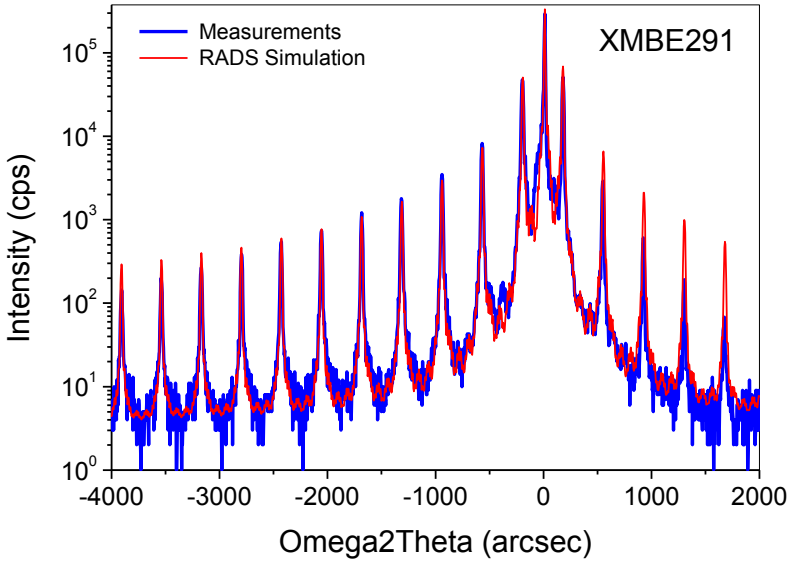

Figure 71 DCXRD curves for InAs/GaAs quantum dot sample XMBE291 including 20 quantum dot layers.

The structural characterization for all the vertical quantum dos periodicity samples shows narrow uniformly spaced peaks with Full width at Half maximum (FWHM) of less than 18arcsec across the entire period demonstrating extremely low distortion in the lattice and showing in general an excellent vertical correlation.

5.3.2 Optical characterisation

Figure 72 shows the PL measurement where new sub bands transitions can be observed. The control sample (without quantum dots incorporated within the lattice) exhibits only one transition at 1.42 eV which corresponds to the GaAs bandgap as expected. However, the samples including quantum dot layers show two additional optical transitions below the GaAs band gap. The new transitions are located at 1.35 eV and 1.2 eV which corresponds to the InAs wetting layer and the QD optical transitions.

As can be seen in Figure 72, as the number of quantum dots layers increases, the photoluminescence peaks intensities reduces. This is because the quantum dots act as recombination centres reducing the radiative recombination rates. In addition, the quantity of material will change as the periodicity changes, which impacts directly in the photoluminescence peak levels. For the optical transition located at 1.42 eV, the sample XMBE322 (x10 QD layers) displayed the lowest intensity. For the 1.35 eV transition, the intensity of the PL peak is reduced as the periodicity is increased. Contrary to that, the 1.2 eV transition increases drastically as the periodicity increases. So, the radiative recombination in the Dots increases as the periodicity increases and the opposite occurs with the wetting layer radiative recombination.

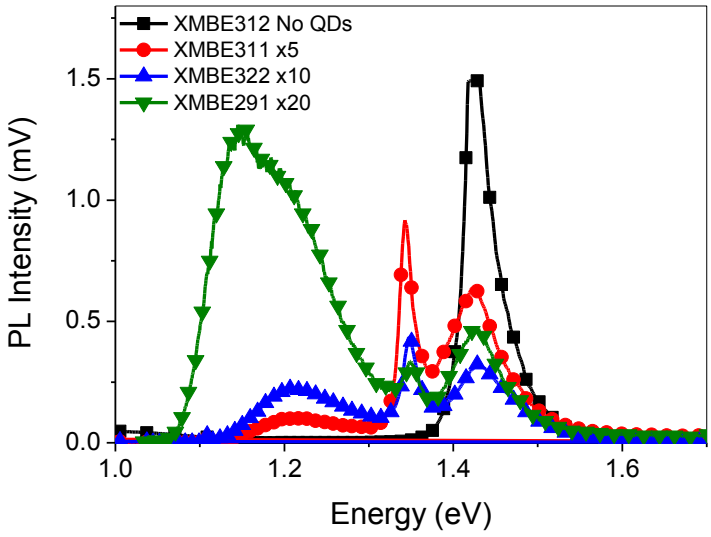

Figure 72 PL measurements for InAs/GaAs material system with different vertical periodicity

5.3.3 Electrical characterisation

J-V measurements at 1 sun light intensity were performed; the results are shown in Figure 73. The control sample showed the highest efficiency with a short circuit current density of 19.2 mA/cm^2 and an open circuit voltage of 800 mV. For the QD samples, the insertion of quantum dots reduces the open circuit voltage due to the increase in the recombination in the material. It can be seen that as the periodicity increases the open circuit voltage is reduced. However, for the short circuit current, the more quantum dot layers the more generated current. This is consistent and is due to the increase in the active material volume within the lattice which increases the material energy absorption.

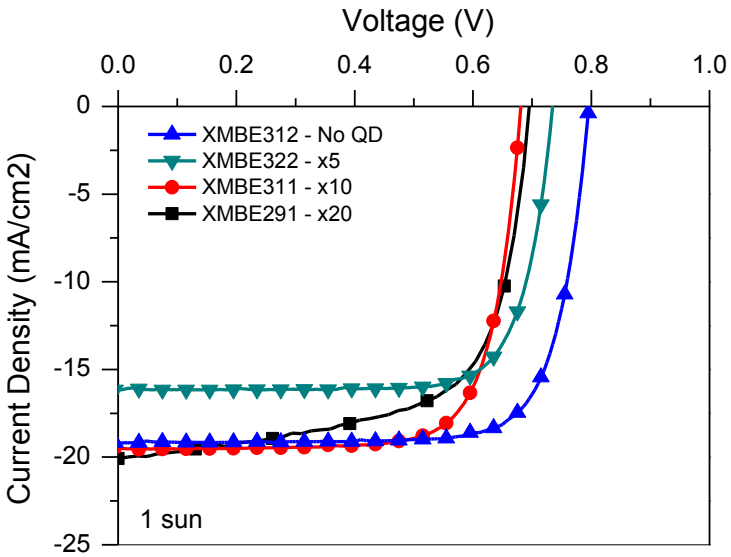

Figure 73 Room temperature J-V characteristics of the various quantum dot samples PV devices at 1 sun (100 mW/cm2). The control sample (No QDs incorporated) exhibited the highest short circuit current density and it is clear that the device fill factor is being negatively impacted by incorporating quantum dots.

Table 12 shows the efficiency calculations for the different periodicity materials. In terms of both the short circuit current density and the open circuit voltage, the obtained results as consequence of the periodicity increases are as expected. However, the efficiency trend was surprising and contrary to our expectations. When the periodicity were increased from 5 QD layers to 10 QD layers, the efficiency increased from 9.2 % up to 9.9 % as expected. But, when the periodicity was increased from 10 QD layers to 20 QD layers, the efficiency dropped back to 9% which is even lower than the 5 QD layers sample. It is thus clear that the QD dots are introducing non-radiative defects in the crystal which are negatively impacting the device efficiency. It thus seems that there is no merit in introducing QD into GaAs solar cell structures. However as shown in the next section, the QD devices led to remarkable improvement in the thermal stability of the devices.

Table 12 Efficiency calculations for InAs/GaAs quantum dot materials using different vertical periodicities. The highest efficiency was exhibited for XMBE312, the sample with no QD.

Sample ID	Isc	Voc	Im	Vm	FF	h (Eff)
	mA/cm2	V	mA/cm2	V	%	
XMBE312 – No QDs	19.19	0.80	17.62	0.67	76.9	**11.8**
XMBE322 – x5	16.30	0.73	15.1	0.61	77.4	**9.2**
XMBE311 – x10	19.28	0.68	17.72	0.56	75.6	**9.9**
XMBE291 – x20	20.09	0.69	15.82	0.57	64.6	**9.0**

5.4 High Temperature dependence study

Photovoltaic devices analysis under different conditions is crucial as in real operation the environment will change according to the application. The conditions that can vary are light power, temperature, etc. Solar cells are exposed to sun irradiance which generates an increase in the operating temperature. Some applications, such as solar concentrator PV modules, operate at higher temperature than 300K (Room temperature of ~23°C). Terrestrial concentrator PV modules can operate above 315K (~40°C) [97]. For space applications, the operation temperature can go above the 400K mark depending on the mission location [98].

From the physics of the photovoltaic device, and in the case of semiconductor materials, it is evident that the temperature dependence of the recombination phenomena plays a crucial role. The latter generates losses in the generation of current with temperature changes [99], [100], [101].

The efficiency is expected to be (negatively) impacted as the temperature increases. The increase of temperature, either due to the operation environment or the light concentration, produces an enhancement of the short circuit current [102]. However, the open circuit is degraded because the temperature enhances the recombination phenomena involved as well as reducing the effective band gap of the semiconductor [103].

Many efforts have been made in the last decades to find materials with small variations in their performance at high temperatures due to increases in recombination phenomena [104]. This has led to new photovoltaic devices with higher efficiencies. Not only structural modifications have been proposed but also addition of external thermal conditions has been tested on photovoltaic devices. It has been found that both the fill factor temperature dependence and the efficiency temperature dependence are strongly related with presence of defects within the active material [105].

Recently, the introduction of quantum dots as vertical arrays in semiconductor devices has been demonstrated to have better behaviour at low temperatures than other devices [106]. However, it is important to investigate the behaviour of these devices at high

operational temperatures. For silicon photovoltaic devices, the effect of the temperature on the open circuit voltage has been shown to drop from 0.65 volts to 0.22 volts when the temperature is raised from 23 °C (RT) to 170 °C [107].

In this subsection, are presented detailed measurement of the InAs/GaAs quantum dots solar cells performance as well as the temperature dependence of the main parameters such as open circuit voltage, short circuit current density, fill factor and efficiency are presented. The study includes the analysis of the effect of the inter-dot doping profile and its temperature behaviour.

A detailed PL study in previous sections has revealed that two more energy states (1.37 and 1.2 eV) appear in the GaAs band gap which is in addition to the main 1.45eV peak. These are added due to the insertion of QDs into the host lattice. This new states add to the enhancement in the open circuit voltage which in turn helps with the increase of the device's efficiency using the correct doping profile between the dots.

5.4.1 Experiment details

Simple devices without anti-reflective coating (ARC), and which consist of 250µm cylindrical diodes, were fabricated. The top contact is formed from two concentric circles with diameter of 50µm and 200µm respectively (as refers in Figure 29). The wafers were cut into small pieces and placed on a temperature controlled base. The devices were characterized on –wafer at the Slovak University of Technology facilities in the Institute of Electronics and Photonics of Bratislava under 20 suns light illumination (AM1.5 Solar light model 16S-002-300 using a Keithley 237 I-V test equipment). A light intensity of 2000mW/cm^2 was achieved by focusing the light using a Fresnel lens. The temperature of the samples was controlled using a cryostat system.

The J-V characteristics were measured under light for all the studied samples. Without any attempt to reduce the reflectance on the solar cell surface, the short circuit current density (Jsc) for sample XMBE291, InAs/GaAs undoped QD with periodicity of 20, is 20 mA/cm^2 and its open circuit voltage is the lowest of all the samples at only 690 mV. The QDs can act as traps for the generated electrons but doping the dots increases the

probability that one electron is trapped. It is clear that the insertion of doping into the QDs reduces the recombination phenomena in the material. The highly doped sample, sample XMBE294 is clear from the figure, exhibits the highest Voc of 800 mV.

5.4.2 Room temperature characterisation

The obtained I-V curves, using 2000 mW/cm^2 light, for all the samples are shown in Figure 74.

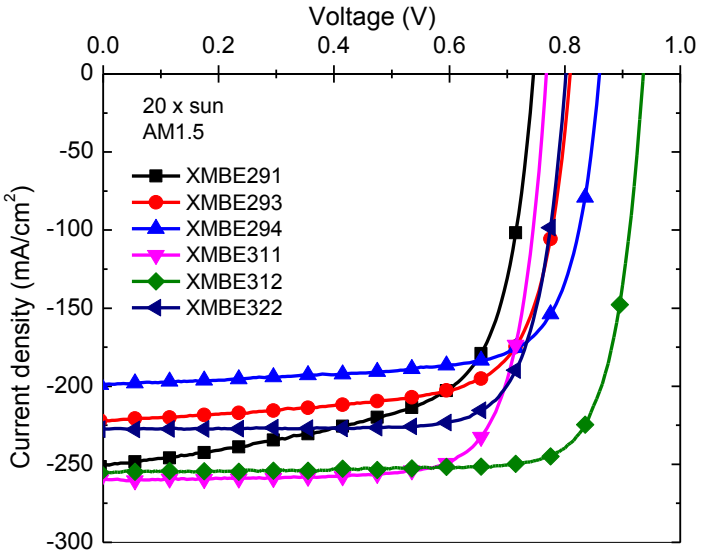

Figure 74 J-V characteristics under 20 suns at room temperature

It was found that sample XMBE291 (undoped QDs x20) exhibited the highest current density, 283 mA/cm^2. However, the enhancement of the open circuit voltage due to the inter-dot doping insertion is also clear in the graph. The QD devices efficiencies under 20 suns were extracted and the results are shown in Table 13. In the case of the highly doped sample (16x10^{10} /cm^2) the efficiency increased up to 7% and the fill factor up to 73%, which are excellent values for such simple structures. However, the undoped sample including 10 quantum dot layers, XMBE311, exhibits the highest efficiency for all the QD materials. It is evident from its JV curve, that the fill factor of the device plays a crucial role in the final device efficiency.

It is also clear that the insertion of the inter-dot doping n-type profile helps considerably the quality of the device in terms of shunt resistance. This can be seen in the curve slope from 0 volts to 0.4 volts approximately. Once again, it is confirmed that the optimum periodicity for undoped quantum dots is 10 layers. The efficiency is the highest among the rest of the QD materials. The insertion of an inter-dot doping profile evidently helps to enhance the open circuit voltage reducing the recombination in the dots. However, the short circuit is negatively impacted at room temperature.

Table 13 shows the values used for the efficiency calculations. The doped samples present a short circuit current smaller than that of the undoped sample. This is evidence that for these samples the inter dot doping is not helping the solar cell generate more free carriers. However, the doping is helping to reduce the recombination as due to the dots presence the open circuit voltage is enhanced.

Table 13 GaAs/InAs QD devices efficiencies under 20 suns

ID		x20 suns light intensity			
		Jsc	**Voc**	**FF**	**η**
		mA/cm^2	**V**	**%**	**(%)**
XMBE312	No QDs	255.0	0.94	80.3	**9.60**
XMBE322	x5 undoped	227.0	0.80	78.0	**7.10**
XMBE311	x10 undoped	260.0	0.77	76.7	**7.65**
XMBE291	x20 undoped	283.5	0.77	62.8	**6.91**
XMBE293	x20 n-doped	249.5	0.81	58.7	**5.97**
XMBE294	x20 n-doped	228.9	0.84	73.3	**7.06**

5.4.3 Temperature dependence characterisation

The devices were tested in the temperature range from 300K to 430K. For the GaAs sample XMBE312, without quantum dots, the open circuit voltage reduced by about 300 mV with the temperature increases. The short-circuit current density for the same sample is enhanced by about 2.5% at 430K, compared with the room temperature value, with values up to 261.4 mA/cm^2. The J-V curves for sample XMBE312 at different temperatures are depicted in Figure 75.

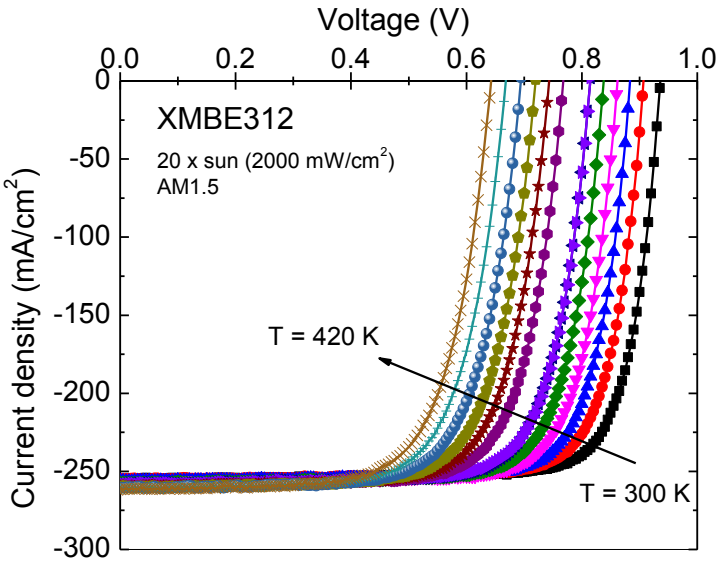

Figure 75 J-V curve measurement for temperature range from 300K to 430K for XMBE312.

For the undoped dots sample (periodicity of 20), and as expected, the open circuit voltage reduced by about 280 mV with the temperature increases. The short-circuit current density for the same sample is enhanced by about 6% at 430K, compared with the room temperature value, with values up to 266.7 mA/cm^2. The J-V curves for sample XMBE291, InAs/GaAs undoped QD with periodicity of 20, at different temperatures are depicted in Figure 76.

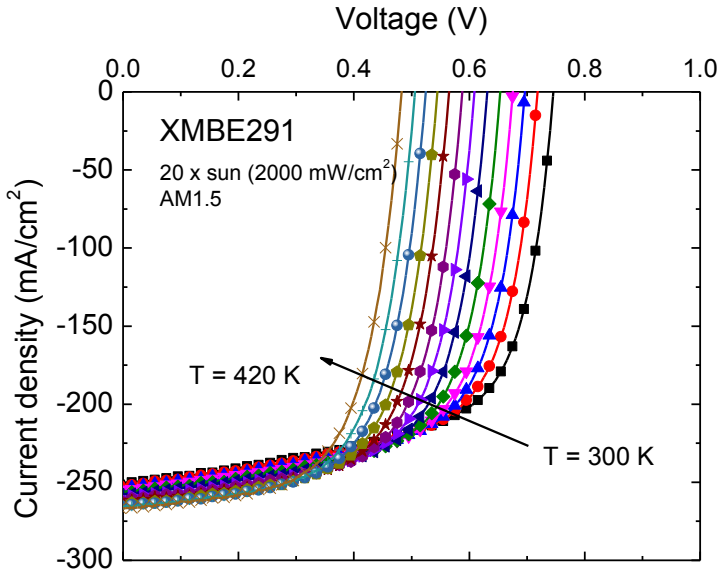

Figure 76 J-V curve measurements for temperature range from 300K to 430K for Sample 291.

For the samples with inter-dot doping, the degradation of the photovoltaic cell's electrical parameters increases with the temperature. For sample XMBE293, which an n-type doping profile of $8x10^{10}$ /cm^2, the open circuit voltage drops by just 230 mV from 0.81 volts at room temperature to 0.58 volts at 430K. The short circuit current density increases by around 9.2% with temperature as can be seen in Figure 77.

The reduction of the open circuit voltage for sample XMBE293 compared with sample XMBE291 is very noticeable. This is due to the effect of the doping profile introduced in the host lattice.

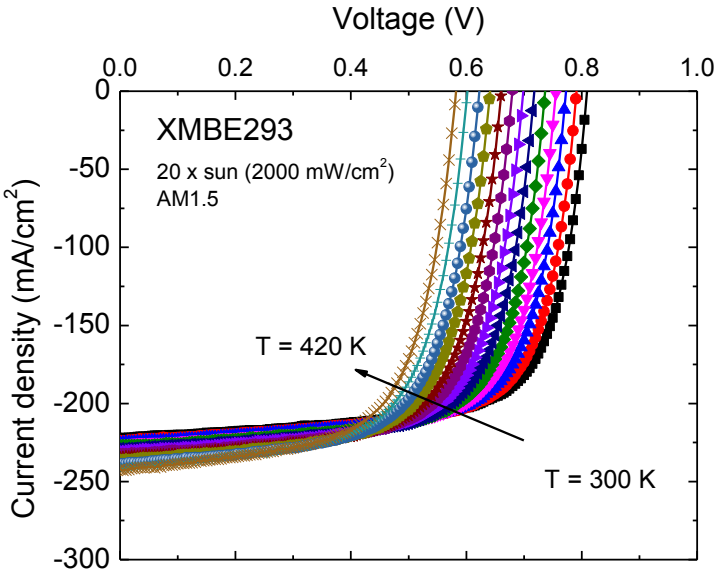

Figure 77 J-V curve measurement for temperature range from 300K to 430K for Sample 293.

For Sample XMBE294, InAs/GaAs QD with periodicity of 20 with inter-dot dopin profile of $16x10^{10}$ cm^{-3}, the open circuit voltage degradation is the smallest of all the samples. This time, the reduction of the open circuit voltage is only 250 mV. The open circuit voltage obtained at 430K is 0.61 volts. The short circuit current density increases by 11.3% rising from 200 mA/cm^2 at room temperature to 222 mA/cm^2 at 430K. (See Figure 78). It is clear that the n-type doping profile, which was introduced in the quantum dots structure, helps to reduce the recombination phenomena that limit the open circuit voltage. In this material system, the open circuit voltage drop is slower as the inter dot doping profile increases. Using inter dot doping an open circuit voltage up to 0.6 volts was achieved at 430K.

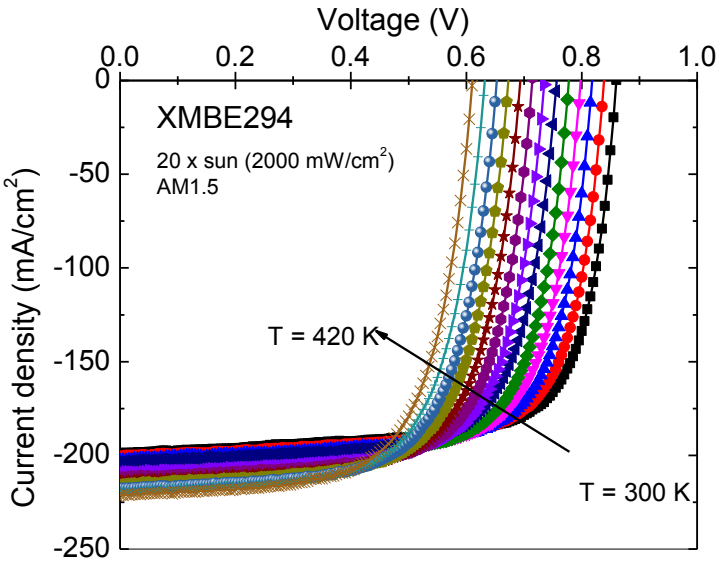

Figure 78 J-V curve measurement for temperature range from 300K to 430K for Sample 294.

For Sample XMBE322, in which the quantum dot layer periodicity was changed to 5, the open circuit voltage degradation is one of the smallest degradation of all the samples. This time, the reduction of the open circuit voltage is only 240 mV. The open circuit voltage obtained at 430K is 0.56 volts. The short circuit current density increases by 3.4% rising from 227 mA/cm^2 at room temperature to 234 mA/cm^2 at 430K. (See Figure 79).

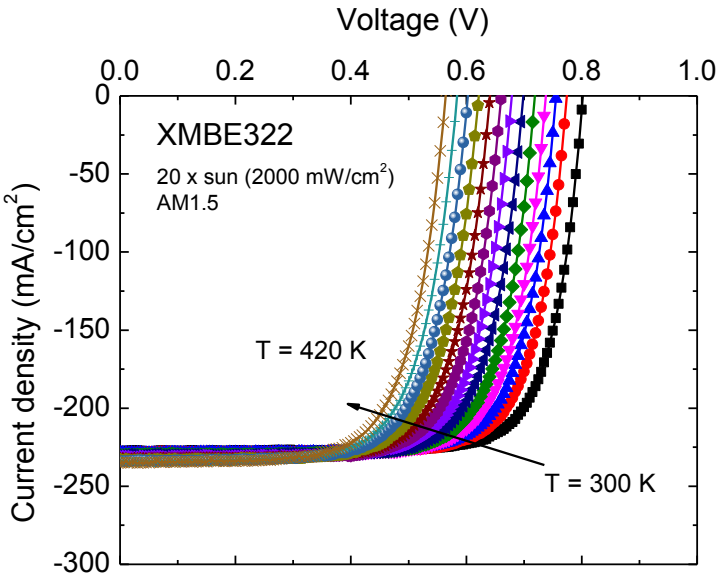

Figure 79 J-V curve measurement for temperature range from 300K to 430K for XMBE322.

The temperature dependence of the JV curve for sample XMBE311, in which the quantum dot layer periodicity is 10, is shown in Figure 80. It is clear how the increasing of the periodicity from 5 up to 10 layers has no impact in the voltage degradation and it is consistent with the idea that the adding of more quantum dot layers will only increase the quantity of active material but the material properties (like recombination processes involved) are not affected. This time, the reduction of the open circuit voltage is only 240 mV just like the 5 layers case. The open circuit voltage obtained at 430K is 0.53 volts. The short circuit current density increases by 3.3% rising from 260 mA/cm^2 at room temperature to 268 mA/cm^2 at 430K.

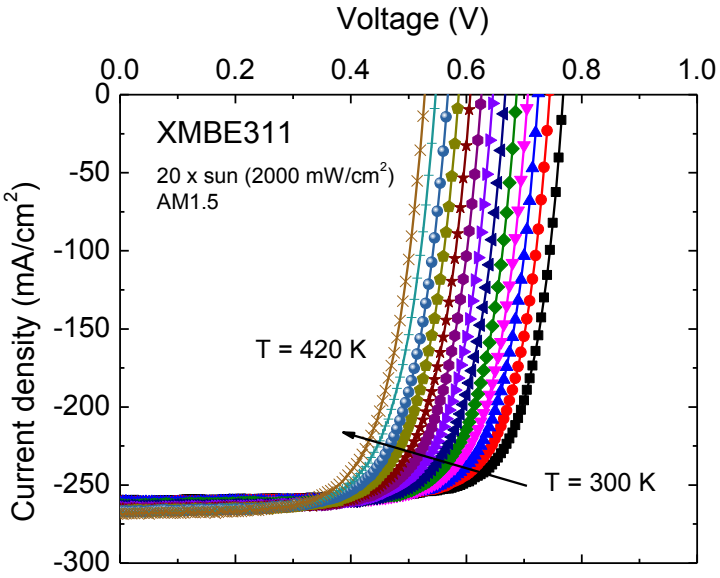

Figure 80 J-V curve measurement for temperature range from 300K to 430K for XMBE311.

The open circuit voltage temperature dependent ratios have been calculated using the J-V curve data measurements as well as the short circuit current density. The trends of these parameters as a function of temperature are shown in Figure 81 (different inter-dot doping profiles) and in Figure 82 (different quantum dot vertical layers periodicity). It is evident that the recombination processes in the material increases with the increase in temperature limiting the open circuit voltage. On the other hand, the short circuit current density is enhanced with the increase in temperature.

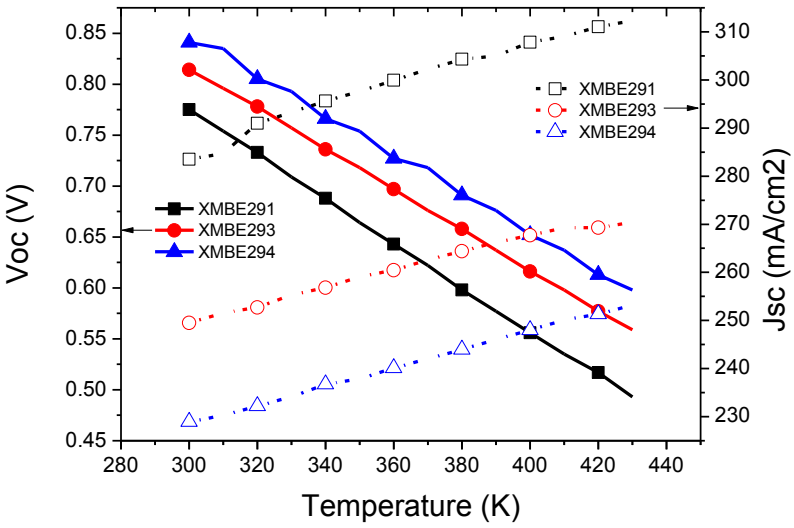

Figure 81 J-V characterisation under 20 sun for samples with different inter-dot doing profiles: XMBE291 (undoped), XMBE293 (doping profile of $8x10^{10}$ cm^{-2}) and XMBE294 (doping profile of $16x10^{10}$ cm^{-2}).

For different periodicities, it is evident that the recombination processes in the material does not change significantly. On the other hand, the short circuit current density is enhanced with the temperature increases but still below that of doped samples ratios.

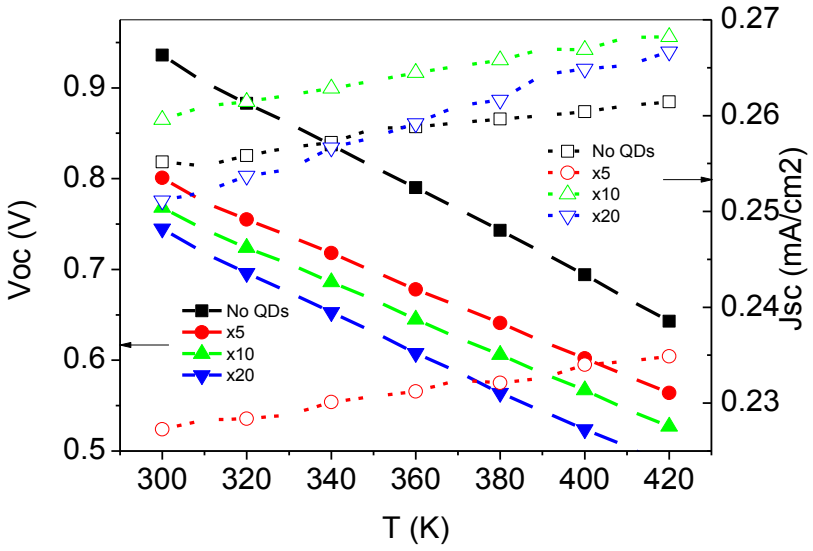

Figure 82 J-V characterisation under 20 suns for samples with different vertical periodicities: XMBE312 (No QDs), XMBE322 (x5), XMBE311 (x10) and XMBE291 (x20).

The temperature increase degrades the photovoltaic device performance. The open circuit voltage is negatively affected by the temperature. The rates of change are shown in Table 14.

It is clear that the doped quantum dots samples, Samples XMBE293 and XMBE294, present the lowest coefficient of -1.9 mV/K, while -2.25 mV/K is obtained for the undoped quantum dots sample with periodicity of 20. These values are competitive with the best values for organic solar cells found to be in -1 mV/K for bulk heterojunction (BHJ) material [108] and -1.9mV/K in [109]. Furthermore, the short circuit current changes in different ratios. For the doped dots, the ratios are higher than the ones for the undoped dots. Even when small changes have been observed for XMBE322, XMBE311 and XMBE12, the periodicity temperature dependence seems to be nil. However, when the periodicity is increased up to 20 layers, the quantity of material is enough to have temperature dependence effects.

Table 14 Temperature dependence for Voc and Isc

ID	d(Voc)/dT mV/°K	d(Isc)/dT mA/cm^2/°K
XMBE291	-2.25	0.12
XMBE293	-1.91	0.16
XMBE294	-2.01	0.18
XMBE311	-2.00	0.07
XMBE312	-2.50	0.05
XMBE322	-2.00	0.06

The efficiency of the photovoltaic device like the ones presented in this work are strongly dependent on the material characteristics and the contacts (metallization) used. The later gives an efficiency dependence of the open-circuit voltage and the short-circuit current density. These parameters directly affect the Fill Factor of the cell, an important device quality reference. Fill factors close to 100% are desirable, but in real devices, values above 70% are acceptable. Therefore, as the fill factor is function of the Voc and Jsc parameters, the efficiency of the devices will be markedly impacted by the temperature variations.

In Figure 83 are depicted the temperature dependence curves for the fill factor and efficiency for samples XMBE291, XMBE293 and XMBE294. For the undoped sample with periodicity of 20, the fill factor remains fairly constant with temperature increases. However, for the doped samples the fill factor does drop with temperature.

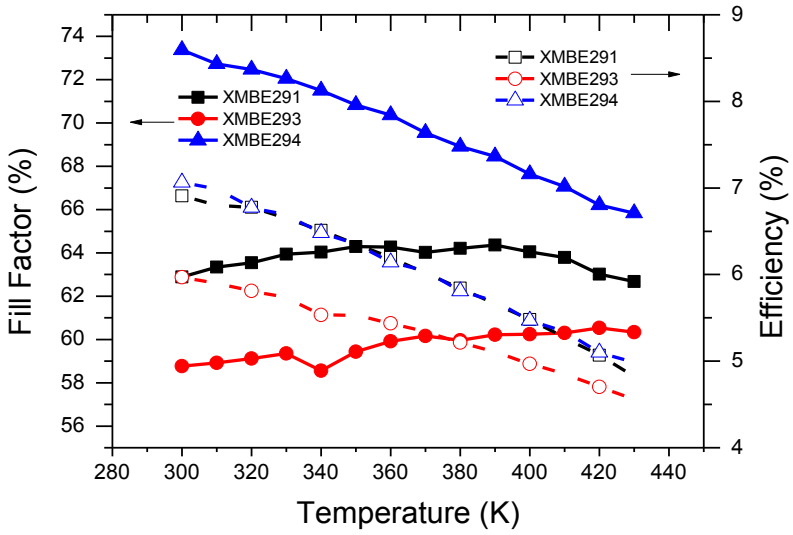

Figure 83 Fill Factor and Efficiency temperature dependence measurements for samples with different inter-dot doping profile

The efficiency for all the devices is impacted negatively with an increase in temperature as expected. The best efficiency temperature dependence coefficient ($d(\eta)/dT$) is displayed by Sample XMBE293, inter-dot doping profile of $8x10^{10}$ cm^{-2}, which has a coefficient of -0.0106 %/°K. This implies that the efficiency, as a function of temperature, of Sample XMBE293 drops at a lower rate than Samples XMBE291, undoped dots, and XMBE294 , inter-dot doping profile of $16x10^{10}$ cm^{-2}, even with the fact that the open circuit voltage drop is faster than in the highly doped dots sample. There is thus a clear compromise to be struck between open circuit voltage and short circuit current density variations.

In Figure 84 are depicted the temperature dependence curves for the fill factor and efficiency for samples XMBE312 (No QDs within the lattice), XMBE322 (x5 QD layers), XMBE311 (x10 QD layers) and XMBE291 (x20 QD layers. For the undoped sample with periodicity of 20, XMBE291, the fill factor remains fairly constant with increases in temperature. However, for the doped samples the fill factor does drop with temperature. At high temperatures, the samples with few QD layers (vertically stacked) exhibited the worst degradation effect compared with the doped samples. However, when the number of quantum dot layers was 20, the efficiency degradation as a function of temperature was around 50% less compared with samples with smaller number of quantum dot layers.

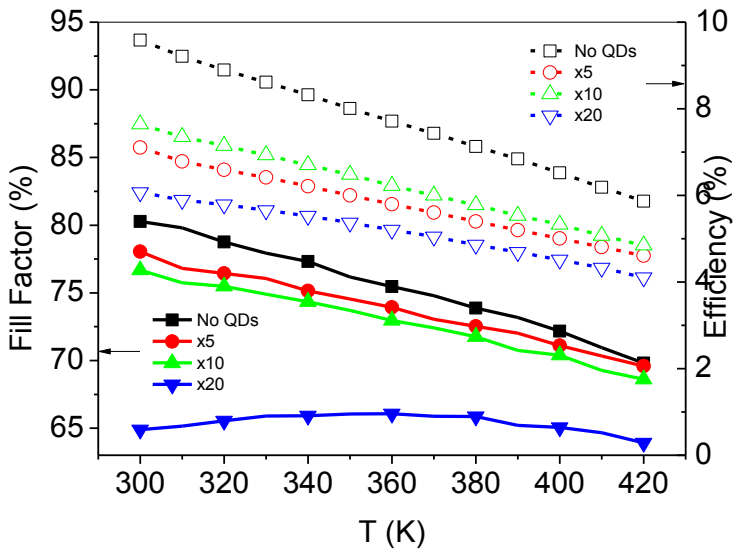

Figure 84 Fill Factor and Efficiency temperature dependence measurements for samples with different QD vertical periodicity

In Table 15 are presented the fill factor and the efficiency coefficients as temperature dependence parameters for all samples. The Fill factor as function of temperature drops at a lower rate for sample XMBE294, which has 20 QD layers with an inter-dot doping profile of $16x10^{10}$ cm^{-2}, and as a consequence this sample exhibits the lowest efficiency temperature dependence rate of -0.015 %/K. These values of fill factor temperature dependence are excellent compared with the values of -0.64%/K that have been found for Si devices [110]. For commercial crystalline Si solar cells, fill factor coefficient drops at a rate of -0.2 %/K and the efficiency at a rate of -0.53 %/K [111]. This strong efficiency temperature dependence degradation makes them less than appropriate candidates for high power concentrator applications.

Table 15 Efficiency temperature dependence for QD materials

ID	d(η)/dT %/°K
XMBE291	0.016
XMBE293	0.016
XMBE294	0.015
XMBE311	0.023
XMBE312	0.030
XMBE322	0.021

Additionally, the minimum energy required to generate free electron in the material has been calculated and the results are shown in Table 16. It can be seen that the introduction

of quantum dots reduce the GaAs activation energy independently of their studied configurations, which were either with different periodicities or including different inter-dot doping profiles.

Table 16 Activation energy obtained from Voc vs. T for all InAs/GaAs QD material system

Sample ID	Activation Energy eV
XMBE291	1.39
XMBE293	1.38
XMBE294	1.48
XMBE311	1.36
XMBE312	1.65
XMBE322	1.38

5.4.4 Discussion

In summary, detailed investigations of three InAs/GaAs QD samples with different doping profile and tested under 20 suns irradiation in the temperature range from 300 to 430 ºK are reported. The solar cell efficiency was found to be temperature dependent. The efficiency is reduced as the operational temperature is increased. The obtained results indicate an improvement of the GaAs solar cells operation at higher temperatures due to the insertion of QDs. The open circuit voltage temperature dependence value of -1.9 mV/K is an excellent value compared with the one obtained on GaAs solar cells of -2 mV/K reported in [98]. In addition, it was found that with the introduction of n-type dopants into the quantum dots lattice, the temperature dependence of the open circuit voltage is weaker compared with undoped quantum dots structures.

5.5 Low temperature dependence study

The analysis of photovoltaic (PV) devices operating under high temperatures conditions is very important to fully characterize and understand cell behaviours. Also, it is sometimes necessary to analyse the solar cell performance under low temperatures operation in order to understand the physics that controls the device behaviour. The temperature dependence of some of the material parameters, such as the recombination

phenomena, plays a crucial role. The latter involves unavoidable losses of current with temperature changes [112], [113], [114]. Carrier mobility changes due to two main scattering phenomena which are the impurities and lattice vibration. These phenomena are very temperature dependent too. The lattice vibrations reduce at low temperatures while the impurities scattering will be impacted by the ionization at very low temperatures, usually below 100K. Within the range of 100 K to 400K, usually denoted as the extrinsic region, a temperature increase will not generate more free carriers because here all the dopants are already ionized. At higher temperatures than 400K (for Si) charge carriers will be generated by lattice vibrations and the number of intrinsic carriers will dominate.

Furthermore, the carrier kinetic energy is reduced by reducing the temperature and this has the effect of further reducing the photocurrent via drift and diffusion current components. Low temperatures produce a reduction of the diffusion current, however, at high electric fields the drift current dominates while at low electric fields the diffusion current dominates [115].

The introduction of quantum dots arrays in PV devices is expected to be as a good option to get better behaviour at low temperatures [116]. This devices concept is known as intermediate band solar cells and we have shown in our previous studies that the resulting devices are very stable at temperatures higher than 300K. In this study we demonstrate that the insertion of n-type inter-dot dopants helps to improve the fill factor of the device while the temperature dependence degradation of the cell parameters is reduced. A number of QD solar cells based on the $In_{0.5}Ga_{0.5}As/GaAs$ system have been previously tested at low temperature showing blue shifting of the energy gap material and extended wavelength range but at a cost of a highly reduced fill factor at temperatures lower than 150K. [117] It has also been shown that GaAs cells showed lower dark current compared with the quantum dot ones at low temperatures [118]. In addition, it has also been found that low temperature measurements on doped material revealed that there is a very strong relationship between the carrier concentration and the quantum efficiency. The quantum efficiency at low temperatures is dominated by the junction carrier concentration and not by the minority carrier diffusion length [119].

In this section XMBE312 (control sample), XMBE291, XMBE293, XMBE294, XMBE 311 and XMBE322, which are GaAs/InAs quantum dots (QDs) structures grown on GaAs substrate, were measured and characterized at low temperatures to study the physics of this intermediate band cell. The results were compared with a control GaAs sample without any quantum dot included. The samples structures consist of two different batches. The first one of 20-period quantum dots arrays vertically stacked with the inter-dot doping profile as the main differentiator. The second one of different periodicities of the quantum dot vertical layers (periodicities of 0, 5, 10 and 20). Temperature dependence of the photocurrent spectra is studied in details and this includes the analysis of the effect of the inter-dot doping profile and its temperature behaviour.

5.5.1 Experimental details

Samples were diced into small pieces and were placed on a temperature controlled chuck base. The I-V measurements were performed using a Keithley 237 unit. The measurements of light I-V curves was carried out under 1 sun AM1.5 solar simulator from the company Solar Light, model 16S-002-300 (light intensity 100mW/cm^2). A Fresnel lens assembly was used to obtain 20 suns light intensity (2000 mW/cm^2). The temperature of the samples was controlled using a cryostat system. The measurements setup is shown in Figure 85 and was conducted at the Slovak University of Technology facilities in the Institute of Electronics and Photonics of Bratislava.

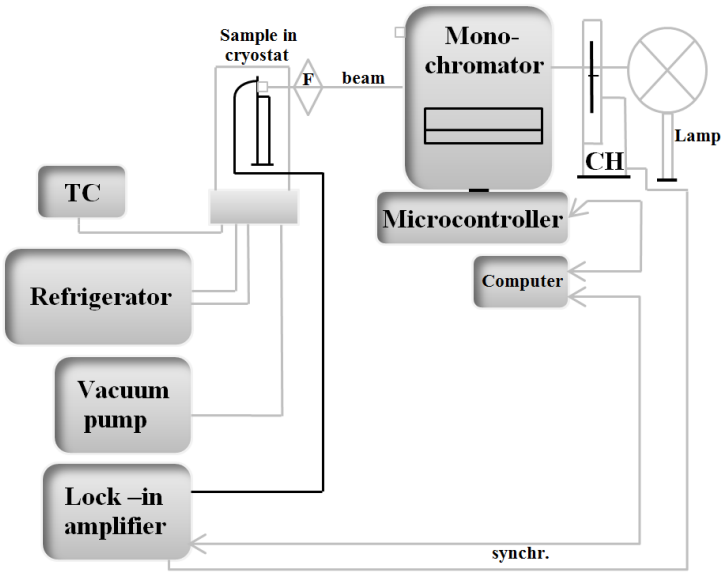

Figure 85 Low-temperature photocurrent measurements setup

5.5.2 Temperature dependence characterisation

The electrical characterization at room temperature under light conditions shows an evident open circuit voltage enhancement due to the inter-dot doping profile. However, we have shown in Section 5.4 that at high temperatures the quantum dot devices showed a better stability and the solar cell metrics are impacted much less than the ones for the control GaAs samples [120]. In order to understand the physics involved in the quantum dots device performance, low temperature measurements were performed. These measurements were made within the range from 50K to 300K and photocurrent data were obtained. For the control sample, photoresponse from the GaAs bandgap (1.44eV) 860 nm down to 400 nm were acquired. The photocurrent spectra at 300K are shown in Figure 86.

The GaAs bandgap is shifted from 860 nm (1.44 eV) at room temperature to 815nm (1.52 eV) at 50K. This is consistent with the temperature dependence of the Gallium Arsenide bandgap via the Varshni's equation [121] confirming that the bandgap of GaAs is dependent only on the lattice dynamics due to the temperature drop that leads to a shifting of both valence and conduction bands. It can be seen that the photocurrent within the wavelength range from 400 to 830 nm has a bizarre behaviour. It was expected that the photocurrent were reduce as temperature reduces but at 50 K, the photocurrent has a clear increasing. However, the absorption range was shifted normally so, more studies should be perform to find the reason of this strange behaviour.

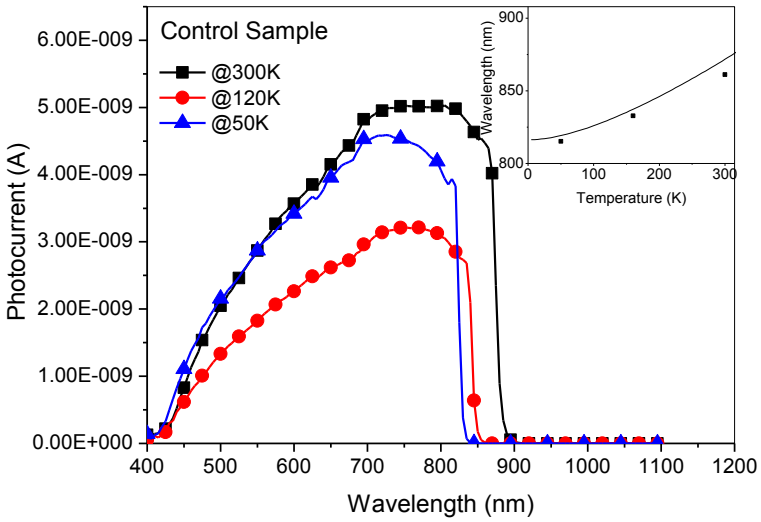

Figure 86 Photocurrent for GaAs Control Sample. The GaAs bandgap presents a blue-shift while the temperature drops as expected. Inset Varshni equation is compared with low temperature measurement values showing a good agreement

When nanostructures are introduced within the lattice, more phenomena are involved in the temperature dependence relation. As can be seen in Figure 87 for the undoped InAs/GaAs quantum dots sample, a new energy level appears at 922 nm approximately (1.35 eV) which increases the absorption wavelength of the material into the infrared spectrum. As is well known, at very low temperatures (< ~ 70K) the electron mobility and the lattice vibrations are significantly reduced. Not only are these parameters affected by temperature but also the drift and diffusion current.

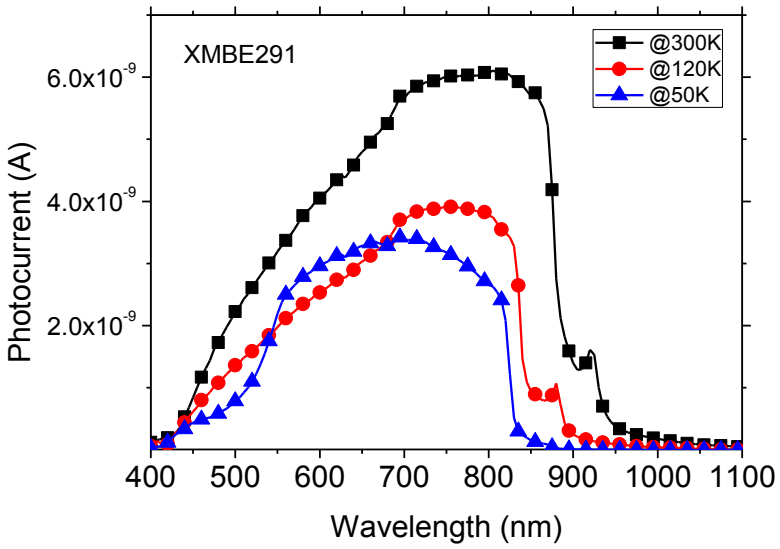

Figure 87 Photocurrent for Sample XMBE291, InAs/GaAs undoped quantum dot, the GaAs bandgap presents a blue-shifted while the temperature drops as expected.

Low-temperature measurements were therefore performed on all the quantum dot samples with different inter-dot doping profiles. Sample XMBE291, undoped dots, shows additional optical transitions at room temperature which are located below the GaAs bandgap. The first additional transition is located at 922 nm (1.34 eV) (first quantum dot transition (QD1)). The second quantum dot transition (QD2), which is even lower than QD1, appears at 1.08 um (1.23 eV). These new optical transitions can be observed in Figure 88.

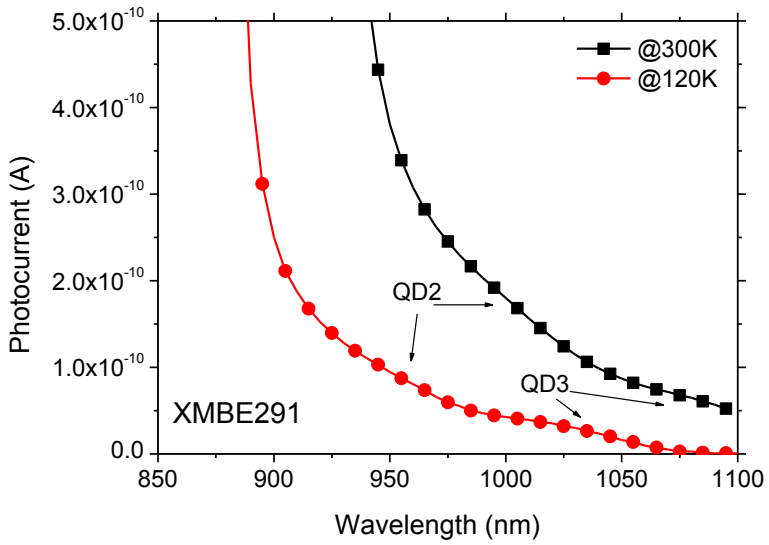

Figure 88 Photocurrent for Sample XMBE291 showing two extra optical transitions located at 1 µm and 1.1 µm (QD2 and QD3 transitions).

Figure 89 depicts the low temperature measurements for sample XMBE293 from 50K to 300K. The intensity of the QD1 and QD2 optical transitions (920nm and 1080 nm) are reduced with temperature as expected. All optical transitions show, as in the GaAs control sample, a blue shift. For samples XMBE293 and XMBE294, $8x10^{10}$ /cm^2 and $16x10^{10}$ /cm^2 n-type inter-dot doping profile respectively, the same transitions are present at 920 nm approximately. However, this time the QD2 transition is not present.

It is evident that a reduction of the photocurrent below 610 nm approximately occurs at room temperature. This is probably a consequence of the photon absorption in the $Al_{0.6}Ga_{0.4}As$ window layer.

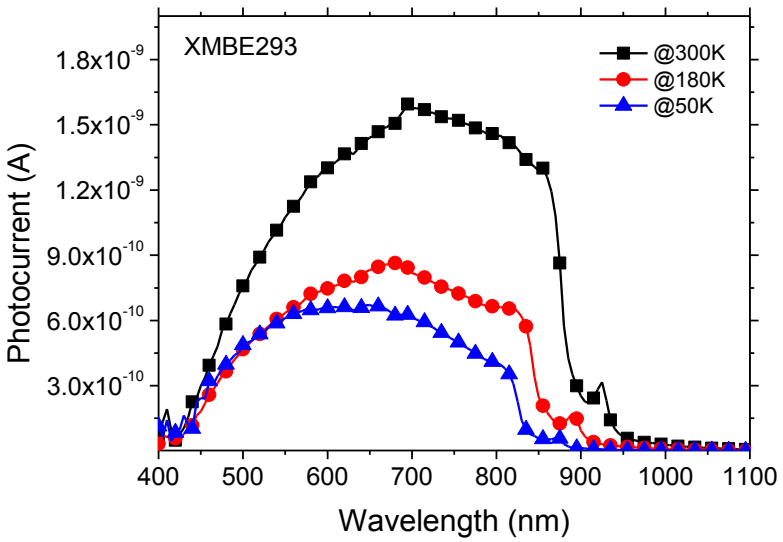

Figure 89 Photocurrent for Sample XMBE293, InAs/GaAs with n-type inter-dot doping profile of $8x10^{10}/cm^2$.

When a doping profile is introduced within the dots, the open circuit voltage is enhanced due to the reduction of recombination in the nanostructures but the short circuit current is expected to be impacted negatively. In sample XMBE293, which includes an n-type doping profile of $8x10^{10}$ /cm^2, the QD1 transition is again visible at 920nm at room temperature shifted down to 870nm at 50K. At room temperature and due to the inter-dot doping profile, the photocurrent decreases from a maximum of $6x10^{-9}$A at 700nm to $1.6x10^{-9}$A at 700nm.

Sample XMBE294 showed a reduction in the intensity of the photocurrent when the temperature is reduced, as the rest of the samples as can be seen in Figure 90. This time, the inter-dot doping profile is even higher than the one for sample XMBE293. However, bellow 610 nm, the photocurrent spectrum showed an increase at 160K which possibly occurs because of the changes in the window layer due to the reduction in the temperature reducing its absorption coefficient and as a consequence allowing through more photons to pass to the active region (the quantum dots array) and thus contributing to the carriers generation.

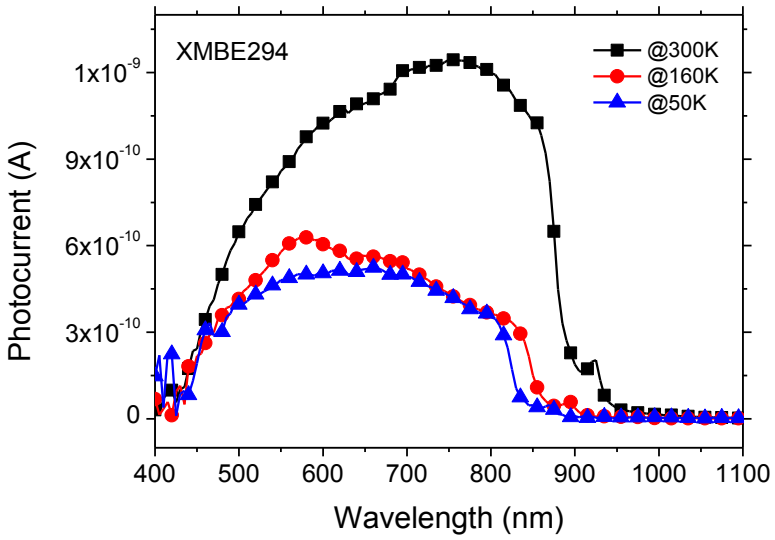

Figure 90 Photocurrent for Sample C, InAs/GaAs with n-type inter-dot doping profile of $16x10^{10}/cm^2$.

Sample XMBE322 showed a reduction in the intensity of the photocurrent when the temperature is reduced, as the rest of the samples as can be seen in Figure 91. This time, the reduction of the quantum dot layers periodicity down to 5 produces a reduction of the photocurrent in the QD1 transitions. The photocurrent temperature dependence for this sample has a lineal relationship with temperature. The effect of the emitter layer below 680 nm is apparent where it starts absorbing part of the photons reducing the photocurrent levels.

Sample XMBE311 showed a reduction in the intensity of the photocurrent when the temperature is reduced as can be seen in Figure 92. This time, the 10 quantum dot layers produce a slight increase of the photocurrent in the QD1 transition. The photocurrent temperature dependence for this sample has a lineal relationship with temperature. Again, it is clear that the emitter layer starts absorbing below 680 nm reducing the photocurrent levels.

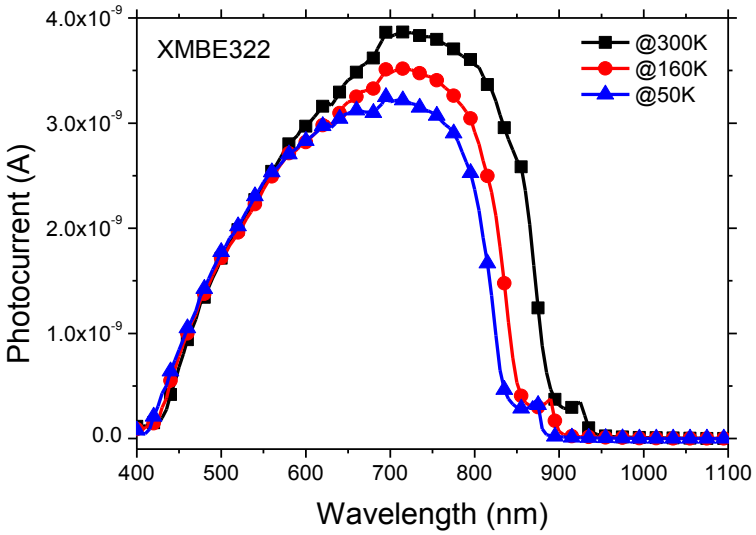

Figure 91 Photocurrent for Sample XMBE322, with 5 InAs/GaAs quantum dot layers.

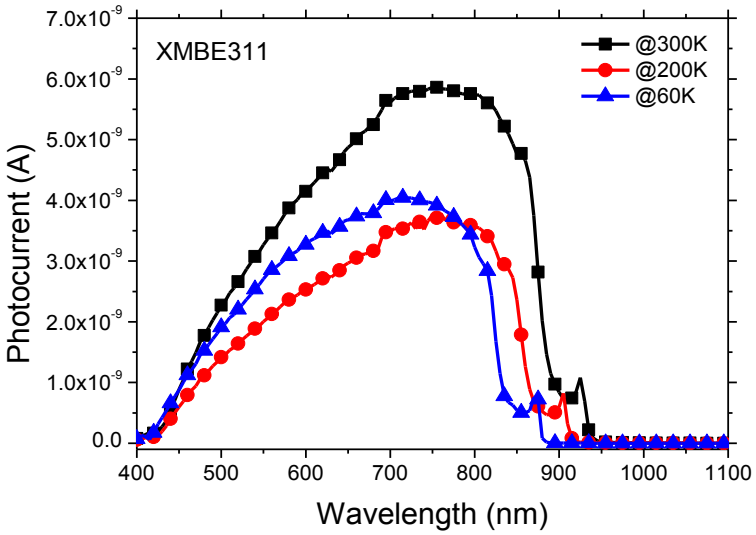

Figure 92 Photocurrent for Sample XMBE311, with 10 InAs/GaAs quantum dot layers.

The QD1 optical transitions as a function of the temperature are presented in Figure 93 for all the QD studied materials. It can be seen that the intensity of the photocurrent at the first quantum dot optical transition varies according to the material configuration. For inter-dot doped quantum dot materials, the dopant atoms clearly contribute to a drastic reduction of the photocurrent as the temperature drops. This can be interpreted as the intermediate band requiring thermal energy to be enabled in the material but when impurity atoms are present in the quantum dot, the host lattice can enhance the current generation due to the high carrier concentration. However, for the undoped samples, the

photocurrent seems to remain at the same level independently of the temperature changes. Here, the effect is almost imperceptible because the photocurrent at room temperature is already very low by itself.

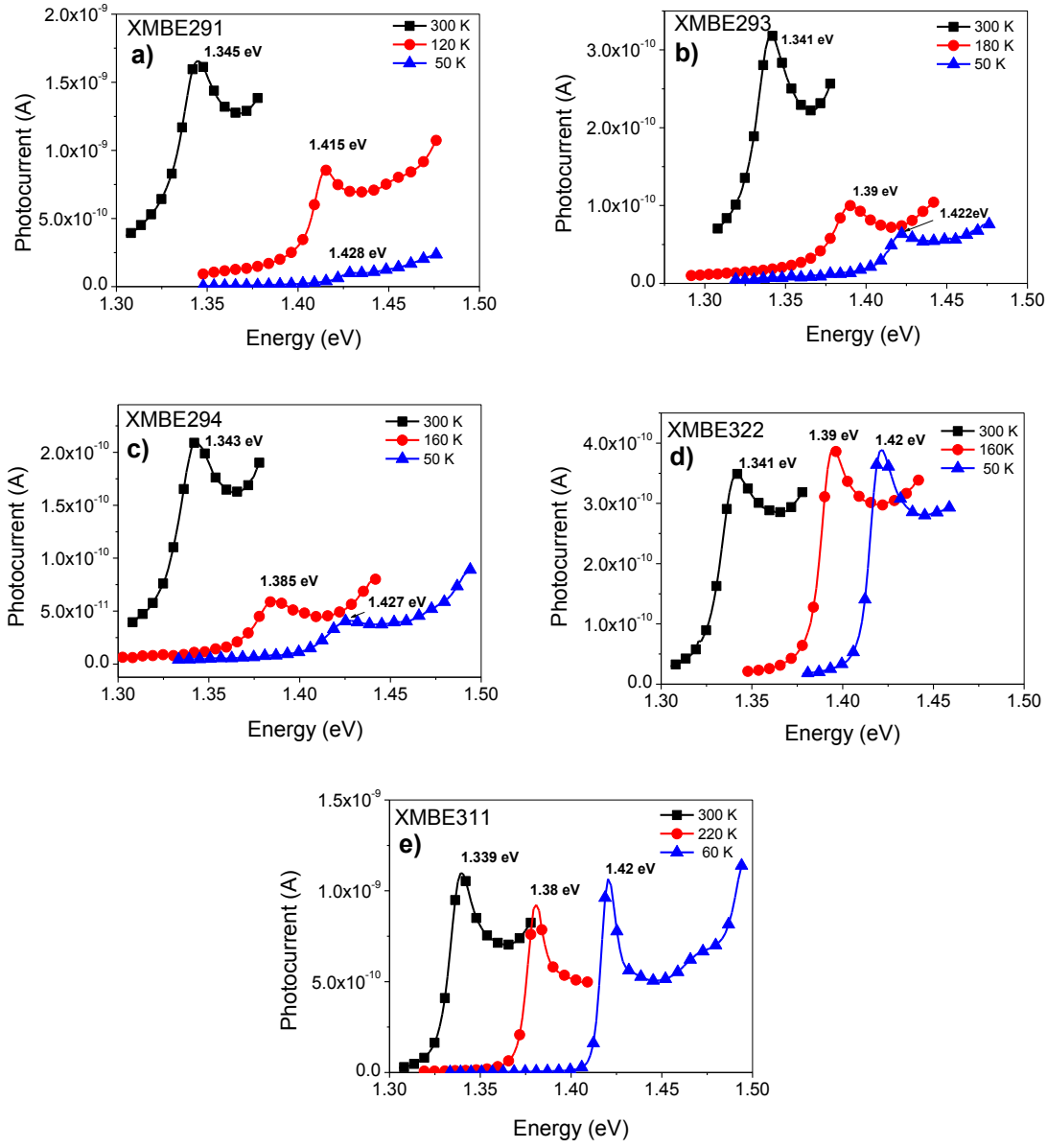

Figure 93 QD transitions as function of the temperature within the range from 50K to 300K

Figure 94, shows polynomial approximations of the QD1 for the different samples including the GaAs Control sample. Using Varshni equation, the GaAs fitting was obtained using Eg(0)= 1.519 eV with alpha = 5.41×10^{-4}eV and beta = 204K. In order to fit the QD1 transition for all studied samples, the same values were used except for Eg(0) which was changed to 1.44 eV. Thus, it can be seen that the QD1 transition is blue-shifted when the temperature is reduced. In addition, the peaks intensity is dramatically reduced. It means that intermediate band cannot be formed in the absence of thermal energy. It is

evident that the doping within the dots can interact with the charge carriers generation at temperatures greater than 100K where the impurities are ionized.

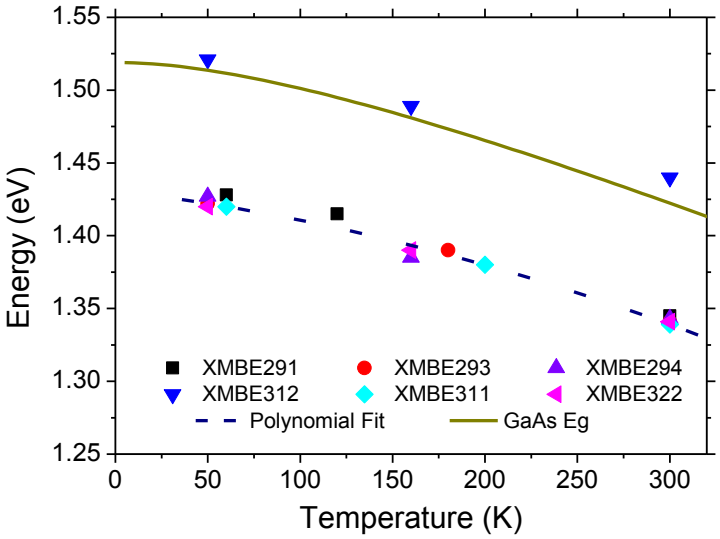

Figure 94 Low-temperature measurements for InAs/GaAs QD samples and Control including the theoretical GaAs Eg curve and the polynomial approximation for samples measurements data.

Several QD PV devices were measured at low temperatures. The quantum confinement effects at temperatures within the range of 50K to 300K were studied by observing the temperature dependence of the photocurrent spectra. It was observed that lower energy transitions, below the GaAs material bandgap, are added by introducing QD arrays within the lattice. These QD structures, are negatively impacted at low temperatures which confirms that thermalisation of the lattice is needed to keep the intermediate band transitions. In all the devices, the window layer starts absorbing some of the incident photons hindering photons from contributing to the active layers.

5.6 Anti-Reflective coating study

This section presents the characterisation of several solar cell devices using a single layer of anti-reflective coating (ARC). Several devices, consisting of InAs/GaAs quantum dots cylindrical diodes, were fabricated and characterised. The main difference between the used materials is the inter-dot doping profile. The J-V characteristic for the devices were obtained under 1 sun showing an increase of the short circuit current density (Jsc) by almost 40% in the undoped dots sample. We show that the use of 100 nm Silicon Nitride

(Si_3N_4) enhance the efficiency by about another 2.5% resulting in efficiencies up to 11.6% for single junction diodes.

Reducing the reflected incident light on the top of optical devices (solar cells, lasers, photo diodes, etc.) can increase the efficiency of these devices when using different coatings such as ZnS and MgF_2 [122]. The design of the antireflective coating (ARC) can be complicated because correct and accurate optical data of materials are needed to evaluate the multilayer coefficients which are a function of the wavelength of the incident light. Several methods can be used to calculate a single layer ARC for a single wavelength which can be analytical or empirical. The ARC can be used for a single layer, for different wavelength or wideband detectors. For the case of solar cells, it is clear that what is needed is a wideband anti-reflective coating because of the large wavelength range of incident light. The material used can be organic such as TiO_2 (Spray), Ta_2O_5, ZnS and SiO_2 [123].

As is well known, the reflectance on the surface of solar cells is related directly to the refractive index of the media layer thickness. Thus, thickness and refractive index are critical for the optimal ARC coating and enhancement of up to 30% in the Isc using a 68nm single layer of ZnS on silicon solar cell have been reported [124]. TiO_2 and Al_2O_3 coatings have been tested on GaAs devices, leading to improvements in the Jsc of up to 30% [125]. TiO_2 has been used to enhance the performance of different solar cells like Dye-sensitized solar cells (DSSC) resulting in an efficiency up to 3.4% from almost 2% of the original cell [126] but for this ARC the temperature and thickness are critical parameters [127]. Deposition of Silicon Nitride as ARC has been tested on several devices showing good enhancements of the optical coupling. In this section, the deposition of 100nm Si_3N_4 single layer on InAs/GaAs Quantum Dots solar cells is studied.

5.6.1 Antireflective coating design

An anti-reflective coating (ARC) should be designed to operate with low reflectance in the long wavelength range (from 800 to 1000 nm). The first step is to measure the reflectance of the material and this is shown in Figure 95 as a black-line. It can be seen

that only 40 % of the incident light on the device is transmitted to the GaAs top layers. So, 60 % of the energy is being lost due to the media mismatch.

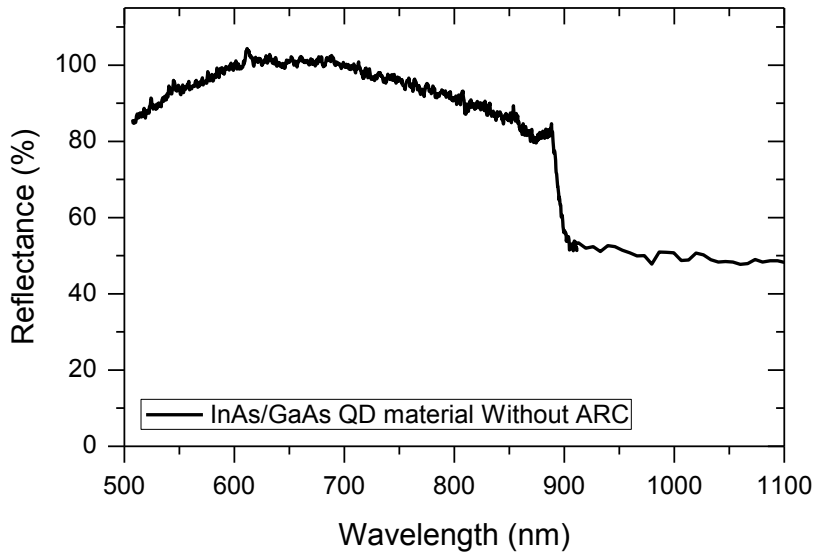

Figure 95 Reflectance measurement for InAs/GaAs material

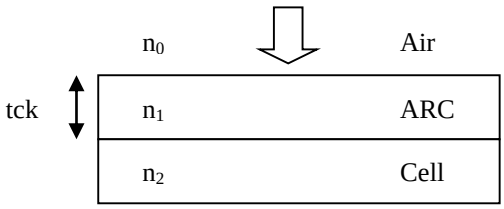

Figure 96 Scheme of optical parameters of incident light

The reflectivity can be calculated using the diagram shown in Figure 96. The reflectance equation is:

$$R = |r|^2 = \frac{r_1^2 + r_2^2 + 2r_1 r_2 \cos 2\theta}{1 + r_1 r_2 + 2r_1 r_2 \cos 2\theta} \quad \mathbf{5}$$

Where r_1, r_2 and θ are calculated as follow:

$$r_1 = (n_0 - n_1) / (n_0 + n_1) \quad \mathbf{6}$$

$$r_2 = (n_1 - n_2) / (n_1 + n_2) \quad \mathbf{7}$$

$$\theta=(2\pi n_1 t_1) / (\lambda) \qquad \mathbf{8}$$

Equations 5, 6, 7 and 8 were used to calculate the antireflective coating refractive index and the optimum thickness [128].

Antireflective coating refractive index calculation

The reflectance can be calculated as a function of the refractive index of the different media and the thickness of the intermediate layer (in our case it is the ARC layer) as shown in Figure 97. n_0 is considered as 'air', and n_2 as 'GaAs'. Thus, the ARC design is focused on its refractive index and its thickness.

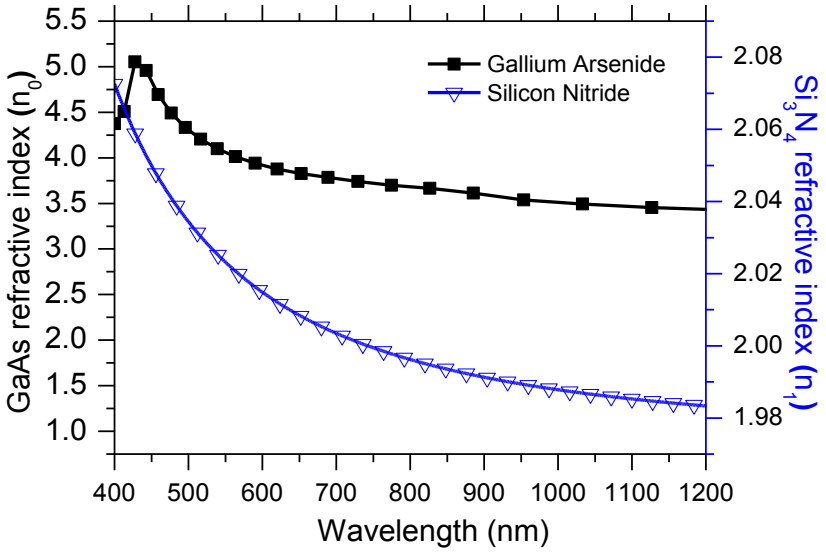

Figure 97 GaAs [129] and Si_3N_4 [130] refractive index

The refractive index n_0 is fixed to be 1 (air) as the solar cell is exposed to ambient. The n_2, GaAs refractive index (shown in Figure 97), is obtained from [129]. The thickness used for the optimum ARC refractive index is 70 nm. It is clear that the minimum reflectance value is obtained using an ARC refractive index of 2 (Figure 98) with the minimum reflectance of 2% at 550 nm. The later, makes Si_3N_4 the best option for this materials. Si_3N_4 has a refractive index of 2 from 700 to 1100 nm as shown in Figure 97.

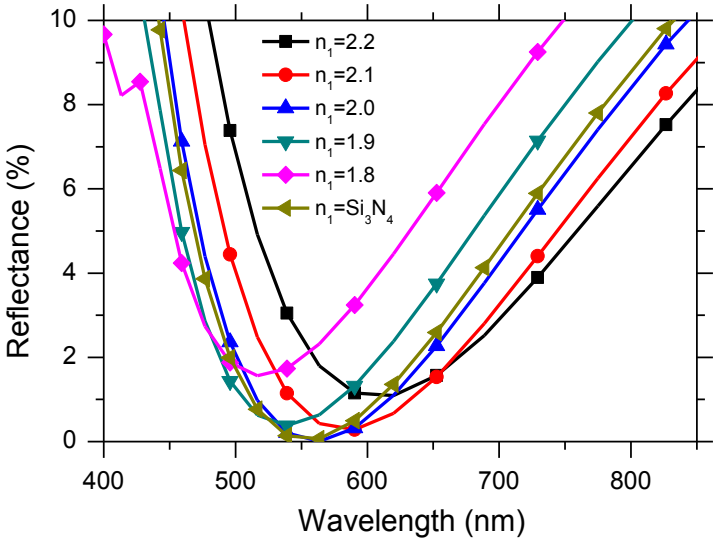

Figure 98 ARC Refractive index calculation with $n_0=n_{air}$, $n_2=n_{GaAs}$ and tck=70nm

Antireflective coating thickness calculation

Si_3N_4 has therefore a convenient refractive index to reduce the reflectance up to 2%. It is necessary to tune the antireflective coating to the region of interest in the infrared wavelength range from 700 to 1100nm. Controlling the layer thickness can tune the wavelength optical response of the ARC [131], [132]. Thus, the optimum thickness is calculated using $n_0=n_{air}$, $n_1=n_{Si3N4}$ and $n_2=n_{GaAs}$. The thickness was varied between 60 nm to 120 nm as can be seen in Figure 99 where 100 nm gives the best reflectance behaviour from 700 to 1100 nm. The reflectance is 2%.

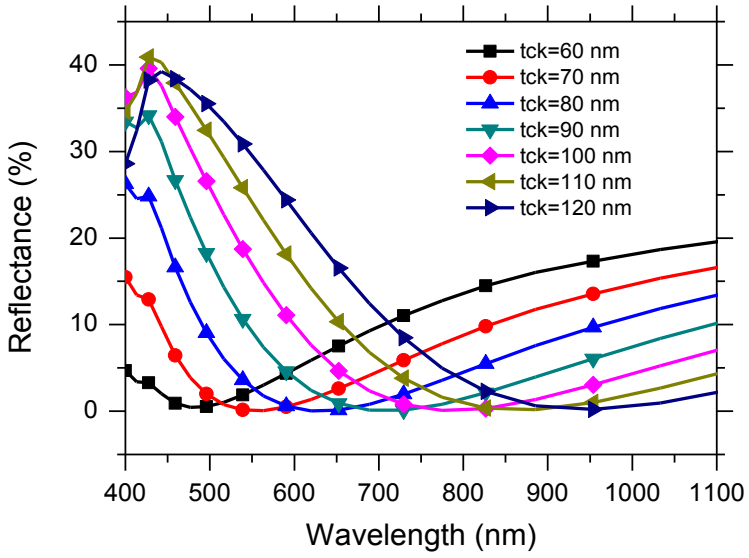

Figure 99 Si_3N_4 layer thickness calculation with $n_0=n_{air}$, $n_1=n_{Si3N4}$ and $n_2=n_{GaAs}$

5.6.2 Optical measurements

Samples preparation

The samples were coated with 100 nm Si_3N_4 layer using Plasma Enhance Chemical Vapour Deposition (PECVD) at 165°C at 10 nm/min. The deposition was performed under 360mT pressure and a gas of Silanol/Amonia/Nitrogen flow ratio of 9/20/56 sccm. The coated layer shows a bluish colour that corresponds to approximately 93.5 nm according to the Si_3N_4 thickness colour chart [133]. The actual thickness was checked using a Dektak™ surface profiler and found to be 102 nm.

Reflectance measurement

The reflectance measurements were performed using the setup shown in Figure 100. The source used is a tungsten halogen broadband Ocenoptics LS1™ guided by an optical fiber. The optical fiber is a Reflection/Backscattering probe.

The detectors used were an extended InGaAs (900 to 2500 nm) and a Si CCD array (400 to 1100 nm). In order to get a reliable measurement, the system was calibrated using a reference that reflects 100 % of the incident light. Calibrated mirrors are preferably used as reference. For these measurements, a double side polished GaAs sample, that gives a reflectance of 100 %, was used. The reflectance measurements are shown in Figure 101.

The reflectance after the ARC insertion is around 2% at 800 nm wavelength, as expected. This is a very good reflectivity reduction at the surface of the solar cell. The reflectance from 700 up to 1100 nm is kept well below 20 %. This implies that the amount of photons into this wavelength range has been doubled.

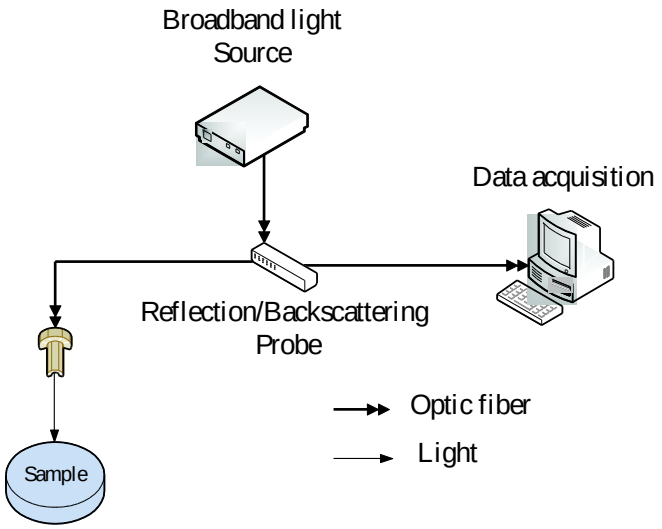

Figure 100 Reflectance measurement setup

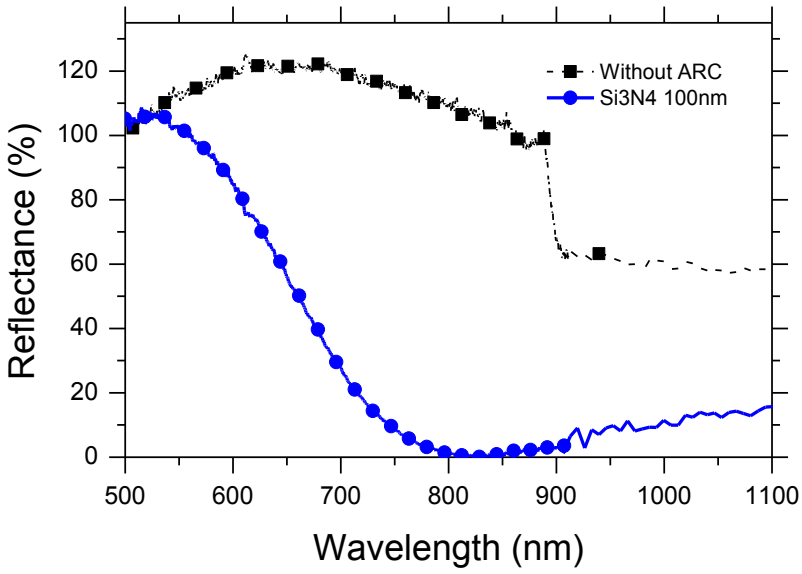

Figure 101 Reflectance measurement for InAs/GaAs material coated with 100 nm of Si_3N_4

5.6.3 Anti-reflective coating electrical measurements

Cylindrical diodes with diameter of 250 µm were defined using wet etching. Ti/Au and Au-Ge/Au were evaporated on the top and the bottom of the device respectively. The *on-wafer* devices were coated with 100 nm of Silicon Nitride obtaining a bluish coating again. Chemical dry etching of silicon nitride in a plasma reactor using CF4 was performed to open the metal area.

5.6.3.1 J-V characteristics

The fabricated devices were mounted on TO-46 headers for electrical characterisation. A Solar simulator system was used to perform the measurements with a broadband light calibrated at 100 mWatts/cm^2 (1 sun).

The J-V characteristics under light are shown in Figure 102 for all the samples studied. Without any attempt to reduce the reflectance on the solar cell surface (line-in-black), the short circuit current density (Jsc) for sample XMBE291 is 20 mA/cm^2 and its open circuit voltage (Voc) is the lowest of all the samples at only 690 mV. The QD can act as traps for the generated electrons but doping the dots increases the probability that one electron is trapped. It is clear that the insertion of doping into the QDs, reduces the recombination phenomena in the material. The highly doped sample, sample XMBE293, exhibit the highest Voc of 800 mV.

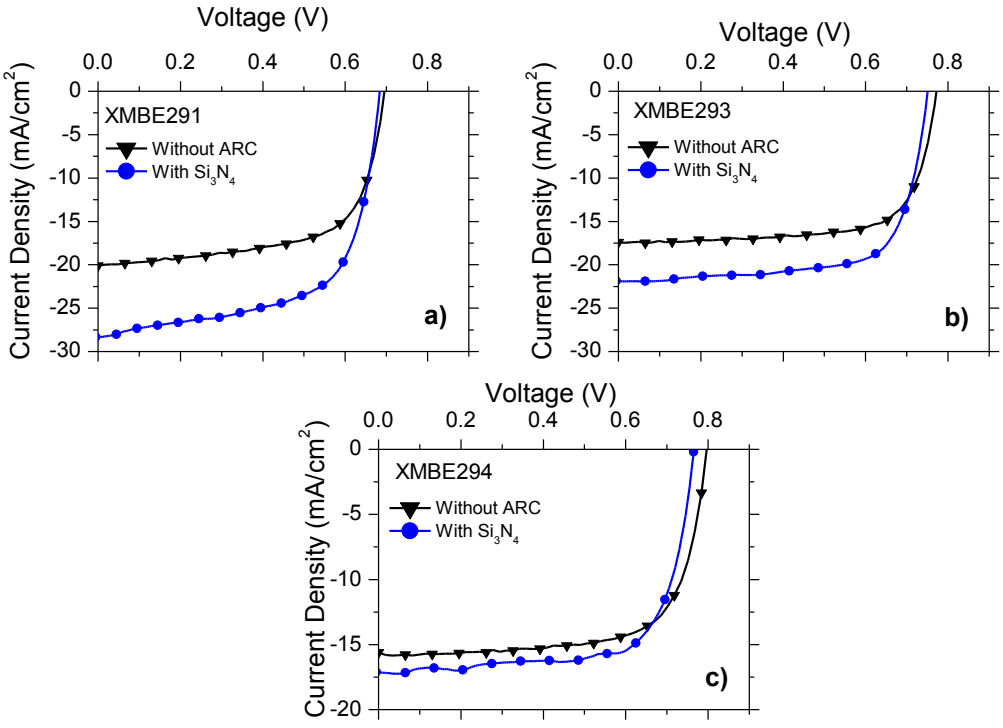

Figure 102 J-V characterisation under 1 sun (100 mW/cm^2) for samples with anti-reflective coating

The coated devices, line-in-blue in Figure 102, show a clear enhancement in the short circuit current density. For sample XMBE291, Jsc has been increased from ~20 mA/cm^2 up to ~27 mA/cm^2 yielding an enhancement of about 37 %. For Sample XMBE293, this

enhancement is around 37% and finally for Sample XMBE294 it is about 30%. The open circuit voltage (Voc) is constant for the undoped QDs sample. However, the n-inter-dot doped samples register a slight degradation in the open circuit voltage of around 30 mV.

5.6.3.2 External Quantum Efficiency

It is crucial to have an estimate of how many of the incident photons are captured and are therefore able to contribute to the photocurrent generation. To have this estimation, external quantum efficiency measurements were performed. The External quantum efficiency for the uncoated devices (line-in-black) and the Si_3N_4 coated devices (line-in-red) are shown in Figure 103. The uncoated samples exhibit very low quantum efficiency, below 40 % for the undoped sample. This is likely due to the high reflectance on the sample surface of about 60 %. Using an antireflective coating, the enhancement, compared with the uncoated ones, is evident. In the wavelength range from 750 to 1000 nm the external quantum efficiency is enhanced as a result of the device surface reflection reduction. The quantum efficiency was enhanced by up to 60%. However, below the 600 nm range where the ARC reflectance is increasing, the external quantum efficiency drops by around 8 %. The undoped sample presents the highest enhancement of the three different samples. In the inter-dot doped samples the enhancement is marginal. From 800 to 900 nm samples XMBE293 and XMBE294 display up to 40 % EQE.

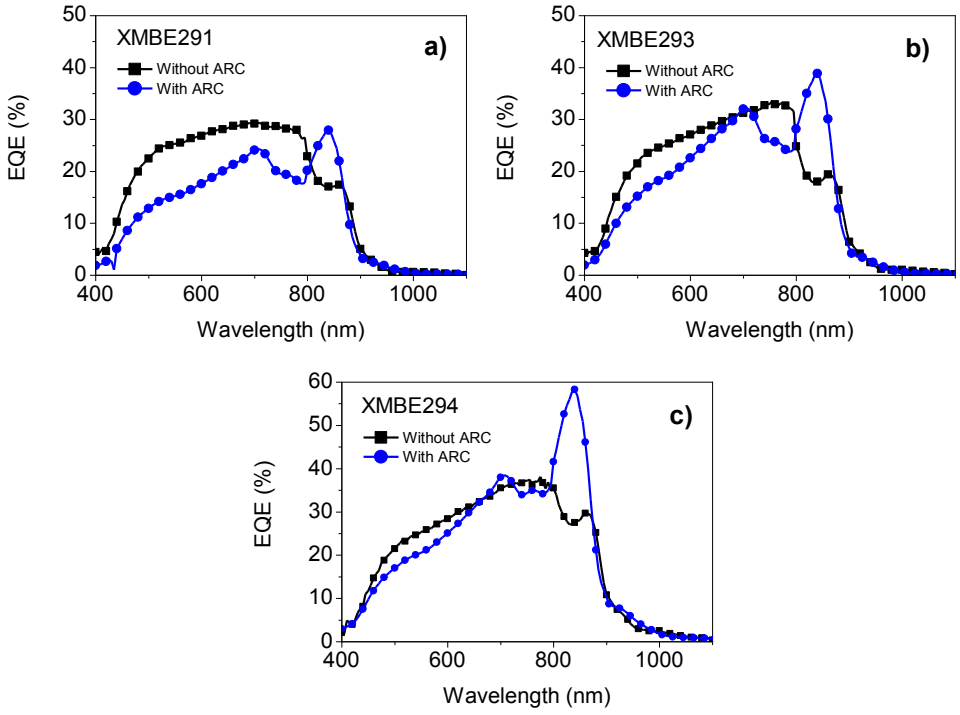

Figure 103 External quantum efficiency measurement

The efficiency calculations for the uncoated PV devices are shown in Table 17. It is clear how the insertion of the inter-dot dopant helps to increase the Fill Factor by up to ~72 % from 64 % shown by the undoped sample. This gives a clear indication of the good quality of the solar cell.

Table 17 Efficiency calculation without using antireflective coating

Sample	Jsc	Voc	Jm	Vm	FF	η (Eff)
	mA/cm^2	V	mA/cm^2	V	%	%
XMBE291	20.0	0.69	15.8	0.57	64.6	**9.0**
XMBE293	17.4	0.73	14.8	0.65	75.8	**9.6**
XMBE294	15.6	0.79	13.5	0.65	71.23	**8.8**

The efficiency calculations for 100nm Si_3N_4 coated PV devices are shown in Table 18. Here the efficiency is seen to improve by around 2.5 %. The efficiency increases from 9 % up to 11.6 % for the undoped sample. Previous reports in the literature show that the AR coating can increase the efficiency by up to 2%. The enhancement of around 2.5% in our case is higher than reported ones. [134]

Table 18 Efficiency calculation using a single layer of Si_3N_4 as antireflective coating

Sample	Jsc	Voc	Jm	Vm	FF	η (Eff)
	mA/cm^2	V	mA/cm^2	V	%	%
XMBE291	27.3	0.685	21.01	0.55	61.7	**11.6**
XMBE293	20.9	0.755	17.7	0.625	70.1	**11.0**
XMBE294	16.1	0.76	14.2	0.62	71.9	**8.8**

5.6.4 Discussions

The QDs, as an initial assumption, act as recombination centres. However, the presence of dopants in the QD layers reduces the recombination probability and thus increases the

PL intensity. This way of synthesising the diodes complements other techniques such as Quantum Dot size control and inter-dot spacing [135].

The maximum efficiency obtained in this work, 11.6 %, is an excellent value for so simple devices. The Si_3N_4, tested for the first time on InAs/GaAs QD materials, proves to be a good option as an antireflective coating. The use of Si_3N_4, reduce the reflectance on the device surface to a value of 2% and the operational wavelength can be tuned controlling the layer thickness. A 100 nm Si_3N_4 antireflective coating proves to be an excellent coating from 700 to 1000 nm. This material optical behavior is not optimum below 700 nm. In terms of short circuit current density, a 37% enhancement was achieved. This result is in excellent agreement with simulated Si3N4 and SiO_2 antireflective coating results reported with Jsc increasing by 7%. [136]

5.7 Conclusion

Systematic study and optimization were performed on InAs/GaAs QD devices. These novel cells were improved in terms of efficiency by inserting stacks of QD into different regions of the device. The effect of localized doping of such structures was also studied to maintain and enhance the open-circuit voltage which in turn increases the device efficiency. InAs/GaAs QD vertically stacked arrays exhibited the imperative need of presence of thermal energy in order to enable the intermediate band within the material. The low temperature device characterisations showed recombination processes are reduced with temperature and the effect of the doping profile inserted within the QD host lattice inhibits carrier recombination in the dots, which was the initial assumption (QDs act as recombination centres).

For high concentrator light applications, which involve operational temperature over 400K, the studied intermediate band cell structures can be used with an inter-dot doped configuration as it has been found that the inter dot doping profile reduces the efficiency degradation below the GaAs values including an excellent enhancement in the open circuit voltage. However, for normal temperature conditions the best configuration was found to have periodicity of 10 using undoped quantum dots due to its high exhibited short circuit current density at 1 sun.

CHAPTER 6

Conclusions

6.1 Conclusion

This thesis reported a detailed study of several photovoltaic materials which were grown using state-of-the-art in materials synthesis technology, molecular beam epitaxy (MBE). The wealth of optical and electrical properties of III-Vs gives the opportunity for further improvements in cell efficiency and cost reductions. Particularly, the introduction of InAs quantum dots (QDs) into the GaAs lattice extends the absorption of the device out into the near infra-red and consequently the photovoltaic device efficiency is enhanced. Our solar cells were characterized using measurements of the dark/light current-voltage (I-V) characteristics and spectral response (50-300 K). Solar cell external quantum efficiencies under standard air mass (AM) 1.5 illumination were determined and the suitability of these new cells under solar concentration were appraised.

The first set of studied solar cells based on InGaAs-InAlAs MQW showed very low efficiencies, largely as result of a drastic reduction of the open voltage as a consequence of the low band gap materials in the QW.

For these quantum well structures, the agreement between the simulated results and experimental ones was very good indeed and permitted to single out the low band gap materials in the QW as the key reason for the poor efficiencies obtained The key factors for reliable simulations are the careful selection of the device parameters and correct definition of the mesh. Furthermore, most of the InGaAs/InAlAs material systems parameters are still poorly understood, nevertheless good correlations with experimental data were obtained.

The highest measured efficiency was obtained for the high temperature grown GaAs/AlGaAs MQW sample (VMBE1661) but this sample can operate only in the visible range. Therefore, it is desirable to enhance the absorption range of the cell. In this sense,

InGaAs/InAlAs samples have been proven to have better absorption in the infrared range. This is desired, because the cell can absorb lower energy light than the GaAs/AlGaAs devices. The insertion of the strain in the quantum well structure resulted in the reduction of the absorption of the cell, as a result of low band gap of the QW materials. However, the short circuit current was increased, which is desirable.

Several simulations attempts have been performed in order to get the external quantum efficiency of the cell and an excellent trend of the EQE curve, in close agreement with experimental data was obtained. It was also from the EQE measurements that by increasing the number of wells, the efficiency is reduced.

The second part of the research work concentrated on a systematic investigation of the properties of InAs QD within GaAs with the aim of achieving enhancement of solar cell performance. Optimization was performed on these novel cells to further improve their efficiency by inserting stacks of QD into different regions of the device. The effect of localized doping of such structures was also studied to maintain and enhance the open-circuit voltage which in turn increases the device efficiency. Periodicity changes were performed in order to improve the efficiency too.

The imperative need of thermal energy in order to enable the intermediate band within the material was confirmed, for InAs/GaAs QD vertically stacked arrays. The low temperature device characterisations showed recombination processes are reduced with temperature and the effect of the doping profile inserted within the QD host lattice inhibits the generated free carriers recombination in the dots, which was the initial assumption (QDs act as recombination centres). However, the presence of dopants in the QD layers reduces the recombination probability and thus increases the PL intensity. This way of synthesising the diodes complements other techniques such as the Quantum Dot size control and inter-dot spacing [135].

The key findings of this thesis is the fact that Intermediate band photovoltaic devices using material based on InAs/GaAs vertically stacked quantum dot arrays, can be used in applications according to specific configuration criteria. For high concentrator light

applications, or other application which involve operational temperature over 400K, this type of intermediate band cell can be used with an inter-dot doped configuration as it has been found that the inter dot doping profile reduces the efficiency degradation below the GaAs values including an excellent enhancement in the open circuit voltage.

However, for normal temperature conditions (without light concentrators or junction temperature rising above 400K), a convenient configuration is with a x10 layers of undoped quantum dots. It is true that these devices do not have, a good performance at high temperatures but the periodicity changes enhances the short circuit current density while keeping a large open circuit voltage.

The best overall efficiency of 11.6 % obtained in this work is an excellent value for so simple devices configuration. The Si_3N_4, tested for the first time on InAs/GaAs QD materials, proved to be a good option as antireflective coating. The use of Si_3N_4, reduce the reflectance on the device surface to a value of 2% and the operational wavelength can be tuned by controlling the layer thickness. A 100 nm Si_3N_4 antireflective coating proved to be an excellent coating from 700 to 1000 nm. This material optical behavior is not optimum below 700 nm. In terms of short circuit current density a 37% enhancement was achieved. This result is in excellent agreement with simulated Si3N4 and SiO_2 antireflective coating results reported with Jsc increasing by 7%. [136]

The results presented in this thesis are crucial to have a better understanding in the intermediate band photovoltaic materials understanding. Theoretical premises were confirmed in the practical device operation. The impact of this works can, hopefully, help in the future improvements of the intermediate band solar cells based on InAs on GaAs QD. The performed studies presented in this thesis and the materials used are further contributions to the state-of-the-art photovoltaic materials.

6.2 Future work

It can be stated that all the initial objectives of this thesis were achieved successfully. The vertically stacked materials were confirmed as good candidates for high temperature

applications by growing, processing and characterising several InAs/GaAs quantum dot system devices. The cylindrical geometry has been found, among other fabricated geometries, to be the optimum mesa definition for very simple diodes. There is a compromise for this kind of materials design between the number of quantum dot layers and the inter-dot doping profile. The latter depends fully upon the solar cell end application.

However, there is still more work to do in terms of top contact grid pattern and anti-reflective coating design due to the development of new materials for these purposes. Regarding the top contact design, the generated shadows reduce the amount of photons that pass through the active material. There are new options like transparent conductor Silver Nano-wires deposition however the added series resistances must be minimised to take full advantage of truly transparent contact.

Appendices

Appendix A Mask Designs

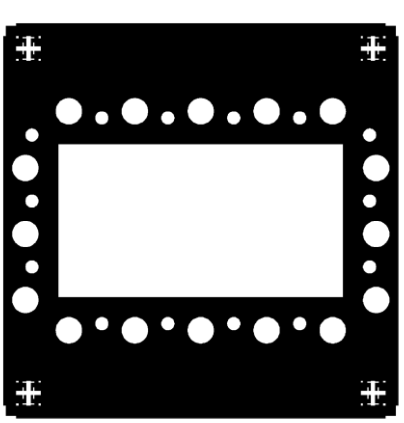

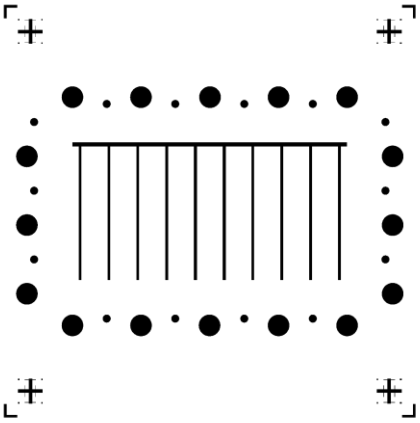

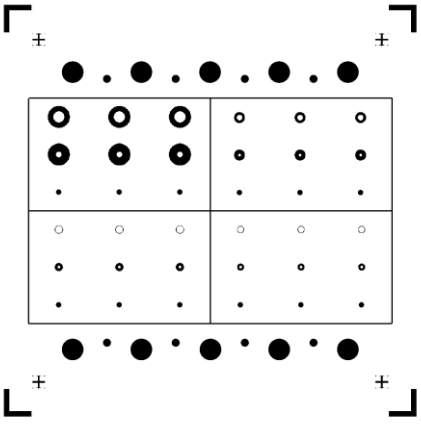

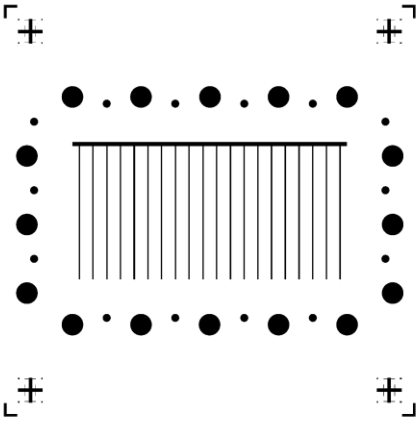

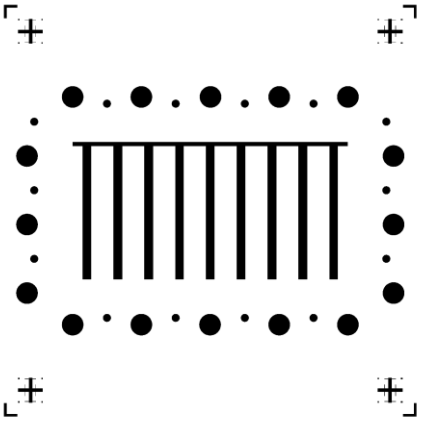

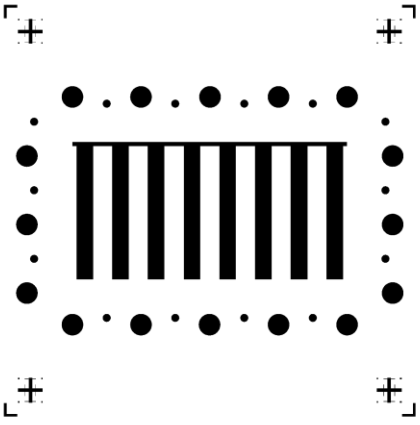

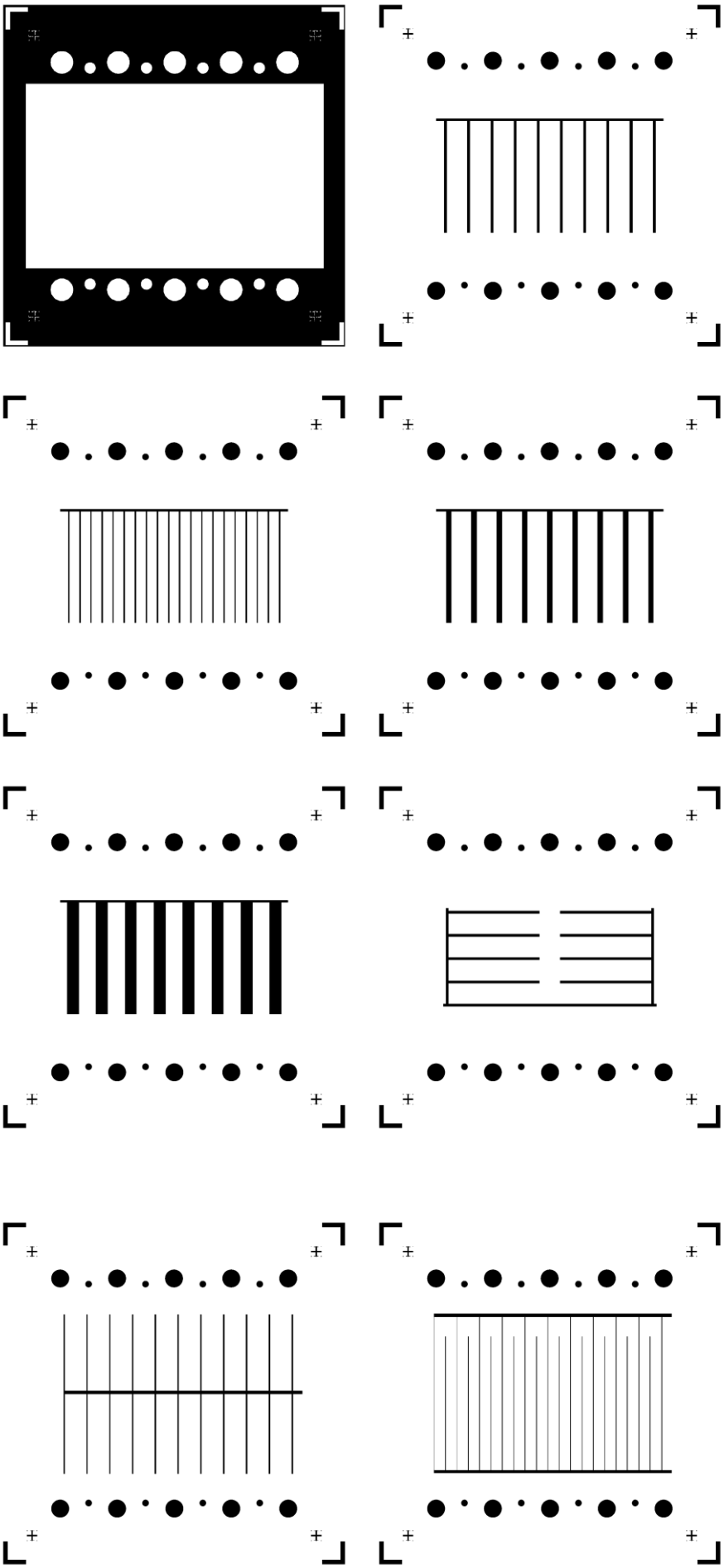

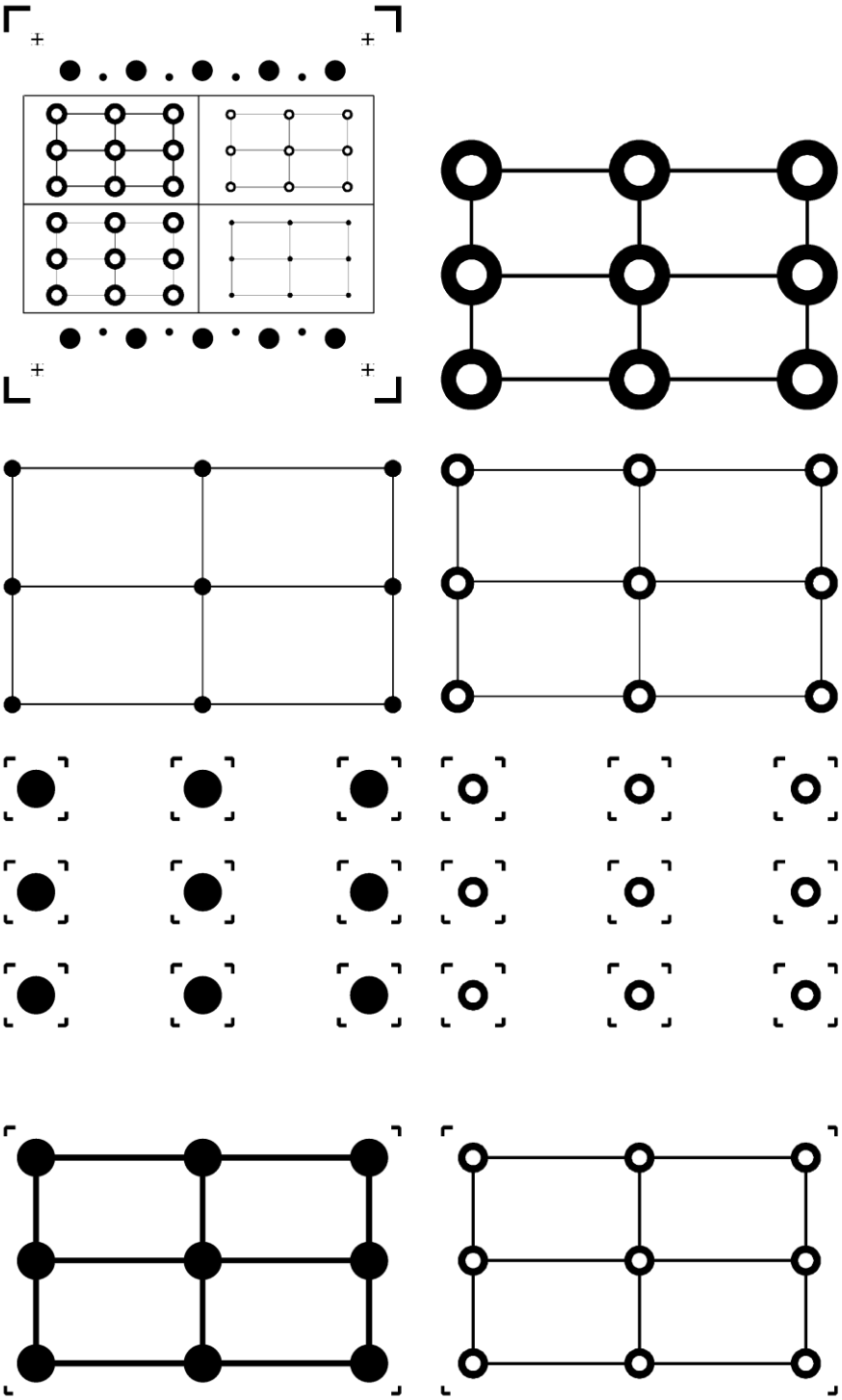

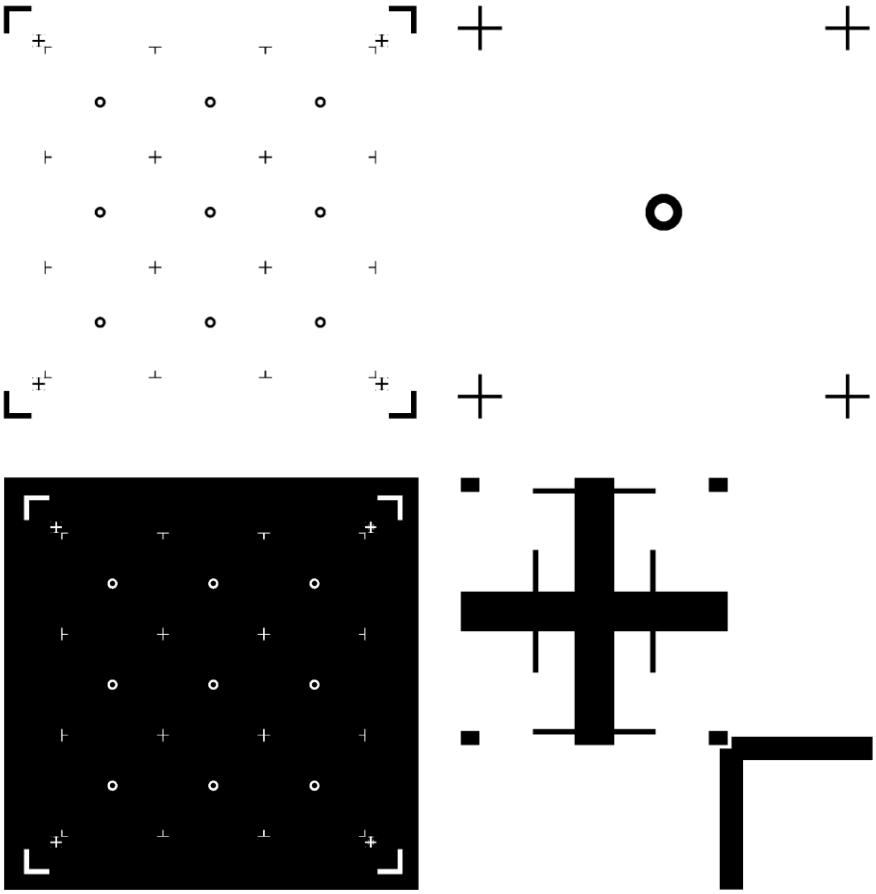

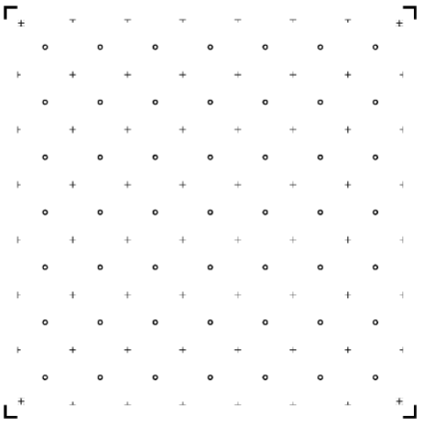

Appendix B Fabrication final recipe

	Step #	Step	Chemicals	Equipment	Temp	Time	Comments Mask: 5" QZ		
MESA	1.1	Clean	NMP(1165)/Water/Acetone/IPA	USB (Level 1)		5m each	Finally dry the sample with N_2	IPA=Propan-2-ol	
	1.2	Preheat		Hotplate	115°C	~1m	After hotplate, heat sink for 1 min at least.		
	1.3	Resist Coating	Photoresist: S1805			30s	**Program-4** (Acc=2000, RPM=4000, Duration=30s)	*Positive Resist	
	1.4	Prebake		Hotplate	115°C	1m	After hotplate, heat sink for 1 min at least.		
	1.5	Exposure		MA4		20s	Intensity=0.9mW/cm^2 for i-line	*Negative Mask	
	1.6	**Develop S1805**	**MIF 319**			**1m**	**Rinse with water and dry with N_2.**		
	1.7	Postbake		Oven	120°C	30m	To harden the remaining resist before etch.		
	1.8	Ortho-phosphoric etch	H_3PO_4:H_2O_2:H_2O (3:1:50) *H_2O_2 High grade		RT	**Calculated time!!!**	15:5:250 ml. Mesa height ~ 150nm. Ortho-phosphoric etches rate ~100nm/min InGaAs/InAlAs type pHEMT, and, ~80nm/min GaAs/InAlAs type pHEMT. It doesn't etch InP. Etch to buffer layer (160nm=1m 30s)	H_3PO_4 = Ortho-phosphoric Acid	H_2O_2=Hydrogen Peroxide
	1.9	Side-wall etch	Succinic acid powder (10g), H_2O (50ml), Ammonia (~10ml to pH of 5.5), H_2O_2 (5 ml)	pH meter	RT	**5m**	Allow the solution to settle for 5m before etching. Add H_2O_2 only after pH of 5.5 is achieved by the intermittent addition of ammonia.	**Side wall etch for better gate thermal stability-Isolation of gate from channel will elimanate any possibilities of leakage current after heat is applied	
Back contact	2.1	Evaporation	**AuGe/Au 50nm/100nm**	Biorad			Load ~70mg AuGe and 10cm Au **AuGe will allow Au to diffuse inti S/C to make metalisation	**If the results are not OK, additional annealing at 290°C for 60s**	Layer: AuGe=3, Au=2
	2.2	Anneal		Alloing equipment	250°C	120s	N_2 flow: 150 (N_2 at 30 is idle), Rc~0.15-0.18 ohm/mm	**Diffusing metal on doped surface**	
OHMICS	2.1	Clean	Acetone/IPA	USB (Level 1)			Dry with N_2		
	2.2	Resist coating	Photoresist: AZnLOF 2070 (2um grade)	Spinner			Program-6 (Acc=2000, RPM=3000, Duration=30s)	* Negative resist	-
	2.3	**Softbake**		**Hotplate**	**100°C**	**1m**	**After hotplate, heat sink for 1 min.**		
	2.4	**Exposure**		**MA4**		**4s**	**Intensity=0.9mW/cm^2 for i-line**	*** Negative mask**	**No EBR**
	2.5	**PEB (Post Exposure Bake)**		**Hotplate**	**110°C**	**1m**	**After hotplate, heat sink for 1 min.**		
	2.6	Develop AZnLOF 2070	MIF 326			1m	Because of the negative resist, the exposed region polymerises and unexposed region gets dissolved in the developer. Rinse with water and dry with N_2.		
	2.7	Plasma with molecular Oxigen		Plasma		0.33 (20s)	Power: 100 (25W) Oxigen Flow: 0.50		
	2.8	Evaporation	**Ti/Au 50nm/100nm**	Biorad			Load ~2cm Ti and 6cm Au		
	2.9	Lift-off	NMP (1165)						
	2.10	Clean	Water			3m	Dry with N_2		
	2.11	Anneal		Alloing	250°C	2m			

Appendix C "XMBE242" SILVACO optimisation

The optimization process was divided into 6 different steps:

7. Barrier-Well thickness optimization
8. Spacer layers (intrinsic) thickness optimization
9. n/p (Base/Emitter) layer thickness optimization
10. Window layer thickness optimization
11. Buffer thickness optimization
12. Final structure

XMBE242 InGaAs / InAlAs QW Solar cell (x25)

x25	p-type	InGaAs	**Cap**
	p-type	InAlAs	**Window**
	p-type	InAlAs	**Emitter**
	i	InAlAs	**Spacer**
	i	InAlAs	**Barrier**
	i	InGaAs	**well**
	i	InAlAs	**Spacer**
	n-type	InAlAs	**Base**
	n-type	InAlAs	**Buffer**
	n+	InP	

Contacts

Barrier-Well thickness optimization

The next figure presents the simulation results for different barrier thickness (150, 100 and 80 Å). The rest of the structure has the same dimensions.

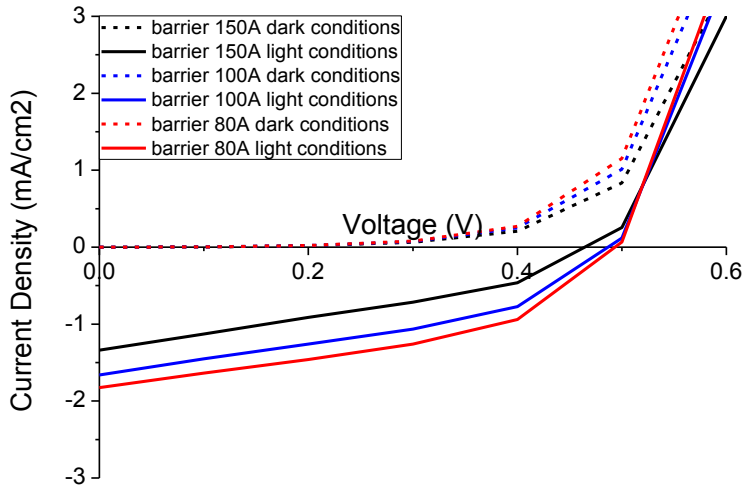

Figure 104 Barrier thickness variations from 80 Å to 150 Å

The short circuit current was increased with a reduction in barrier thickness. The Voc was increased too.

Table 19 Barrier thickness analysis

Barrier thickness (Å)	Isc (mA/cm2)	Voc (V)
150	1.34	0.465
100	1.66	0.48
80	1.83	0.49

The changes in thickness are shown in two different figures, the difference between them is the barrier thickness, it was fixed for each figure at 150 and 80 Å. For each figure the different well thicknesses are 150, 100 and 80 Å. If both well and barrier thicknesses are reduced then both the Isc and Voc are enhanced.

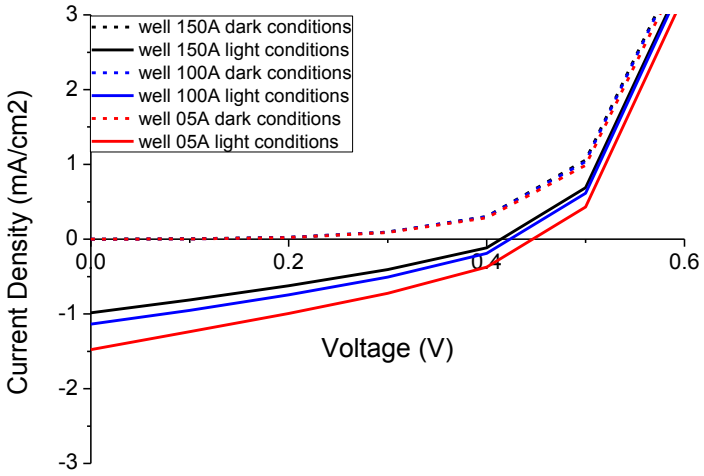

Figure 105 Well thickness variation from 50 Å to 150 Å

Both the short circuit current and the open circuit voltage Voc were increased with a reduction in the well thickness.

Table 20 Well thickness analysis

Well thickness (Å)	Isc (mA/cm2)	Voc (V)
150	1.00	0.41
100	1.14	0.42
50	1.48	0.45

Both Isc and Voc are enhanced when reducing the thicknesses of both well and barrier. Therefore according to the simulations the optimum thicknesses are:

Well = 50 Å
Barrier = 80 Å

Spacer layers (intrinsic) thickness optimization

The changes in thickness are shown in two different steps, one for each layer:

1. The first step is on the Spacer layer next to n-type layers (Layer2)

   Thicknesses: 150 , 100 and 50 Å (Figure 106)

2. The second step is on the Spacer layer next to p-type layers (Layer1)

   Thicknesses: 150 , 100 and 50 Å (Figure 107)

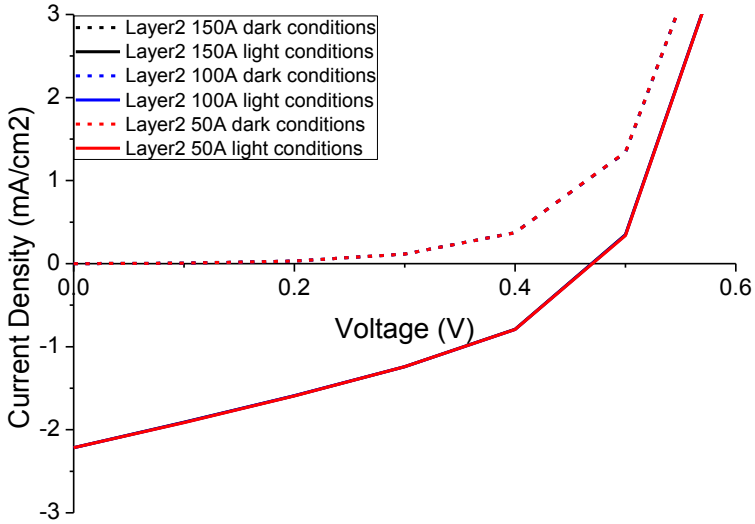

Figure 106 Layer 2 thickness analysis

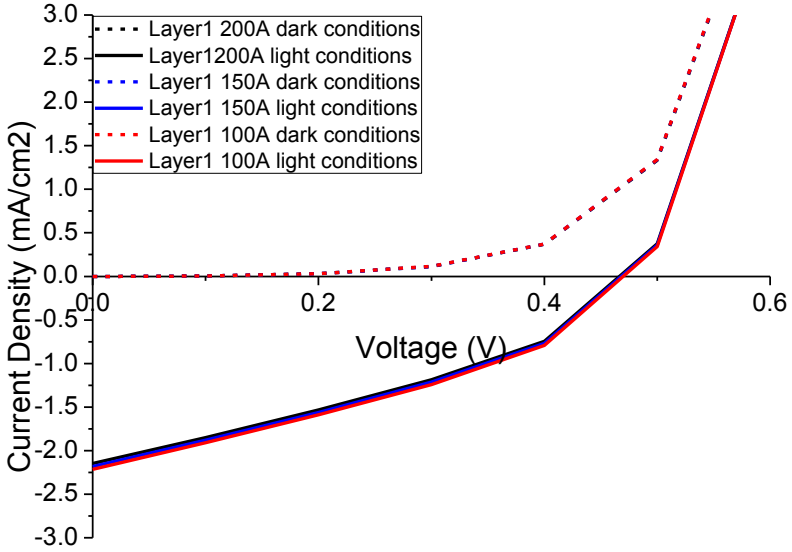

Figure 107 Layer 1 thickness analysis

Table 21 Layer 2 J-V simulation

Layer2 thickness (Å)	Isc (mA/cm2)	Voc (V)
150	2.22	0.46
100	2.22	0.46
50	2.22	0.46

Table 22 Layer 1 J-V simulation

Layer1 thickness (Å)	Isc (mA/cm2)	Voc (V)
150	2.18	0.46
100	2.22	0.46
50	2.23	0.46

No significant changes. The initial thickness is adequate. Therefore the Spacer layers thicknesses are kept at **100 Å.**

n/p (Base/Emitter) layer thickness optimization

The pLayer thickness is varied as such: 250, 200, 150, 100, 50 and 20 Å

Table 23 pLayer J-V simulations

pLayer thickness (Å)	Isc (mA/cm2)	Voc (V)
250	1.96	0.46
200	2.22	0.47
150	2.45	0.48
100	2.69	0.50
50	2.99	0.51
20	2.92	0.51

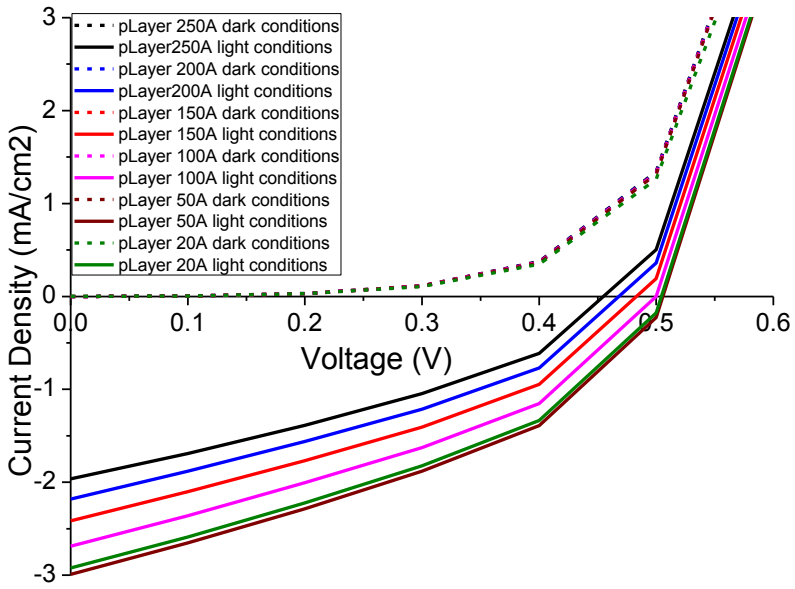

Figure 108 pLayer thickness analysis

In the pLayer case, the optimum thickness value is 50 Å, it increases the Isc up to 3 mA/cm2 and the Voc up to 0.51V. The nLayer thickness simulated were: 15000,11000, 10000 and 9000 Å

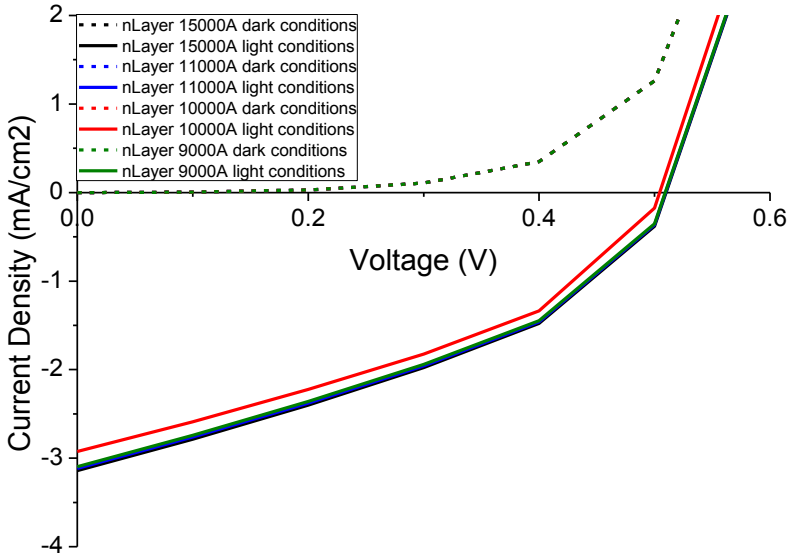

Figure 109 nLayer thickness analysis

Table 24 nLayer J-V simulations

nLayer thickness (Å)	Isc (mA/cm2)	Voc (V)
15000	3.14	0.52
11000	3.12	0.52
10000	2.99	0.51
9000	3.12	0.52

Therefore for the pLayer case, the optimum thickness value is 9000 Å, it increases the Isc up to 3.1 mA/cm2 and the Voc up to 0.512 V.

Window layer thickness optimization

The window thickness is varied from as such: 1000, 800, 500, 200 and 100 Å

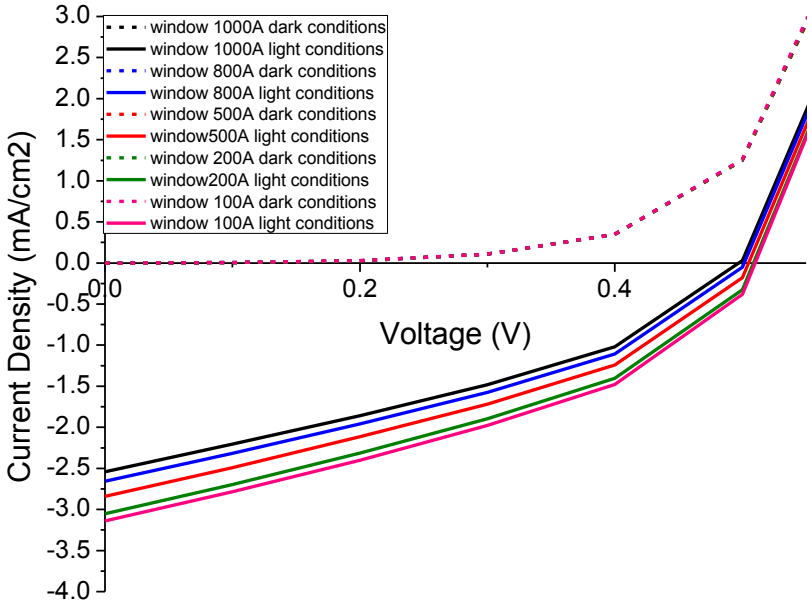

Figure 110 Window layer thickness analysis

Table 25 Window layer J-V simulations

Window thickness (Å)	Isc (mA/cm2)	Voc (V)
1000	2.54	0.510
800	2.66	0.511
500	2.84	0.512
200	3.05	0.513
100	3.14	0.514

The optimal thickness is 100 A as in the original structure, the thinner layer could increase the Isc up to 3.1 mA/cm2 and up to 5.14 V the Voc.

Buffer thickness optimization

The buffer thickness is varied as such: 4000, 3000, 2500 and 1500 Å

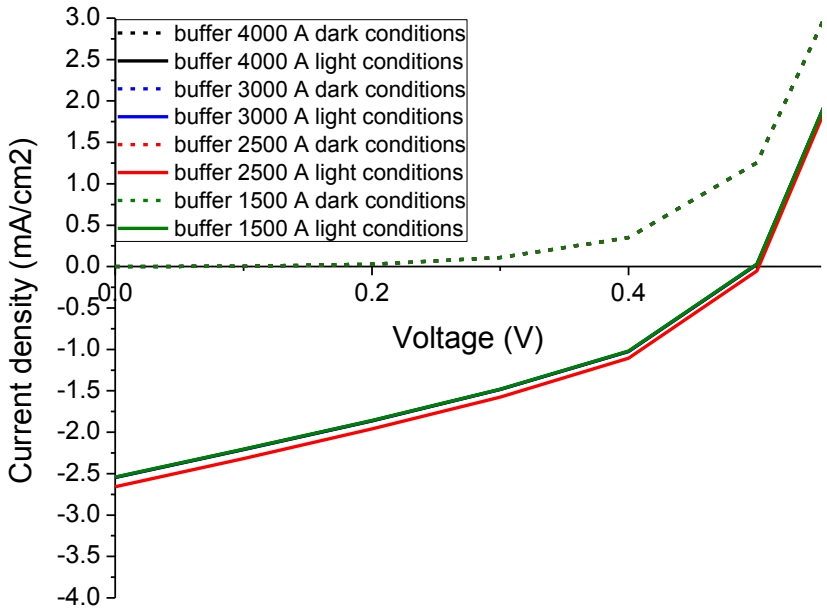

Figure 111 Buffer layer thickness analysis

Table 26 Buffer layer J-V simulations

Buffer thickness (Å)	Isc (mA/cm2)	Voc (V)
4000	2.55	0.51
3000	2.54	0.51
2500	2.66	0.51
1000	2.55	0.51

The optimum value is 2500 A as in the original structure.

Appendix D XMBE242 SILVACO Modelling Code

```
########################
# Solar cells
########################
# Edson Garduno Nolasco
########################
# xmbe242
########################
# PhD UoM - EEE
#InGaAs/InAnAs MQW cells
########################
# QW Modelling
########################

go atlas

#----------------------------------------
#Structure parameter definition (Constants)
#----------------------------------------

## Thicknesses
set t_top=0.075
set t_window=0.010
set t_pLayer=0.200
set t_layer1=0.010
set t_qw1=0.015
set t_qw2=0.010
set t_layer2=0.010
set t_nLayer=1.000
set t_buffer=0.250
set t_substr=500.0

## Doping concentrations
set d_top=4e+17
set d_window=9e+17
set d_pLayer=9e+17
set d_nLayer=9.3e+17
set d_buffer=9e+17
set d_substr=9e+17


## Compoisitions
set c_top=0.52
set c_window=0.30
set c_pLayer=0.53
set c_layer1=0.48
set c_qw1=0.50
set c_qw2=0.42
set c_layer2=0.48
set c_nLayer=0.53
set c_buffer=0.52


## Other parameters
set wmesh=1
set nqw=15

## Layers
set A=$t_top
set B=$A+$t_window
```

```
set C=$B+$t_pLayer
set D=$C+$t_layer1
set E=$D+($t_qw1+$t_qw2)*$nqw
set F=$E+$t_layer2
set G=$F+$t_nLayer
set H=$G+$t_buffer
set I=$H+$t_substr

## Regions numbers
set rA=1
set rB=$rA+1
set rC=$rB+1
set rD=$rC+1
set rF=1+($nqw*2)+$rD
set rG=$rF+1
set rH=$rG+1
set rI=$rH+1



#--------------------------------------
# Mesh generator
#--------------------------------------

mesh auto width=$wmesh

## The x.mesh and y.mesh specifies the location 'loc' of mesh grid lines along the respective
## axis. 'spacing' determines the mesh spacing in microns at the position specified by 'loc'
## parameter. The mesh spacing from one mesh statement to the next is gradually changed and is
## managed by the simulator itself.

x.mesh   l=-$wmesh/2       s=5
x.mesh   l=$wmesh/2  s=5

# Top
y.mesh   l=0.000  s=0.005
y.mesh l=$A                s=0.001

# Window
y.mesh   l=$A              s=0.001
y.mesh   l=$B              s=0.001

# pLayer
y.mesh   l=$B              s=0.01
y.mesh   l=$C              s=0.01

# layer1
y.mesh   l=$C              s=0.001
y.mesh   l=$D              s=0.001

# Quantum wells
y.mesh   l=$D              s=0.001
y.mesh   l=$E              s=0.001

# layer2
y.mesh   l=$E              s=0.001
y.mesh   l=$F              s=0.001

# nLayer
y.mesh   l=$F              s=0.01
y.mesh   l=$G              s=0.01
```

```
# Buffer
y.mesh   l=$G              s=0.001
y.mesh   l=$H              s=0.01

# Substr
y.mesh   l=$H              s=50
y.mesh   l=$I              s=50
#-----------------------------------
# SECTION 2: Structure Specification
#-----------------------------------

#-----------------------------------
# Regions definition
#-----------------------------------

region num=$rA  name=top                material=InGaAs x.comp=$c_top           y.min=0
        y.max=$A
region num=$rB  name=window             material=InAlAs  x.comp=$c_window       y.min=$A
        y.max=$B
region num=$rC  name=pLayer             material=InAlAs  x.comp=$c_pLayer       y.min=$B
        y.max=$C
region num=$rD  name=layer1             material=InAlAs  x.comp=$c_layer1       y.min=$C
        y.max=$D

# MQW region
dbr half.cyc=$nqw*2 thick1=$t_qw1 thick2=$t_qw2 mat1=InAlAs mat2=InGaAs x1.comp=$c_qw1
x2.comp=$c_qw2 y.start=$D y.end=$E qwell2 n1=6 n2=6
# End qw region

region num=$rF   name=layer2      material=InAlAs  x.comp=$c_layer2       y.min=$E
        y.max=$F
region num=$rG  name=nLayer       material=InAlAs  x.comp=$c_nLayer       y.min=$F
        y.max=$G
region num=$rH  name=buffer       material=InAlAs  x.comp=$c_buffer       y.min=$G
        y.max=$H
region num=$rI   name=substr            material=InP
        y.min=$H        y.max=$I


#---------------------------------
# Electrodes
#---------------------------------

electrode       num=1   name=cathode    material=Gold           y.min=  $I      y.max=  $I
electrode       num=2   name=anode      material=Gold           y.min=  0.0     y.max=  0.0



#---------------------------------
# Doping
#---------------------------------

doping   uniform p.type         conc=$d_top             Region=$rA
doping   uniform p.type         conc=$d_windowRegion=$rB
doping   uniform p.type         conc=$d_pLayer  Region=$rC

doping   uniform n.type         conc=$d_nLayer  Region=$rG
doping   uniform n.type         conc=$d_buffer   Region=$rH
doping   uniform n.type         conc=$d_substr   Region=$rI


#--------------------------
```

```
#Contacts
#-------------------------

contact name=     anode
contact name=     cathode


#----------------------------------------
# SECTION 3: Material & Models Definitions
#----------------------------------------

## The physical parameters for the materials are defined in the following three sub-sections

#MATERIAL REAL.INDEX=1.0 IMAG.INDEX=0.0
material material=Gold     sopra=Au.nk
material material=InGaAs sopra=ingaas.nk
material material=InAlAs  sopra=ingaas.nk
material material=Lp23              sopra=ingaas.nk
material material=Lp52              sopra=ingaas.nk
material material=Lil               sopra=ingaas.nk
material material=Li2               sopra=ingaas.nk
material material=Ln52              sopra=ingaas.nk
material material=Ln23              sopra=ingaas.nk

material material=InP               sopra=inp.nk

########BAND DIAGRAM ####

output e.field e.mobility e.temp e.velocity con.band val.band charge flowlines devdeg

#STRUCTURE GRAPHIC
solve init
save outf=xmbe242_ qw.str
tonyplot xmbe242_qw.str

########END BAND DIAGRAM ####

#quit



#----------------------------------------
   ###### ANALYSIS #####
#----------------------------------------
models srh fermi conmob optr auger bgn

method newton
contact  name=anode        workf=5.032


solve     init
log       outf="xmbe242const_qwdark.log"
solve     vanode=-1.0 name=anode vstep=0.05 vfinal=1.0
log       off

tonyplot xmbe242const_qwdark.log -set edson.set

#quit


#### Light IV condition
```

```
beam num=1 AM1.5 wavel.start=0.1 wavel.end=1.4 wavel.num=50

output opt.int
probe name=inten beam=1 intensity

solve init

solve b1=1e-04
solve b1=1e-02
solve b1=1e-01

log       outf="xmbe242iv.log"

solve vanode=0 name=anode vstep=0.01 vfinal=1

log off

tonyplot -overlay xmbe242const_qwdark.log xmbe242dark.log xmbe242iv.log -set edson_IV.set

extract init inf="xmbe242iv.log"

extract name="Isc" y.val from curve(V."anode", I."cathode") where x.val=0.0
#max(abs(i."cathode"))
extract name="Voc" x.val from curve(V."anode", I."cathode") where y.val=0.0
extract name="Pm" max(curve(V."anode",(V."anode" * I."cathode")))
extract name="Vm" x.val from curve(V."anode", (V."anode"*I."cathode") ) where y.val=$"Pm"
extract name="Im" $"Pm"*$"I"*$"I"*$"I"/$"Vm"
extract name="FF" ($"Pm"/($"Isc"*$"Voc"))
extract name="intens" max(probe."inten")
extract name="Eff" ($Pm/($"intens"*0.2628))

# OPTICAL RESPONSE
models conmob fldmob consrh print

# spectral response
solve init
solve previous
solve previous b1=0
log outf=vmbe2016_spectral.log
solve b1=1 beam=1 lambda=0.3 wstep=0.025 wfinal=1.0

tonyplot xmbe242_spectral.log -set solarex01_3.set


# The "Available photo current" accounts for absorption in semiconductor regions only.
# Users interested in the overall absorption need to calculate EQE as:
# EQE=I anode / I Source Photo Current * Asorption

extract init inf="xmbe242_spectral.log"
extract name="IQE" curve(elect."optical wavelength", \
   -(i."anode")/elect."available photo current") outf="IQE.dat"
extract name="EQE" curve(elect."optical wavelength", \
   -(i."anode")/elect."source photo current") outf="EQE.dat"
extract name="EQE2" curve(elect."optical wavelength", \
   -(i."anode")/elect."source photo current"*elect."Absorption") outf="EQE2.dat"

tonyplot IQE.dat -overlay EQE2.dat -set solarex01_1.set
####
```

References

[1] N. A. Sobolev, "Radiation Effects in Quantum Dot Structures," in *Handbook of Self Assembled semiconductor Nanostructures for Novel Devices in Photonics and Electronics*, Elsevier, 2008, pp. 392-447.

[2] K. A. Sablon, J. W. Little, V. Mitin, A. Sergeev, N. Vagidov and K. Reinhardt, "High-efficiency quantum dot solar cells due to inter-dot n-doping," *Next Generation (Nano) Photonic and Cell Technologies for Solar Energy Conversion II. SPIE Proceedings,* vol. 8111, no. 1, pp. 81110H-1 - 81110H-10, 2011.

[3] A. Marti, N. Lopez, E. Antolin, E. Canovas and A. Luque, "Emitter degradation in quantum dot intermediate band solar cells," *Applied Physics Letters,* vol. 90, no. 1, pp. 2335101 - 2335103, 2007.

[4] Y. Hamakawa, "Solar PV energy conversion and the 21st century's civilization," *Solar Energy Materials and Solar Cells,* vol. 74, no. 1-4, pp. 13-23, 2002.

[5] A. Cuevas, A. Luque, J. Eguren and J. Del Alamo, "High efficiency bifacial back surface field solar cells," *Solar cells,* vol. 3, no. 4, pp. 337-340, 1981.

[6] B. Robles-Ocampo, E. Ruiz-Vasquez, H. Canseco-Sanchez, R. C. Cornejo-Meza, G. Trapaga-Martinez, F. J. Garcia-Rodriguez, J. Gonzalez-Hernandez and Y. V. Vorobiev, "Photovoltaic/thermal solar hybrid system with bifacial PV module and transparent plane collector," *Solar Energy Materials and Solar Cells,* vol. 91, no. 20, pp. 1966-1971, 2007.

[7] R. Zakharchenko, L. Licea-Jimenez, S. A. Perez-Garcia, P. Vorobiev, U. Dehesa-Carrasco, J. F. Perez-Robles, J. Gonzalez-Hernandez and Y. Vorobiev, "Photovoltaic solar panel for a hybrid PV/thermal system," *Solar Energy Materials and Solar Cells,* vol. 82, no. 1-2, pp. 253-261, 2004.

[8] J. Peet, M. L. Senatore, A. J. Heeger and G. C. Bazan, "The Role of Processing in the Fabrication and Optimization of Plastic Solar Cells," *Advance Materials,* vol. 21, no. 14-15, pp. 1521-1527, 2009.

[9] L. Xue, L. Liu, Q. Gao, S. Wen, J. He and W. Tian, "Planar-diffused photovoltaic device based on the MEH-PPV/PCBM system prepared by solution process," *Solar Energy Materials and Solar Cells,* vol. 93, no. 4, pp. 501-507, 2009.

[10] R. Valaski, C. D. Canestraro, L. Micaroni, R. M. Q. Mello and L. S. Roman, "Organic photovoltaic devices based on polythiophene films electrodeposited on FTO substrates," *Solar Energy Materials and Solar Cells,* vol. 91, no. 8, pp. 687-688, 2007.

[11] J. Y. Kim, K. Lee, N. E. Coates, D. Moses, T.-Q. Nguyen, M. Dante and A. J. Heeger, "Efficient Tandem Polymer Solar Cells Fabricated by All-Solution Processing," *Science,* vol. 317, no. 5835, pp. 222-225, 2007.

[12] Y. S. Kim, J. H. Park, S.-H. Lee and Y. Lee, "Polymer photovoltaic devices using highly conductive poly (3,4-ethylenedioxythiophene-methanol)electrode," *Solar Energy Materials and Solar Cells,* vol. 93, no. 8, pp. 1398-1403, 2009.

[13] G. D. Sharma, R. Kumar, S. Kumar Sharma and M. S. Roy, "Charge generation and photovoltaic properties of hybrid solar cells based on ZnO and copper phthalocyanines (CuPc)," *Solar Energy Materials and Solar Cells,* vol. 90, no. 7-8, pp. 933-943, 2006.

[14] B. Streetman, Solid State Electronic Devices, 2nd ed., Prentice Hall Inc., 1980.

[15] T. Tiedje, E. Yablonovitch, G. D. Cody and B. G. Brooks, “Limiting Efficiency of Silicon Solar Cells,” *Electron Devices, IEEE Transactions,* vol. 31, no. 5, pp. 711-716, 1984.

[16] M. A. Green, “Crystalline Silicon Solar Cells,” in *Clean Electricity from Photovoltaics,* London, UK, Series on Photoconversion of Solar Energy, 2001, p. 49.

[17] Y. Bai, D. H. Ford, J. A. Rand and R. B. Hall, “16.6% Efficient silicon-filmtm polycrystalline silicon solar cells,” *16th Photovoltaic Specialists Conference,* vol. 16, no. 1, pp. 35-38, 1997.

[18] H. Ruiying, C. P. Murcia, T. Creazzo and T. Biegala, “Thin silicon solar cells using epitaxial lateral overgrowth structure,” *Photovoltaic Specialists Conference (PVSC),* vol. 34, no. 1, pp. 949-953, 2009.

[19] F. Dimroth, “High-efficiency solar cells from III-V compound,” *Physics of State Solid (C),* vol. 1, no. 3, pp. 373-379, 2006.

[20] F. Dimroth, “High-efficiency solar cells from III-V compound semiconductors,” *Physica Status Solidi (c),* vol. 3, no. 3, pp. 373-379, 2006.

[21] R.-H. Horng, S.-T. Lin, Y.-L. Tsai and M.-T. Chu, “Improved Conversion Efficiency of GaN/InGaN Thin-Film Solar Cells,” *Electron Devices Letters, IEEE,* vol. 30, no. 7, pp. 724-726, 2009.

[22] J. Nelson, The Physics of solar cells, London: Imperial College Press, 2003.

[23] M. Yamaguchi, Y. Ohmachi, T. Oh'hara and Y. Kadota, “GaAs-on-Si solar cells for space use,” *Photovoltaic Specialists Conference,* vol. 28, no. 1, pp. 1012-1015, 2000.

[24] S. P. Tobin, S. M. Vernon, C. Bajgar and V. E. Haven, “High efficiency GaAs/Ge monolithic tandem solar cells,” *Photovoltaic Specialists Conference,* vol. 20, no. 1, pp. 405-410, 1988.

[25] S. Gasner, G. Pack, M. Gates and R. Given, “Stability of GaAs/Ge solar cells with standard front contacts after long-term, high-temperature exposure,” *Photovoltaic Specialists Conference,* vol. 21, no. 2, pp. 1314-1319, 1990.

[26] M.-C. Tseng, R.-H. Horng, Y.-L. Tsai and D.-S. Wuu, “Fabrication and Characterization of GaAs Solar Cells on Copper Substrates,” *Electron Device Letters, IEEE,* vol. 30, no. 9, pp. 940-942, 2009.

[27] C. Hardingham, C. Huggings, T. Cross, A. Gray, K. Mullaney and C. Kitchen, “Ultrathin, directly glassed, GaAs solar cells,” *Photovoltaic Specialists Conference,* vol. 23, no. 1, pp. 1399-1403, 1993.

[28] J. M. Woodall and H. J. Hovel, “High-efficiency Ga1−x Al x As–GaAs solar cells,” *Applied Physics Letters,* vol. 21, no. 8, pp. 379-381, 1972.

[29] “Ioffe Physical Technical Institute,” Ioffe Physical Technical Institute, [Online]. Available: http://www.ioffe.ru/SVA/NSM/Semicond/AlGaAs/.

[30] G. S. Kamath, J. Ewan and R. C. Knechtli, “Large-area high-efficiency (AlGa)As-GaAs solar cells,” *Electron Devices IEEE Transactions,* vol. 24, no. 4, pp. 473-475, 2005.

[31] M. Konagai, M. Sugimoto and K. Takahashi, “High efficiency GaAs thin film solar cells by peeled film technology,” *Journal of Crystal Growth,* vol. 45, no. 1, pp. 277-280, 1978.

[32] E. Aperathitis, Z. Hatzopoulos, M. Kayambaki and V. Foukaraki, “1 cm×1 cm GaAs/AlGaAs MQW solar cells under one sun and concentrated sunlight,” *Photovoltaic Specialists Conference,* vol. 28, no. 1, pp. 1142-1145, 2000.

[33] D. L. Miller, S. W. Zehr and J. S. J. Harris, “GaAs-AlGaAs tunnel junctions for multigap cascade solar cells,” *Journal of Applied Physics,* vol. 53, no. 1, pp. 744-748, 1982.

[34] S. M. Ramey and R. Khoie, "Modeling of multiple-quantum-well solar cells including capture, escape, and recombination of photoexcited carriers in quantum wells," *Electron Devices, IEEE Transactions,* vol. 50, no. 5, pp. 1179-1188, 2003.

[35] A. C. Varonides and R. A. Spalletta, "III–V triple junctions and MQW-fine tuning at 1 EV in synergy for high efficiency solar cells," *Photovoltaic Specialists Conference (PVSC), IEEE,* vol. 34, no. 1, pp. 282-286, 2009.

[36] Y. Watanabe, Y. Kadota, H. Okamoto, M. Seki and Y. Ohmachi, "Structural properties of GaAs-on-Si with InGaAs/GaAs strained-layer superlattice," *Journal of Crystal Growth,* vol. 93, no. 1, pp. 459-465, 1988.

[37] G. Haarpaintner, J. Barnes, K. W. J. Barnham and J. P. Connolly, "Voltage performance of quantum well solar cells in the Alx Ga1-xAs/GaAs and the GaAs/InyGa1-yAs material systems," *Photovoltaic Energy Conversion,* vol. 2, no. 1, pp. 1783-1786, 1994.

[38] D. Teng, P. Mandeville and L. F. Eastman, "Growth limitations of strained multiple quantum wells," *Journal of Crystal Growth,* vol. 135, no. 1-2, pp. 36-40, 1994.

[39] F. W. Ragay, J. H. Wolter, A. Marti and G. L. Araujo, "Experimental analysis of GaAs-InGaAs MQW solar cells," *Photovoltaic Energy Conversion,* vol. 2, no. 24, pp. 1754-1758, 1994.

[40] M.-J. Yang and M. Yamaguchi, "Properties of GaAs/InGaAs quantum well solar cells under low concentration ratios," *Photovoltaic Specialists Conference,* vol. 1, no. 26, pp. 915-918, 1997.

[41] J. F. Geisz, D. J. Friedman, J. S. Ward and A. Duda, "40.8% efficient inverted triple-junction solar cell with two independently metamorphic junctions," *Applied Physics Letters,* vol. 93, no. 12, pp. 123505 - 123505-3, 2008.

[42] J.-H. Baek, B. Lee, S. W. Choi, J. H. Lee and E.-H. Lee, "Measurement of index of refraction of In x Al1−x As epitaxial layer using in situ laser reflectometry," *Applied Physics Letters,* vol. 68, no. 17, pp. 2355-2357, 1996.

[43] S. Nojima and H. Asahi, "Refractive index of InGaAs/InAlAs multiquantum-well layers grown by molecular-beam epitaxy," *Journal of Applied Physics,* vol. 63, no. 2, pp. 479-483, 1988.

[44] S. Sinharoy, M. A. Stan, A. M. Pal, V. G. Weizer, M. A. Smith, D. M. Wilt and K. Reinhardt, "MOVPE growth of lattice-mismatched Al 0.88In 0.12As on GaAs (1 0 0) for space solar cell applications," *Journal of Crystal Growth,* vol. 221, no. 1, pp. 683-687, 2000.

[45] S. T. Davey, M. A. G. Halliwell, D. C. Rogers, M. R. Taylor and E. G. Scott, "On the determination of alloy compositions in GaInAs/AlInAs multiple quantum wells," *Journal of Crystal Growth,* vol. 96, no. 2, pp. 258-264, 1989.

[46] K. Barnham, J. Connolly, P. Griffin, G. Haarpaintner, J. Nelson and E. Tsui, "Voltage enhancement in quantum well solar cells," *Journal of Applied Physics,* vol. 80, no. 2, pp. 362857-1 362857-5, 1996.

[47] F. W. Ragay, J. H. Wolter, A. Marti and G. L. Araujo, "Experimental analysis of GaAs-lnGaAs MQW solar cells," *Photovoltaic Energy Conversion,* vol. 2, no. 1, pp. 1754-1758, 1994.

[48] S. M. Ramey and R. Khoie, "Modeling of Multiple-Quantum-Well Solar Cells Including Capture, Escape, and Recombination of Photoexcited Carriers in Quantum Wells," *Electron Devices, IEEE Transactions on,* vol. 50, no. 5, pp. 1179-1188, 2003.

[49] J. M. Mohaidat, K. Shum, W. B. Wang and R. R. Alfano, "Barrier potential design criteria in multiple quantum well based solar cell structures," *Journal of Applied Physics,* vol. 76, no. 9, pp. 5533-5537, 1994.

[50] D. Teng, P. Mandeville and L. F. Eastman, "Growth limitations of strained multiple quantum wells," *Journal of Crystal Growth,* vol. 135, no. 1-2, pp. 36-40, 1994.

[51] G. Haarpaintner, J. Barnes, K. W. J. Barnham and J. P. Connolly, "Voltage performance of quantum well solar cells in the AlGaAs/GaAs and the GaAs/lnGaAs material systems," *Photovoltaic Energy Conversion,* vol. 2, no. 1, pp. 1783-1786, 1994.

[52] S. T. Davey, M. A. G. Halliwell, D. C. Rogers, M. Taylor and E. G. Scott, "On the determination of alloy compositions in GaInAs/AlInAs multiple quantum wells," *Journal of Crystal Growth,* vol. 96, no. 2, pp. 258-264, 1989.

[53] H. Kamei, K. Hahizume, M. Murata, N. Kuwata, K. Ono and K. Yoshida, "Growth of AllnAs and heterostructures on InP by OMVPE," *Journal of Crystal Growth,* vol. 93, no. 1-4, pp. 329-335, 1988.

[54] H. Ohtsuka, T. Kitatani, Y. Yazawa and T. Warabisako, "Numerical prediction of InGaAs/GaAs MQW solar cell characteristics under concentrated sunlight," *Solar Energy Materials and Solar Cells,* vol. 50, no. 1-4, pp. 251-257, 1998.

[55] E. Aperathitis, C. G. Scott, D. Sands, V. Foukaraki, Z. Hatzopoulos and P. Panayotatos, "Effect of temperature on GaAs:AlGaAs multiple quantum well solar cells," *Materials Science and Engineering: B,* vol. 51, no. 1-3, pp. 85-89, 1998.

[56] M. Paxman, J. Nelson, B. Braun, J. Connolly, K. W. J. Barnham, C. T. Foxon and J. S. Roberts, "Modeling the spectral response of the quantum well solar cell," *Journal of Applied Physics,* vol. 74, no. 1, p. 614, 1993.

[57] D. B. Bushnell, N. J. Ekins-Daukes, K. W. J. Barnham, J. P. Connolly, J. S. Roberts, G. Hill, R. Airey and M. Mazzer, "Short-circuit current enhancement in Bragg stack multi-quantum-well solar cells for multi-junction space cell applications," *Solar Energy Materials and Solar Cells,* vol. 75, no. 1-2, pp. 299-305, 2003.

[58] D. C. Johnson, I. Ballard, K. W. J. Barnham, D. B. Bishnell, J. P. Connolly and et al, "Advances in Bragg stack quantum well solar cells," *Solar Energy Materials and Solar Cells,* vol. 87, no. 1-4, pp. 169-179, 2005.

[59] W. S. a. H. J. Queisser, "Detailed Balance Limit of Efficiency of p-n Junction Solar Cells," *Journal of Applied Physics,* vol. 32, no. 3, May 1961.

[60] Luque, Antonio and Martí, Antonio, "Increasing the Efficiency of Ideal Solar Cells by Photon Induced Transitions at Intermediate Levels," *Phys. Rev. Lett.,* vol. 78, no. 26, Jun 1997.

[61] A. Luque, P. G. Linares, E. Antolin, I. Ramiro, C. D. Farmer, E. Hernandez, I. Tobias, C. R. Stanley, and A. Marti, "Understanding the operation of quantum dot intermediate band solar cells," *Journal of Applied Physics,* vol. 111, Jan 2012.

[62] S. S. J. A. D. W. S. B. R.P. Raffaelle, "Multi-Junction Solar Cell Spectral Tuning with Quantum Dots," *Photovoltaic Energy Conversion, Conference Record of the 2006 IEEE 4th World Conference on,* vol. 1, pp. 162-166, May 2006.

[63] Sablon, Kimberly A. and Little, John W. and Mitin, Vladimir and Sergeev, Andrei and Vagidov, Nizami and Reinhardt, Kitt, "Strong Enhancement of Solar Cell Efficiency Due to Quantum Dots with Built-In Charge," *Nano Letters,* vol. 11, no. 6, pp. 2311-2317, May 2011.

[64] Wang Zhan-Guo, Chen Yong-Hai, Liu Feng-Qi, Xu Bo, "Self-assembled quantum dots, wires and quantum-dot lasers," *Journal of Crystal Growth,* no. 227-228, pp. 1132-1139, 2001.

[65] Z.R. Wasilewski and S. Fafard and J.P. McCaffrey, "Size and shape engineering of vertically stacked self-assembled quantum dots," *Journal of Crystal Growth,* Vols. 201-202, no. 0, pp. 1131-1135, May 1999.

[66] Martí, Antonio and Cuadra, L. and Luque, Antonio, "Partial filling of a quantum dot intermediate band for solar cells," *IEEE Transactions on Electron Devices,* vol. 48, no. 10, pp. 2394-2399, 2001.

[67] A. Luque, A. Marti, L. Cuadra, "Thermodynamics of solar energy conversion in novel structures," *Physica E: Low-dimensional Systems and Nanostructures,* vol. 14, no. 1-2, pp. 107-114, April 2002.

[68] Luque, Antonio; Marti, Antonio; Cuadra, L., "Impact-ionization-assisted intermediate band solar cell," *IEEE Transactions on Electron Devices,* vol. 50, no. 2, pp. 447-454, Feb 2003.

[69] A.J. Nozik, C.A. Parsons, D.J. Dunlavy, B.M. Keyes, R.K. Ahrenkiel, "Dependence of hot carrier luminescence on barrier thickness in GaAs/AlGaAs superlattices and multiple quantum wells," *Solid State Communications,* vol. 75, no. 4, pp. 297-301, July 1990.

[70] Luque,Antonio and Martí,Antonio and Nozik,Arthur J., "Solar Cells Based on Quantum Dots: Multiple Exciton Generation and Intermediate Bands," *MRS Bulletin,* vol. 32, no. 3, pp. 236-241, Feb 2007.

[71] S. B. Christiana Honsberg, "PV Education," PVEducation Org., [Online]. Available: http://pvcdrom.pveducation.org/CELLOPER/QUANTUM.HTM.

[72] W. Yang, Z. Q. Ma, X. Tang, C. B. Feng, W. G. Zhao and P. P. Shi, "Internal quantum efficiency for solar cells," *Solar Energy,* vol. 82, no. 2, pp. 106-110, 2008.

[73] P. C. Jagdish and M. L. Douglas, "Modeling of multi-junction solar cells for estimation of EQE under influence of charged particles using artificial neural networks," *Renewable Energy,* vol. 44, no. 1, pp. 7-16, 2012.

[74] J. Woo-Seok, L. Jin-Wook, J. Soonil, H. Y. Jae and P. Nam-Gyu, "Evaluation of external quantum efficiency of a 12.35% tandem solar cell comprising dye-sensitized and CIGS solar cells," *Solar Energy Materials and Solar Cells,* vol. 95, no. 12, pp. 3419-3423, 2011.

[75] A. Kongkanand, K. Tvrdy, K. Takechi, M. Kuno and P. V. Kamat, "Quantum Dot Solar Cells. Tuning Photoresponse through Size and Shape Control of CdSe-TiO2 Architecture," *Journal of American Chemical Society,* vol. 1, no. 130, Jan 2008.

[76] T. H. Gfroerer, "Photoluminescence in Analysis of Surfaces and Interfaces," in *Encyclopedia of Analytical Chemistry*, John Wiley & Sons, Ltd, 2006, pp. 9209-9231.

[77] "Basics of X-ray Diffraction," http://www.scintag.com/, ugcc_sr0112, 2013.

[78] Y. Tsuno, Y. Hishikawa and K. Kurokawa, "Modeling of the I– V curves of the PV modules using linear interpolation/extrapolation," *Solar Energy Materials and Solar Cells,* vol. 93, no. 6, pp. 1070-1073, 2008.

[79] R. B. Darling, "http://www.ee.washington.edu," [Online]. Available: http://www.ee.washington.edu/research/microtech/cam/PROCESSES/PDF%20FILES/Photolithography.pdf.

[80] J. Lammasniemi and K. Rakennus, "Effects of annealing on performance of InP solar cells on GaAs substrates," *Solar Energy Materials and Solar Cells,* vol. 30, no. 4, pp. 301-307, 1993.

[81] S. J. Xu, X. C. Wang, S. J. Chua and C. H. Wang, "Effects of rapid thermal annealing on structure and luminescence of self-assembled InAs/GaAs quantum dots," *Applied Physics Letters,* vol. 72, no. 25, pp. 3335-3337, 1998.

[82] "Siliconfareast," [Online]. Available: http://www.siliconfareast.com/lith_electron.htm.

[83] H. Hauser, P. Berger, B. Michl, C. Muller, S. Schwarzkopf, M. Hermle and B. Blasi, "Nanoimprint lithography for solar cell texturisation," *Proceedings SPIE, Micro-Optics,* vol. 7716, no. 1, pp. 77160X 1-77160X 9, 2010.

[84] J.-H. Guo and J. E. Cotter, "Metallization improvement on fabrication of interdigitated backside and double sided buried contact solar cells," *Solar Energy Materials and Solar Cells,* vol. 86, no. 4, pp. 485-498, 2005.

[85] P. Sterian, S. Fara, L. Fara and M. Iancu, "A study of the optical properties of quantum well solar cells aimed at optimizing their configuration," *U. P. B. Scientific Bulletin, Series A,* vol. 27, no. 1, pp. 9-20, 2010.

[86] U. Manmontri, S. Sopitpan, P. Cheewatas, S. Thainoi, S. Rattanathammpan and S. Panyakeow, "Study on GaAs/GaAlAs MQW structure for photovoltaic applications," *Solar Energy Materials and Solar Cells,* vol. 50, no. 1, pp. 265-272, 1998.

[87] K. W. J. Barnham and G. Duggan, "A new approach to high-efficiency multi-band-gap solar cells," *Journal of Applied Physics,* vol. 67, no. 1, pp. 3490-3493, 1990.

[88] D. S. Software, "ATLAS User Manual," [Online]. Available: www.silvaco.com.

[89] M. Concetta Allia, "Device Simulation, IMS CAD & Designs Service," [Online]. Available: www.silvaco.com/content/kbase/.

[90] U. B. M. M. J. Ng, "Defect investigation of stacked self-assembled InAs/GaAs quantum dots lasers," *Physica status solidi,* vol. 4, no. 8, July 2007.

[91] J. N. a. M. Missous, "Improvements of stacked self-assembled InAs/GaAs quantum dot structures for 1.3 μm applications," *Microelectronics Journal,* vol. 37, no. 12, Dic 2006.

[92] S. S. U. T. R. S. R. M. D. R. R. B. K. M. T. Srinivasan, "Structural and photoluminescence characteristics of molecular beam epitaxy-grown vertically aligned In0.33Ga0.67As/GaAs quantum dots," *Journal of Crystal Growth,* vol. 280, no. 3-4, July 2005.

[93] U. B. a. M. M. J T Ng, "Formation and role of defects in stacked large binary InAs/GaAs quentum dot structures," *Semiconductor Science and Technology,* vol. 22, no. 2, Dic 2007.

[94] K. Barnham, J. Connolly, P. Griffin, G. Haarpaintner, J. Nelson, E. Tsui, A. Zachariou, J. Osborne, C. Button, G. Hill, M. Hopkinson, M. Pate, J. Roberts and T. Foxon, "Voltage enhancement in quantum well solar cells," *Journal of Applied Physics,* vol. 80, no. 2, pp. 1201-1206, Jan 1996.

[95] Sablon, K. A. and Little, J. W. and Mitin, V. and Sergeev, A. and Vagidov, N. and Reinhardt, K., "High-efficiency quantum dot solar cells due to inter-dot n-doping," *Proc. SPIE 8111, Next Generation (Nano) Photonic and Cell Technologies for Solar Energy Conversion II,* pp. 81110H-81110H-10, Sept 2011.

[96] C. Schneider, S. Kremling, N. V. Tarakina, T. Braun, M. Adams, M. Lermer, S. Reitzenstein, L. Worschech, M. Kamp, S. Hofling and A. Forchel, "AlGaInAs quantum dot solar cells: tailoring quantum dots for intermediateband formation," *Semiconductors Science Technology,* no. 27, March 2012.

[97] J. C. C. Fan, "Theoretical temperature dependence of solar cell parameters," *Solar Cells,* vol. 17, no. 2-3, pp. 309-315, 1986.

[98] S. P. Phillipps, D. Stetter, R. Hoheisel, M. Hermle, F. Dimroth and A. W. Bett, "Characterization and numerical modeling of the temperature-dependent behavior of GaAs solar cells," *23rd European Photovoltaic Solar Energy Conference,* vol. 23, no. 1, pp. 114-117, 2008.

[99] I. Konovalov, V. Strikha and O. Breitenstein, "Activation energy of local currents in solar cells measured by thermal methods," *Progress in Photovoltaics: Research and Applications,* vol. 6, no. 3, pp. 151-161, 1998.

[100] "Temperature and Irradiance Dependence of the I-V Curves of Various Kinds of Solar Cells," *15th International Photovoltaic Science & Engineering Conference (PVSEC-15),* vol. 26, no. 1, pp. 422-423, 2005.

[101] J. V. Li, S. W. Johnston, Y. Yan and D. H. Levi, "Measuring temperature-dependent activation energy in thermally activated processes: a 2D Arrhenius plot method," *Review of Scientific Instruments,* vol. 81, no. 3, pp. 033910-1 - 033910-5, 2010.

[102] J. Coello, M. Castro, I. Anton, G. Sala and M. A. Vazquez, "Conversion of commercial si solar cells to keep their efficient performance at 15 suns," *Progress in Photovoltaics: Research and Applications,* vol. 12, no. 5, pp. 323-331, 2004.

[103] J. Liang, E. A. Schiff, S. Guha, B. Yan and J. Yang, "Temperature-Dependent Open-Circuit Voltage Measurements and Light-Soaking in Hydrogenated Amorphous Silcon Solar Cells," *Materials Research Society Symposium Proceedings,* vol. 862, no. 1, pp. A21.8.1-A.21.8.6, 2005.

[104] I. Riedel, J. Parisi, V. Dyakonov, L. Lutsen, D. Vanderzande and J. C. Hummelen, "Effect of Temperature and Illumination on the Electrical Characteristics of Polymer–Fullerene Bulk-Heterojunction Solar Cells," *Advanced Functional Materials,* vol. 14, no. 1, pp. 38-44, 2004.

[105] D. E. Carlson, G. Lin and G. Ganguly, "Temperature dependence of amorphous silicon solar cell PV parameters," *Photovoltaic Specialists Conference,* vol. 1, no. 28, pp. 707-713, 2000.

[106] A. Luque, A. Marti and C. Stanley, "Understanding intermediate-band solar cells," *Nature Photonics,* vol. 6, no. 1, pp. 146-152, 2012.

[107] D. Meneses-Rodriguez, P. P. Horley, J. Gonzalez-Hernandez, Y. V. Vorobiev and P. N. Gorley, "Photovoltaic solar cells performance at elevated temperatures," *Solar Energy,* vol. 78, no. 2, pp. 243-250, 2005.

[108] G. Garcia-Belmonte, "Temperature dependence of open-circuit voltage in organic solar cells from generation–recombination kinetic balance," *Solar Energy Materials and Solar Cells,* vol. 94, no. 12, pp. 2166-2169, 2010.

[109] E. A. Katz, D. Faiman, S. M. Tuladhar and J. M. Kroon, "Temperature dependence for the photovoltaic device parameters of polymer-fullerene solar cells under operating conditions," *Journal of Applied Physics,* vol. 90, no. 10, pp. 5343-5350, 2001.

[110] H. Hamadeh, "Temperature dependence of pin solar cell parameters with intrinsic layers made of pm-Si:H and low crystalline volume fraction @mc-Si:H," *Renewable Energy,* vol. 35, no. 7, pp. 1419-1423, 2010.

[111] Z. Macháček, V. Benda and R. Barinka, "Parameters of photovoltaic cells in dependence on irradiance and temperature," *Electroscope,* vol. 3, no. 1, pp. 11-13, 2007.

[112] I. Konovalov, V. Strikha and O. Breitenstein, "Activation Energy of Local Currents in Solar Cells Measured by Thermal Methods," *Progress on Photovoltaic Research Applications,* vol. 6, no. 1, pp. 151-161, 1998.

[113] Y. Tsuno, Y. Hishikawa and K. Kurokawa, "Temperature and Irradiance Dependence of the I-V Curves of Various Kinds of Solar Cells," *15th International Photovoltaic Science & Engineering Conference (PVSEC-15),* vol. 2005, no. 1, 2005.

[114] J. V. Li, S. W. Johnston, Y. Yan and D. H. Levi, "Measuring temperature-dependent activation energy in thermally activated processes: A 2D Arrhenius plot method," *Review of scientific instruments,* vol. 10, no. 1, 2010.

[115] D. Wolpert, "Temperature effects in semiconductors," in *Managing Temperature Effects in Nanoscale Adaptive Systems* , 2012, pp. 15-33.

[116] A. Luque, A. Marti and C. R. Stanley, "Understanding intermediate-band solar cells," *Nature Photonics,* vol. 6, no. 1, pp. 146-152, 2012.

[117] J. Greg, H. F. Lu, L. Fu, H. H. Tan and C. Jagadish, "Electron-hole recombination properties of In0.5Ga0.5As/GaAs quantum dot," *Applied Physics Letters,* vol. 97, no. 12, 2010.

[118] H. F. Lu, L. Fu, G. Jolley, H. H. Tan, S. R. Tatavarti and C. Jagadish, "Temperature dependence of dark current properties of InGaAs/GaAs quantum dot solar cells," *Applied Physics Letters,* vol. 98, no. 18, 2011.

[119] J. F. Geisz, D. J. Friedman, J. M. Olson, S. R. Kurtz and B. M. Keyes, "Photocurrent of 1 eV GaInNAs lattice-matched to GaAs," *Journal of Crystal Growth,* vol. 195, no. 1-4, pp. 401-408, 1998.

[120] E. Garduño-Nolasco, M. Missous, D. Donoval, J. Kovac and M. Mikolasek, "Temperature dependence of InAs/GaAs Quantum Dots solar photovoltaic devices," *Journal of Semiconductors,* 2014.

[121] Y. Varshni, "Temperature dependence of the energy gap in semiconductors," *Physica,* vol. 34, no. 1, pp. 149-154, 1967.

[122] M. A. Green, A. W. Blakers, J. Shi, E. M. Keller and S. R. Wenham, "19.1% efficient silicon solar cell," *Applied Physics Letters,* vol. 44, no. 12, pp. 1163-1164, 1984.

[123] D. Bouhafs, A. Moussi, A. Chikouche and J. M. Ruiz, "Design and simulation of antireflection coating systems for optoelectronic devices: Application to silicon solar cells," *Solar Energy Materials and Solar Cells,* vol. 52, no. 1-2, pp. 79-93, 1998.

[124] D. Bouhafs, A. Moussi, A. Chikouche and J. M. Ruiz, "Design and simulation of antireflection coating systems for optoelectronic devices: Application to silicon solar cells," *Solar Energy Materials and Solar Cells,* vol. 52, no. 1, pp. 79-93, 1998.

[125] A. Bahrami, S. Mohammadnejad, N. Jouyandeh and S. Soleimaninezhad, "Optimized Single and Double Layer Antireflection Coatings for GaAs Solar Cells," *International Journal of Renewable Energy Research-IJRER,* vol. 3, no. 1, pp. 79-83, 2013.

[126] M. H. Abdullah and M. Rusop, "Novel ITO/arc-TiO2 antireflective conductive substrate for transmittance enhanced properties in dye-sensitized solar cells," *Microelectronic Engineering,* vol. 108, no. 1, pp. 99-105, 2013.

[127] B. Kepenek, S. Oncel, A. F. Cakir and M. Urgen, "Photoactive TiO2 Coatings on Metal Substrates by Cathodic Arc Deposition Technique," *Key Engineering Materials,* Vols. 264-268, no. 1, pp. 549-552, 2004.

[128] "Anti-Reflective Coatings," [Online]. Available: http://pveducation.org/pvcdrom/design/anti-reflection-coatings.

[129] "Refractive Index of GaAs, Gallium Arsenide," Filmetrics, [Online]. Available: http://www.filmetrics.com/refractive-index-database/GaAs/Gallium-Arsenide.

[130] "Optical constants of Si3N4 (Silicon nitride)," Refractive Index.inf, [Online]. Available: http://refractiveindex.info/?group=CRYSTALS&material=Si3N4.

[131] H. J. Lee, C. H. Henry, K. J. Orlowsky, R. F. Kazarinov and T. Y. Kometani, "Refractive-index dispersion of phosphosilicate glass, thermal oxide, and silicon nitride films on silicon," *Applied Optics,* vol. 27, no. 19, pp. 4104-4109, 1988.

[132] F. Reizman and W. V. Gelder, "Optical thickness measurement of SiO2 and Si3N4 films on silicon," *Solid-State Electronics,* vol. 10, no. 7, pp. 625-632, 1967.

[133] "Si3N4 Color Chart for LPCVD grown silicon nitride," MEMS Foundry, [Online]. Available: http://www.mems-foundry.com/appnotes/si3n4_color_chart_LPCVD_silicon_nitride.htm.

[134] N. J. Ekins-Daukes, K. W. J. Barnham, J. P. Connolly and J. S. Roberts, “Strain-balanced GaAsP/InGaAs quantum well solar cells,” *Applied Physics Letters,* vol. 75, no. 26, pp. 4195-4197, 1999.

[135] F. Sohrabi, A. Nikniazi and H. Movla, “Optimization of Third Generation Nanostructured Silicon-Based Solar Cells,” in *Solar Cells - Research and Application Perspectives",,* INTECH, 2013.

[136] D. N. Wrigth, E. S. Marstein and A. Holt, “Double layer anti-reflective coatings for silicon solar cells,” *Photovoltaic Specialists Conference,* vol. 1, no. 31, pp. 1237-1240, 2005.

[137] L. B. Karlina, V. V. Vozlovskii, V. A. Solov'ev and M. Z. Shvarts, “The effects of irradiation on heteroepitaxial InP/InGaAs solar cells,” *Photovoltaic Specialists Conference,* vol. 1, no. 25, pp. 239-242, 1996.

[138] A. Zachariou, K. W. J. Barnham, P. Griffin and J. Nelson, “A new approach to p-doping and the observation of efficiency enhancement in InP/InGaAs quantum well solar cells,” *Photovoltaic Specialists Conference,* vol. 1, no. 25, pp. 113-116, 1996.

[139] K. Aydin, M. S. Leite and H. A. Atwater, “Increased cell efficiency in InGaAs thin film solar cells with dielectric and metal back reflectors,” *Photovoltaic Specialists Conference (PVSC),* vol. 1, no. 34, pp. 1713-1717, 2009.

[140] H. Kamei, K. Hashizume, M. Murata, N. Kuwata, K. Ono and K. Yoshida, “Growth of AlInAs and heterostructures on InP by OMVPE,” *Journal of Crystal Growth,* vol. 93, no. 1-4, pp. 329-335, 1988.

[141] D. Saeedkia and S. Safavi-Naeini, “"Terahertz photonics: Optoelectronic techniques for generation and detection of terahertz waves",” *J. Lightw. Technol.,* vol. 26, no. 15, pp. 2409-2423, 2008.

[142] S. Y. Chiang and G. L. Pearson, “"Properties of vacancy defects in GaAs single crystals",” *J. Appl. Phys.,* vol. 46, no. 7, pp. 2986-2991, 1975.

[143] P. Kordos, F. Ruders, M. Marso and A. Forster, “"Properties of LT GaAs for photomixing up to THz frequencies",” in *Optoelectronic and Microelectronic Materials and Devices Proceedings,* Research Centre Julich, Germany, 1996.

[144] I. Gregory, C. Baker, W. R. Tribe, M. Evans, H. Beere, E. Linfield, A. Davies and M. Missous, “"High resistivity annealed low-temperature GaAs with 100 fs lifetimes",” *Appl. Phys. Lett.,* vol. 83, pp. 4199-4201, 2003.

[145] P. Upadhya, W. Fan, A. Burnett, J. Cunningham, A. Davies, E. Linfield, J. Hughes, E. Camus, M. Johnston and H. Beere, “"Excitation-density-dependent generation of broadband terahertz radiation in an assymetrically excited photoconductive antenna",” *Opt. Lett.,* vol. 32, no. 16, p. 2297, 2007.

[146] L. Duvillaret, F. Garet, J. Roux and J. Coutaz, “"Analytical modelling and optimization of terahertz time-domain spectroscopy experiments using photoswitches as antennas",” *IEEE J. Sel. Top. Quantum Electron.,* vol. 7, no. 4, p. 615, 2001.

[147] D. Saeedkia and S. Safavi-Naeini, “"A comprehensive model for photomixing in ultrafast photoconductors",” *IEEE Photon. Technol. Lett. ,* vol. 18, no. 13, pp. 1457-1459, 2006.

[148] D. Saeedkia, “"Terahertz photoconductive antennas: Principles and applications",” in *5th Eur. Conf. Antennas Propag.,* Rome, 2011.

[149] E. R. Brown, “"THz generation by photomixing in ultrafast photoconductors",” *Terahertz Sensing Technol.,* vol. 1, pp. 147-195, 2003.

[150] Y. Chen, S. Prabhu, S. Ralph and D. McInturff, “"Trapping and recombination dynamics of low temperature-grown InGaAs/InAlAs multiple quantum wells",” *Appl. Phys. Lett.,* vol. 72, no. 4, p. 439, 1998.

[151] S. Preu, G. H. Dohler, S. Malzer, L. J. Wang and A. C. Gossard, “"Tunable, continuous-wave terahertz photomixer sources and applications",” *J. Appl. Phys.,* vol. 109, p. 061301, 2011.

[152] B. Sartorius, H. Roehle, H. Kunzel, J. Bottcher, M. Schlak, D. Stanze, H. Venghaus and M. Schell, “"All fiber terahertz time domain spectrometer operating at 1.5 μm telecom wavelengths",” *Opt. Express,* vol. 16, no. 13, p. 9565, 2008.

[153] K. Biermann, D. Nickel, K. Reimann, M. Woerner, S. Elsaesser and H. Kuenzel, “"Ultrafast optical nonlinearity of low-temperature grown GaInAs/AlInAs quantum wells at wavelength around 1.55 μm",” *Appl. Phys. Lett.,* vol. 80, no. 11, pp. 1936-1938, 2002.

[154] R. Takahashi, Y. Kawamura and H. Iwamura, “"Ultrafast 1.55 μm all optical switching using low-temperature-grown multiple quantum wells",” *Appl. Phys. Lett.,* vol. 68, no. 8, pp. 153-155, 1996.

[155] C. Baker, I. Grecory, W. Tribe, I. Bradley, M. Evans, M. Withers, P. Taday, V. Wallace, E. Linfield, A. Davies and M. Missous, “"Terahertz pulsed imaging with 1.06 μm laser excitation",” vol. 83, no. 20, pp. 4113-4115, 2003.

[156] C. Baker, I. Grecory, W. Tribe, I. Bradley, M. Evans, E. Linfield and M. Missous, “"Highly resistive annealed low-temperature-grown InGaAs with sub-fs 500 carrier lifetimes",” *Appl. Phys. Lett.,* vol. 85, no. 21, pp. 4965-4967, 2004.

[157] G. M. Martin, J. P. Farges, G. Jacob, J. P. Hallais and G. Poiblaud, “"Compensation mechanisms in GaAs",” *J. Appl. Phys.,* vol. 51, no. 5, pp. 2840-2852, 1980.

[158] G. M. Martin, “"Optical assessment of the main electron trap in bulk semi-insulating GaAs",” *Appl. Phys. Lett.,* vol. 39, no. 9, pp. 747-748, 1981.

[159] G. Williams, “"Filling the THz gap - High power sources and applications",” *Rep. Prog. Phys. ,* vol. 69, pp. 301-326, 2006.

[160] A. G. Davies, E. H. Linfield and M. B. Johnston, “"The development of terahertz sources and their applications",” *Phys. Med. Biol.,* vol. 47, pp. 3679-3689, 2002.

[161] E. R. Mueller, “"Terahertz radiation: Application and sources",” *Industrial Physicist Online,* vol. 9, pp. 29-31, 2003.

[162] J. E. Bjarnason, T. L. Chan, A. W. Lee, M. A. Celis and E. R. Brown, “"Millimeter-wave, Terahertz and mid-infrared transmission through common clothing",” *Appl. Phys. Lett.,* vol. 85, pp. 519-521, 2004.

[163] Y.-S. Jin, G.-J. Kim and S.-G. Jeon, “"Terahertz Dielectric properties of Polymers",” *J. Korean Phys. Soc. ,* vol. 49, pp. 513-517, 2006.

[164] K. Kawase, Y. Ogawa, H. Minamide and H. Ito, “"Terahertz parametric sources and imaging applications",” *Semicond. Sci. Technol. ,* vol. 20, pp. 258-265, 2005.

[165] P. H. Siegel, “"Terahertz Technology",” *IEEE Transactions on Microwave Theory and Techniques,* vol. 50, no. 3, pp. 910-928, 2002.

[166] N. Karpowicz, H. Zhong, C. Zhang, K.-I. Lin, J.-S. Hwang, J. Xu and X.-C Zhang, “"Compact continuous-wave subterahertz system for inspection applications",” *Appl. Phys. Lett,* vol. 86, no. 5, p. 054105, 2005.

[167] T. Fong and H. Kuno, “"Millimeter-wave pulsed IMPATT sources",” *IEEE Trans. Microw. Theory Techn. ,* vol. 27, pp. 492-499, 1979.

[168] H. Eisele, A. Rydberg and G. I. Haddad, “"Recent advances in the performance of InP Gunn devices and GaAs TUNNETT diodes for the 100-300 GHz frequency range and above",” *IEEE Trans. Microw. Theory Techn.*, vol. 48, no. 4, pp. 626-631, 2000.

[169] E. R. Brown, J. R. Soderstrom, C. D. Parker, L. J. Mahoney, K. M. Molvar and T. C. McGill, “"Oscillations up to 712 GHz in InAs/AlSb resonant-tunneling diodes",” *Appl. Phys. Lett.*, vol. 58, no. 20, pp. 2291-2293, 1991.

[170] J. Liu, J. Dai, X. Lu, I-C. Ho and X.-C. Zhang, “"Broadband Terahertz Wave Generation, Detection and Coherent Control Using Terahertz Gas Photonics",” *Int. J. Hi. Spe. Ele. Syst.*, vol. 20, no. 1, pp. 3-12, 2011.

[171] J. Faist, F. Capasso, D. L. Sivco, C. Sirtori, A. L. Hutchinson and A. Y. Cho, “"Quantum Cascade Laser",” *Science*, vol. 264, pp. 553-556, 1994.

[172] M. Abo-Bakr, J. Feikes, K. Holldack, G. Wustefeld and H.-W. Hubers , “"Steady-state far infrared coherent synchrotron radiation detected at BESSY II",” *Phys. Rev. Lett.*, vol. 88, p. 254801, 2002.

[173] A. Bergner, U. Heugen, E. Brundermann, G. Schwaab, M. Havenith, D. R. Chamberlin and E. E. Haller, “"New p-Ge THz laser spectrometer for the study of solutions: THz absorption spectroscopy of water",” *Review of Scientific Instruments*, vol. 76, no. 6, p. 063110, 2005.

[174] G. Ramian, “"The new UCSB free-electron lasers",” *Nuclear Instruments & Methods in Physics Research*, vol. 318, no. 1-3, pp. 225-229, 1992.

[175] G. K. a. P. Palluel, “"Backward Wave Oscillators",” in *"Infrared and Millimeter Waves"*, vol. 1, Academic Press, 1979.

[176] D. Auston, “"Picosecond optoelectronic switching and gating in silicon",” *Appl. Phys. Lett.*, vol. 26, no. 3, pp. 101-103, 1975.

[177] C. Lee, “"Picosecond optoelectronic switching in GaAs",” *Appl. Phys. Lett.*, vol. 30, no. 2, pp. 84-86, 1977.

[178] G. P. Gallerano and S. Biedron, “"Overview of terahertz radiation sources",” in *Proceedings of the 2004 FEL Conference*, Trieste, Italy, 2004.

[179] R. Kohler, A. Tredicucci, F. Beltram, H. E. Beere, E. H. Linfield, A. G. Davies, D. A. Ritchie, R. C. Lotti and F. Rossi , “"Terahertz semiconductor-heterostructure laser",” *Nature*, vol. 417, pp. 156-159, 2002.

[180] A. W. M. Lee, Q. Qin, S. Kumar, B. S. Williams, Q. Hu and J. L. Reno , “"High-power and high-temperature THz quantum-cascade lasers based on lenscoupled metal-metal waveguides",” *Opt. Lett.*, vol. 32, no. 19, pp. 2840-2842, 2007.

[181] S. Cherednichenko, P. Khosropanah, E. Kollberg, M. Kroug and H. Merkel, “"Terahertz superconducting hot-electron bolometer mixers",” *Physica C Superconductivity*, vol. 372, pp. 407-415, 2002.

[182] D. E. Prober, “"Superconducting terahertz mixer using a transitionedge microbolometer",” *Appl. Phys. Lett.*, vol. 62, no. 17, pp. 2119-2121, 1993.

[183] E. R. Brown, K. A. McIntosh, K. B. Nichols and C. L. Dennis, “"Photomixing up to 3.8 THz in low temperature-grown GaAs",” *Appl. Phys. Lett.*, vol. 66, no. 3, pp. 285-287, 1995.

[184] I. Brener, D. Dykaar, A. Frommer, I. N. Pfeiffer, J. Lopata, J. Wynn, K. West and M. C. Nuss, “"Terahertz emission from electric field singularities in biased semiconductors",” *Optics Letters*, vol. 21, no. 23, pp. 1924-1926, 1996.

[185] G. Zhao, R. N. Schouten, N. van der Valk, W. Th. Wenckebach and P. C. M. Planken, “"Design and performance of a THz emission and detection setup based on a semi-insulating GaAs emitter",” *Rev. Sci. Instrum.*, vol. 73, no. 4, pp. 1715-1719, 2002.

[186] Z. Jiang and X.-C. Zhang, “"Terahertz imaging via electrooptic effect",” *IEEE Trans. Microw. Theory Tech.,* vol. 47, no. 12, pp. 2644-2650, 1999.

[187] Q. Wu, T. D. Hewitt and X.-C. Zhang, “"Two dimensional eletro-optic imaging of THz beams",” *Appl. Phys. Lett.,* vol. 69, no. 8, pp. 1026-1028, 1996.

[188] D. Auston and K. Cheung, “"Coherent time-domain far-infrared spectroscopy",” *J. Opt. Soc. Am. B,* vol. 2, pp. 606-612, 1985.

[189] B. Ferguson and X. Zhang, “"Materials for terahertz science and technology",” *Nat. Mater.,* vol. 1, no. 1, pp. 26-33, 2002.

[190] W. S. Holland, J. S. Greaves, B. Zuckerman, R. A. Webb, C. McCarthy, I. M. Coulson, D. M. Walther, W. R. F. Dent, W. K. Gear and I. Robson, “"Submillimeter images of dusty debris around nearby stars",” *Nature,* vol. 392, pp. 788-791, 1998.

[191] K. Kawase, Y. Ogawa, Y. Watanabe and H. Inoue, “"Non-destructive terahertz imaging of illicit drugs using spectral fingerprints",” *Optics Express,* vol. 11, no. 20, pp. 2549-2554, 2003.

[192] Y. Shen, T. Lo, P. Taday, B. Cole, W. Tribe and M. Kemp, “"Detection and identification of explosives using terahertz pulsed spectroscopic imaging",” *Appl. Phys. Lett.,* vol. 86, p. 241116, 2005.

[193] T. Yasui, T. Yasuda, K. Sawanaka and T. Araki, “"Terahertz paintmeter for noncontact monitoring of thickness and drying progress in paint film",” *Appl. Opt.,* vol. 44, no. 32, pp. 6849-6856, 2005.

[194] R. Woodward, B. Cole, V. Wallace, R. Pye, D. Arnone, E. Linfield and M. Pepper, “"Terahertz pulse imaging in reflection geometry of human skin cancer and skin tissue",” *Physics in Medicine and Biology,* vol. 47, no. 21, pp. 3853-3863, 2002.

[195] Y. C. Shen, P. C. Upadhya, H. E. Beere, E. H. Linfield, A. G. Davies, I. S. Gregory, C. Baker, W. R. Tribe and M. J. Evans , “"Generation and detection of ultrabroadband terahertz radiation using photoconductive emitters and receivers",” *Appl. Phys. Lett.,* vol. 85, no. 2, pp. 164-166, 2004.

[196] Y. C. Shen, P. C. Upadhya, E. H. Linfield, E. H. Beere and A. G. Davies, “"Ultrabroadband terahertz radiation from low-temperature-grown GaAs photoconductive emitters",” *Appl. Phys. Lett.,* vol. 83, no. 15, pp. 3117-3119, 2003.

[197] W. L. Chan, J. Deibel and D. M. Mittleman, “"Imaging with terahertz radiation",” *Rep. Prog. Phys. ,* vol. 70, pp. 1325-1379, 2007.

[198] B. Hu and M. Nuss, “"Imaging with terahertz waves",” *Op. Lett.,* vol. 20, no. 16, pp. 1716-1718, 1995.

[199] D. Mittleman, S. Hunsche, L. Boivin and M. Nuss, “"T-ray tomography",” *Opt. Lett.,* vol. 22, no. 12, pp. 904-906, 1997.

[200] S. Kono, M. Tani and K. Sakai, “"Generation and Detection of Broadband Pulsed Terahertz Radiation",” in *Terahertz Optoelectronics,* vol. 97, Topics Appl. Phys, 2005, p. 31.

[201] M. Tani, S. Matsuura, K. Sakai and S. Nakashima, “"Emission characteristics of photoconductive antennas based on low-temeprature-grown GaAs and semi-insulating GaAs",” *Appl. Opt.,* vol. 36, no. 30, pp. 7853-7859, 1997.

[202] S. Verghese, K. A. McIntosh and E. R. Brown, “"Highly Tunable Fiber-Coupled Photomixers with Coherent Terahertz Output Power",” *IEEE Trans. Microw. Theory Techn.,* vol. 45, no. 8, pp. 1301-1309, 1997.

[203] E. R. Brown, “"A photoconductive model for superior GaAs THz photomixers",” *Appl. Phys. Lett.,* vol. 75, no. 6, pp. 769-771, 1999.

[204] B. Sartorius, D. Stanze, T. Gobel, D. Schmidt and M. Schell, “"Continuous Wave Terahertz Systems Based on 1.55 μm Telecom Technologies",” *J. Infrared Milli. Terahz. Waves,* vol. 33, no. 4, pp. 405-417, 2012.

[205] C. Baker, I. S. Gregory, M. J. Evans, W. R. Tribe, E. H. Linfield and M. Missous, “" All-optoelectronic terahertz system using low-temperature-grown InGaAs photomixers",” *Optics Express,* vol. 13, no. 23, pp. 9639-9644, 2005.

[206] K. Sakai, in *Terahertz optoelectronics*, vol. 97, 2005, pp. 157-202.

[207] S. Matsuura, M. Tani and K. Sakai, “"Generation of coherent terahertz radiation by photomixing in dipole photoconductive antennas",” *Appl. Phys. Lett.,* vol. 70, no. 5, pp. 559-561, 1996.

[208] S. Verghese, K. A. McIntosh, S. Calawa, W. F. Dinatale, E. K. Duerr and K. A. Molvar, “"Generation and detection of coherent terahertz waves using two photomixers",” *Appl. Phys. Lett.,* vol. 73, no. 26, pp. 3824-3826, 1998.

[209] B. Sartorius, M. Schlak, D. Stanze, H. Roehle, H. Kunzel, D. Schmidt, H.-G. Bach, R. Kunkel and M. Schell, “"Continuous wave terahertz systems exploiting 1.5 μm telecom technologies",” *Optics Express,* vol. 17, no. 17, pp. 15001-15007, 2009.

[210] M. Luysberg, H. Sohn, A. Prasad, P. Specht, Z. Liliental-Weber, E. R. Weber, J. Gebauer and R. Krause-Rehberg, “"Effects of the growth temperature and As/Ga flux ratio on the incorporation of excess As into low temperature grown GaAs",” *J. Appl. Phys.,* vol. 83, no. 1, pp. 561-566, 1998.

[211] B. G. Yacobi, "Semiconductor Materials: An Introduction to Basic Principles", New York: Kluwer Academic Publishers, 2003.

[212] G. M. Martin, “"Optical assessment of the main electron trap in bulk semi-insulating GaAs",” *Appl. Phys. Lett.,* vol. 39, no. 9, pp. 747-748, 1981.

[213] M. R. Melloch, N. Otsuka, J. M. Woodall, A. C. Warren and J. L. Freeouf, “"Formation of arsenic preicpitates in GaAs buffer layers grown by molecular beam epitaxy at low substrate temepratures",” *Appl. Phys. Lett.,* vol. 57, no. 15, pp. 1531-1533, 1990.

[214] W. C. Lee, T. M. Hsu, J. -I. Chyi, G. S. Lee, W. -H. Li and K. C. Lee, “"Characterisation of low temperature GaAs grown by molecular beam epitaxy",” *Appl. Surface Sci.,* vol. 92, pp. 66-69, 1996.

[215] D. H. Youn, S. -J. Kim, G. -Ho Kim and K. -Y. Kang, “"Structural Change and Its Electrooptical Effects on Terahertz Radiation with Post-Growth Annealing of Low-Temeprature-Grown GaAs",” *Jap. J. Appl. Phys.,* vol. 46, no. 10A, pp. 6514-6518, 2007.

[216] D. H. Youn, S. -H. Lee, H. -C. Ryu, Se-Y. Jung, S.-B. Kang, M.-H. Kwack, S. Kim, S.-K. Choi, M.-C Baek, K.-Y. Kang, C.-S. Kim, K.-J. Yee, Y.-B. Ji, E.-S. Lee, T.-I. Jeon, S.-J. Kim, S. Kumar and G.-H. Kim, “"Effects of post-growth annealing on the structure and electro-optical properties of low-temperature grown GaAs",” *J. Appl. Phys.,* vol. 103, p. 123528, 2008.

[217] N. Hozhabri, S. -H. Lee and K. Alavi, “"Infrared measurements in annealed molecular beam epitaxy GaAs grown at low temperature",” *Appl. Phys. Lett.,* vol. 66, no. 19, pp. 2546-2548, 1995.

[218] M. O. Manasreh, D. C. Look, K. R. Evans and C. E. Stutz, “"Infrared absorption of deep defects in molecular-beam-epitaxial GaAs layers grown at 200 C: Observation of an EL2-like defect",” *Phys. Rev. B,* vol. 41, no. 14, pp. 10272-10275, 1990.

[219] Q. Fu, Radiation Solar, Georgia Tech, 2009.

[220] J. L. a. G. W. Adolf Goetzberger, “Solar cells: past, present, future,” *Solar Energy Materials & Solar Cells,* vol. 74, Nov 2002.

[221] N. A. Sobolev, “Radiation Effects in Quantum Dot Structures,” in *Handbook of Self Assembled semiconductor Nanostructures for Novel Devices in Photonics and Electronics*, Elsevier, 2008, pp. 392-447.

[222] Sugiura, H. and Amano, C. and Yamamoto, A. and Yamaguchi, M., “Double heterostructure GaAs tunnel junction for a AlGaAs/GaAs tandem solar cell,” *Japanese Journal of Applied Physics*, vol. 27, pp. 296-272, Feb 1988.

[223] Q. Shao, A. A. Balandin, A. I. Fedoseyev and M. Turowski, “Intermediate-band solar cells based on quantum dot supracrystals,” *Applied Physics Letters*, vol. 91, no. 16, pp. 163503-1 - 163503-3, 2007.

[224] A. J. Nozik, “Quantum dot solar cells,” *Physica E: Low-dimensional Systems and Nanostructures*, vol. 14, no. 1-2, pp. 115-120, 2002.

[225 A. J. Nozik, “Multiple exciton generation in semiconductor quantum dots,” *Chemical Physics Letters*, vol. 457, no. 1-3, pp. 3-11, 2008.